A Thermally Efficient Micro-Reactor for Thermophotovoltaic Power Generation

by

Ole Mattis Nielsen

Submitted to the Department of Electrical Engineering and Computer Science
in partial fulfillment of the requirements for the degree of

Doctor of Philosophy in Electrical Engineering

at the

MASSACHUSETTS INSTITUTE OF TECHNOLOGY

September 2006

MASSACHUSETTS INSTITUTE OF TECHNOLOGY
JAN 11 2007
LIBRARIES

© Massachusetts Institute of Technology 2006. All rights reserved.

Author .....
Department of Electrical Engineering and Computer Science
August 21, 2006

Certified by 8/24/06
Martin A. Schmidt
Professor of Electrical Engineering
Thesis Supervisor

Certified by .....
Klavs F. Jensen
Lammot du Pont Professor of Chemical Engineering
Thesis Supervisor

Accepted by .....
Arthur C. Smith
Chairman, Department Committee on Graduate Students

ARCHIVES

A Thermally Efficient Micro-Reactor for Thermophotovoltaic Power Generation

by

Ole Mattis Nielsen

Submitted to the Department of Electrical Engineering and
Computer Science
on August 21, 2006, in partial fulfillment of the
requirements for the degree of
Doctor of Philosophy in Electrical Engineering

Abstract

Hydrocarbon fuels exhibit very high energy densities, and micro-generators converting the stored chemical energy into electrical power are interesting alternatives to batteries in certain applications. The increasing demands in power and total energy delivered to portable consumer electronics such as laptops, and to military equipment that most soldiers carry with them today, open up opportunities for the miniaturization of different energy conversion technologies.

A thermally efficient MEMS (micro electro mechanical systems) suspended micro-reactor (SμRE) for thermophotovoltaic (TPV) power generation has been designed and fabricated. In TPV systems, photocells convert radiation from a combustion-heated emitter, into electrical power. TPV is an indirect conversion scheme that goes through the thermal domain and therefore does not exhibit very high efficiencies. However, because of its simple structure and because the combustor and photocell fabrication processes do not need to be integrated, the system is simpler to micro-fabricate than other generator types, such as thermoelectric systems and fuel cells. It is also a mechanically passive device that is virtually noiseless and less subject to wear than engines and turbines. The SμRE serves as a catalytic combustor-emitter, heated by combustion of propane in air, and the radiation emitted is converted into electrical energy by low-bandgap, gallium-antimonide (GaSb) photocells.

The SμRE combines thermal isolation provided by long, thin-walled silicon nitride tubes, with the high thermal conductivity of a silicon reaction chamber and heat exchangers to obtain a thermally efficient device. The latest generation of reactors, SμRE III, has been designed, fabricated and thermally characterized, using a three-wafer bonding process to achieve circular tubes. The packaged device measures 11.5x15.5x3 mm, with a reaction chamber of dimensions 5x5x2 mm. Net TPV power generation of up to 1 mW during autothermal propane combustion has been achieved in an earlier and smaller version of the reactor, SμRE I, constituting a promising proof of concept and the first reported net power generation in a MEMS based TPV system.

Thesis Supervisor: Martin A. Schmidt
Title: Professor of Electrical Engineering

Thesis Supervisor: Klavs F. Jensen
Title: Lammot du Pont Professor of Chemical Engineering

Acknowledgments

There are many people I need to thank for helping me get successfully to the end of this thesis. First, I must thank my thesis supervisors, Professors Martin Schmidt and Klavs Jensen, for always being supportive and professional and for contributing invaluable expertise. I would also like to thank Professor Clifton Fonstad for serving on my thesis committee, providing expertise in the area of photocells and TPV.

Leonel Arana's impressive work on the first generation of the micro-reactors laid much of the foundation that my work built on. During the time that we overlapped at MIT, he was always very helpful and wonderful to work with, and I cannot stress enough how important he was in getting my work off to a good start. I must also thank Aleksander Franz and Samuel Schaevitz, who were instrumental in the original device development, for their support. Chelsey Baertsch very generously provided her expertise in catalysts. Kishori Deshpande and Smitha Matthews both helped me out in the fab at different times, and I am especially grateful to Kishori for providing a substantial amount of help over the past year.

I want to thank Alexander Mitsos and Michael Hencke for providing important simulations of mass and heat flow in my devices. Alexander also helped me in grasping many important concepts within the realm of gas flow and thermal management. I must also thank Ivan Celanovic for being very generous with his time and knowledge of TPV systems. David Jenicek, working for Ivan, spent many weeks characterizing my photocells, and I am very grateful for this important contribution during a very busy time. A special thanks goes to Namiko Yamamoto for being very generous with her time.

My gratitude goes to the past and present members of the Schmidt Group for both social and professional contributions to my life as a graduate student. I have made many friends, and I want mention in particular Xue'en Yang, Christine Tsau, Valerie Leblanc, Kerry Cheung, Vikas Sharma, Jeremy Chou and Ankur Mehta. Without them my work days would have been much duller. I also want to thank the many members (not already mentioned) of the Jensen Group that I interacted with during

my years here.

Working in the fab can be both very challenging and at times dull. I could not have done it without the help of the MTL staff that was always very supportive and a good source of solutions to the various problems I ran into. In particular I want to thank Dennis Ward, Dave Terry, Bob Bicchieri, Donal Jamieson, Gwen Donahue, Pat Burkhart and Vicky Diadiuk for all their contributions in so many ways. Likewise, many of the students in MTL have helped make my time in the fab enjoyable; Niamh, Joyce, Andy and many more.

I would also like to thank David Barlow and Kate McHugh for their extremely important help this past Spring.

I cannot stress how important my family and their support has been to me, especially over the past year. They are always a solid foundation I can lean on. And my life would not be nearly as joyful without my soon to be wife Josie. She brightens my day, and helps me get through the tough times. I do not have space to mention all of my friends here, but especially the friendship of Daniele and Radhika and Jang has been very important.

Lastly I want to thank and remember two dear friends who passed away during my thesis work. Jaemin Rhee, my friend and accompanist, chose to leave us in the Spring of 2003. Antimony Gerhardt, friend and collegue in the Schmidt Group, died tragically last Fall. Nothing can replace them, but I will always carry their memory with me. I dedicate this thesis to them.

Contents

1 Introduction **17**

1.1 Motivation 17

1.2 Electrical power generators 19

1.2.1 Generators and batteries 19

1.2.2 Important metrics and definitions 20

1.3 Thermophotovoltaic technology 23

1.3.1 TPV overview 23

1.3.2 Thermophotovoltaic system components 24

1.4 Background 28

2 SμRE design **31**

2.1 Generator thermal management 31

2.2 Scaling 33

2.2.1 Optics 33

2.2.2 Heat transfer 34

2.2.3 Fluid mechanics 36

2.2.4 Conclusion on scaling 38

2.3 SμRE III design 38

2.3.1 MEMS technology 38

2.3.2 SμRE III: Important design features 39

2.3.3 From design to fabrication process 47

2.3.4 SμRE III evolved from SμRE I 49

2.4 Applications of SμRE III 52

3 SμRE III fabrication **55**

3.1 Fabrication process 55

3.1.1 Center wafer: tube mold 56

3.1.2 Capping wafer #1 56

3.1.3 Capping wafer #2 59

3.1.4 Bonding and preparation for release 60

3.1.5 Final release 65

3.2 Critical fabrication steps 66

3.2.1 DRIE through etch 66

3.2.2 Wafer bonding 69

3.2.3 LPCVD silicon nitride growth 70

3.2.4 Metal deposition 70

3.2.5 Final release etch 71

3.2.6 DRIE halo etch 72

3.2.7 Dry photoresist 72

3.3 Fabricated devices 74

3.4 Fabrication evolution from previous SμRE generations 77

4 Modeling **81**

4.1 Modeled structure 82

4.2 Thermal pathways of SμRE III 84

4.2.1 Platinum/nitride bridges: solid conduction 84

4.2.2 Nitride tubes: solid conduction and forced convection 85

4.2.3 Radiation 87

4.2.4 Ambient: gas conduction and natural convection 89

4.3 SμRE III thermal model results 89

4.4 Photocells 93

4.4.1 Photocell characterization 93

4.4.2 Partial illumination 94

5 Experiments **97**

5.1 Overview of experiments 97

5.2 Device preparation 99

5.2.1 Packaging 100

5.2.2 Catalyst loading 100

5.2.3 Aluminum fixtures 105

5.3 Test setup 105

5.3.1 Hardware 105

5.3.2 Software 109

6 Experimental results **111**

6.1 SμRE I experimental results 111

6.1.1 Test setup 111

6.1.2 TPV power output with electrical heating 113

6.1.3 Combustion testing and net TPV power generation 113

6.1.4 Discussion 116

6.2 SμRE III experimental results 117

6.2.1 Mechanical strength 117

6.2.2 Thermal characterization 117

6.2.3 Further testing 120

6.2.4 Discussion 121

7 Conclusion **123**

7.1 Principal achievements 123

7.2 Limitations of SμRE III 124

7.3 Recommendations for future work 124

A SμRE III fabrication process flow **127**

A.1 Process flow 127

A.2 Legend 131

A.2.1 Laboratories 131

A.2.2 Machines 131
A.2.3 Acronyms 132

B Photomasks **133**

C Thermal modeling program code **139**
C.1 therm.m 139
C.2 matrixes.m 141
C.3 viewfactors.m 143
C.4 radiation.m 145

List of Figures

1-1 Conceptual graph of electrical energy vs. system weight for generators and batteries. 20

1-2 Conceptual diagram of TPV thermal management. 25

1-3 SμRE I. 28

2-1 General TPV combustor-emitter thermal requirements. 32

2-2 Conceptual representation of laminar flow velocity profile. 37

2-3 SμRE III model. 40

2-4 SμRE III silicon nitride tube section with heat exchangers. 41

2-5 SμRE III heat exchangers with nitride covered channels. 43

2-6 SμRE III reaction chamber. 44

2-7 Plot of resistance change with temperature, with quadratic fit, in a platinum thin-film resistor [1]. 46

2-8 4-point probe circuit diagram. 47

2-9 SμRE III protected with packaging chips. 48

2-10 SμRE comparisons to relative scale. 50

2-11 Three SμRE I internal reaction chamber geometries. 51

3-1 Center wafer tube mold. 57

3-2 Cap1 fabrication steps. 58

3-3 Illustration of Cap1 after nitride deposition. 59

3-4 Cap2 outside with patterned oxide. 60

3-5 Cap2 fabrication steps. 61

3-6 Illustration of bonding orientation of the three wafers. 62

3-7 SμRE III cross section after bonding (front view). 62
3-8 SμRE III cross section after silicon nitride deposition. 63
3-9 SμRE III cross section after platinum deposition. 64
3-10 SμRE III cross section during and after opening up the release pits. . 64
3-11 SμRE III cross section and full view after final release. 65
3-12 Conceptual illustration of footing in DRIE process. 67
3-13 Various SμRE III final release methods. 73
3-14 SμRE III device completely released with TMAH. 75
3-15 Views of reaction chamber and tubes from broken TMAH-released device. 76
3-16 Non-uniformities in DRIE. 78
3-17 Cross-sections showing footing on buried oxide layer in SμRE II. . . . 79

4-1 Annotated model of SμRE III. 82
4-2 Femlab® model of tubes and heat exchangers with 3D counter-current flow. 84
4-3 Silicon emissivity as a function of temperature. 88
4-4 Reactor heat losses as a function of temperature in vacuum with no gas flow. 90
4-5 Reactor heat losses as a function of temperature in vacuum with gas flow forced convection. 91
4-6 Total reactor heat losses as a function of temperature with and without forced convection. 92
4-7 Thermal efficiency as a function of temperature (with forced convection). 92
4-8 Mounted photocell without filter. 93
4-9 Maximum normalized power vs. emitter temperature for GaSb photocells. 94

5-1 Packaging chips with and without glass frit. 101
5-2 Packaging chuck and complete packaged device. 102
5-3 Model of stop valve constrictions in SμRE III reaction chamber. . . . 104
5-4 Schematic of SμRE I catalyst loading with stop valves [1]. 104

5-5 Mounting of SμRE III to aluminum bars serving as interface with the test setup. 106
5-6 Schematic of fluidic test setup. 107
5-7 Fluidic part of the test setup for SμRE III. 108
5-8 Electrical test rack for SμRE III and bell jar for vacuum testing. . . . 109
5-9 Screen capture of the graphical user interface of the test software. . . 110

6-1 SμRE I TPV power generation test setup schematic. 112
6-2 Pictures of SμRE I mounted to aluminum fixture and GaSb photocell with filter. 112
6-3 SμRE I TPV power generation vs. temperature (with electrical heating). 113
6-4 Radiation spectrum of a grey-body emitter of emissivity 0.7. 114
6-5 Propane combustion rate in SμRE I during test. 115
6-6 Thermal characteristics of three different SμRE III devices. Tests are done with electrical heating, in air and in vacuum. 118
6-7 Thermal characteristics in vacuum compared with model results. . . . 119
6-8 Thermal step response of reactor in air and vacuum. 120

List of Tables

1.1 Energy densities of selected fuels. 18

6.1 SμRE I TPV power generation with autothermal combustion. 115

Chapter 1

Introduction

1.1 Motivation

The revolution of portable computing and electronics in recent years has not been matched by a similar advance in battery technology. The low energy densities of even state of the art batteries are a major hindrance to lengthy use of portable consumer electronics such as laptops, and of military equipment that most soldiers carry with them today. Furthermore, disposing of batteries constitutes an environmental problem, due to their toxic and/or corrosive contents. Hydrocarbon fuels exhibit very high energy densities in comparison, but currently available power generators for converting their chemical energy into electrical energy are too large and bulky to be integrated with portable devices. (The word *generator* will from this point on signify any technology that converts the chemical energy of a fuel into electrical energy by some means.) Much ongoing research is therefore focusing on developing smaller generators that can take advantage of the high energy densities of the fuels, while both being portable and producing high enough power levels to be useful in the aforementioned applications.

Table 1.1 shows the energy density of several fuels and includes two commonly used battery technologies. With gravimetric energy densities more than 60 times that of primary lithium ion batteries, liquid butane and propane can be converted into electricity at a relatively low efficiency and yet have a longer period of usage

Table 1.1: Energy densities of selected fuels (based on the lower heating value for combustion at 25°C) and Li ion batteries.

Energy density	Gravimetric (specific energy) [Wh/kg]	Volumetric [Wh/L]
Propane	12870	6320
Butane	12700	7280
Methanol	5530	4370
Li ion battery	150-200	250-530

without recharging/refueling. This does, however, assume that the generator and the fuel tank are much lighter than the fuel itself. It is also important to realize that if the generator is inefficient, even though it may provide longer usage cycles than batteries, it will produce more heat, assuming near 100% fuel conversion. This will in turn limit the potential applications of the generator.

There exist many approaches to converting chemical energy into electricity. These can be grouped into three categories: (1) direct chemical conversion, (2) mechanically active and (3) mechanically passive heat engines. The first category is comprised of fuel cells, the second of engines and turbines, and the third includes thermoelectric (TE) and thermophotovoltaic (TPV) generators. (While solar cells constitute a potentially portable power source, they rely on the presence of the sun to operate and require relatively large surface areas to achieve significant power levels. They will not be discussed within this thesis other than as a comparison to put TPV into perspective.)

While all of the above generator systems at small sizes are potential replacements for batteries in different applications [13, 18, 8, 24, 23, 31, 32, 20, 30], many of them cannot attain high conversion efficiencies, even under relatively ideal conditions. The significant amounts of waste heat that need to be removed does limit their application to systems where heat removal to the environment is not a problem, but this disadvantage can in some cases be outweighed by the increased energy density. Although they may not be suitable for powering laptops and cell phones, there are many other civilian and military applications where long-lasting, refuelable, and light-weight power sources are needed.

The various technologies have many trade-offs that should be considered when choosing a particular approach, such as efficiency, power density, reliability and lifetime. While many advances have been made in recent years with all of these technologies, laptops are still powered by batteries, and no generators sufficiently small and powerful have yet been built.

1.2 Electrical power generators

1.2.1 Generators and batteries

Electrical generators of various sorts have been used for decades, to produce electricity on-site where the required power is not available. Examples are diesel or gasoline engines with alternators, which can be relocated easily with a vehicle. These are used regularly in construction work and for powering equipment at remote locations. These generators have a clear advantage over batteries, in applications where the weight of the system is not limiting. However, typically at 50 kg or more, these are not truly portable power sources. The challenge then becomes to scale these down drastically, using whichever conversion technology works best for a particular application.

Figure 1-1 clearly illustrates when generators achieve a higher energy density than batteries. The offset due to the generator weight creates a region of low energy density until enough fuel is added to the system. Once the generator's weight becomes insignificant to that of the fuel, the system energy density asymptotically becomes that of the fuel multiplied by the system efficiency, leaving batteries far behind, assuming the efficiency is above a certain minimum. The simple fact that currently available generators are large and heavy, from this graph explains why batteries are used for all small portable devices, but never for large applications, except for providing buffer storage, startup power or emergency backup for generators.

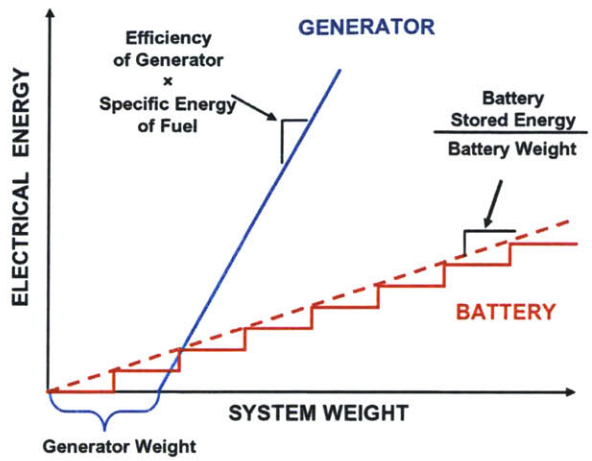

Figure 1-1: Conceptual graph of electrical energy vs. system weight for generators and batteries. The step function for batteries illustrates the sum of discrete electrochemical cells. These steps would be much smaller and the generator weight much larger for current systems.

1.2.2 Important metrics and definitions

The performance of electrical power generator systems (or just generators) can be described by a series of metrics and characteristics. The most important ones are efficiency, energy density, power density, power output, size/weight, working conditions, reliability, lifetime, cost and environmental impact.

The *efficiency* of a generator can be defined in many ways depending on the technology and the various subsystems, but ultimately the important metric is the *overall system efficiency*, which is the useful electrical power output divided by the potential chemical power of the fuel used.

$$\eta = \frac{Electrical\ Power\ Out}{Potential\ Chemical\ Power} \tag{1.1}$$

The latter is given by the *lower heating value* (given in units of Joules per unit mass or volume) of the fuel multiplied by amounts of fuel used per unit time. The factors reducing this efficiency are waste heat losses, unused fuel in the exhaust and reuse of some of the electrical power produced for example for active cooling (e.g. fans), pumps and control electronics. Most systems are designed to operate with a near 100% fuel

usage, which means that all of the non-useful energy put out by the generator is ultimately heat. Thus as an example, a generator that uses 10 Watts of fuel and produces 3 Watts of electrical power has an overall efficiency of 0.3 or 30% and puts out 7 Watts of heat. The operating temperature inside the generator is unimportant to the user. The efficiency along with the power output determines the heat produced by the device, which in turn limits its suitability for different applications. It is possible to have incomplete conversion in a generator, either leaving some fuel gas unreacted, or producing intermediate species that are still usable. The latter, in particular, tends to produce poisonous carbon monoxide, which must of course be avoided. Sufficient catalyst surface area and high temperatures help avoid these problems. Batteries are typically very efficient [23], outputting only small amounts of heat relative to the power they deliver.

The *energy density* of a generator system is simply the amount of useful electrical energy it can deliver without refueling divided by the total mass (*gravimetric energy density* also known as *specific energy*) or volume (*volumetric energy density*) of the system.

$$\Psi\ [Wh/kg\ or\ Wh/L] = \frac{Total\ Electrical\ Energy}{System\ Mass\ or\ Volume} \tag{1.2}$$

(The same definition applies for batteries.) The mass/volume of the system is the sum of the respective values for the fuel, the fuel tank, and the generator itself, including any pumps, fans and control electronics. The mass is usually given for a full fuel tank. Another item that may have to be included here, is the mass/volume of the oxygen and it's container, if atmospheric air is not used for the chemical reactions. Clearly carrying oxygen in the generator system negatively impacts its energy density. The useful electrical energy delivered can also be expressed as the lower heating value of the fuel multiplied by the fuel mass/volume and the overall system efficiency.

The *power density*, not to be confused with the energy density, is the instantaneous electrical power output of the system, divided by the total mass/volume of the system.

$$S\ [W/kg\ or\ W/L] = \frac{Electrical\ Power\ Out}{System\ Mass\ or\ Volume} \tag{1.3}$$

The *volumetric power density* is most often used. For several technologies, such as fuel cells and TPV, where the power output is proportional to an active area, the *power density per unit area* is often quoted. While this is an important metric for those particular energy conversion technologies, the end user, who is likely to view the generator system as a "black box" will only need to know the volumetric power density.

The *power output* (given in Watts) of a generator system is the useful electrical power the system can deliver to a device. Internally the generator may be producing additional power that is used to run e.g. fans and pumps, but this is not useful power to the end user. The power used by a given device may vary widely with time, and a generator can be described by its *maximum* power output (average or peak).

The overall size and weight of a generator is of great importance in portable applications. Again, one must emphasize that all components of the system be included for the metric to be useful. It is also favorable to the energy and power densities that the generator itself constitutes a small fraction of the mass or volume, which should preferably be dominated by the fuel. One potential advantage of generators is that as the fuel is used up, the system becomes lighter. The system volume does not change, however, because the fuel tank is typically rigid.

The working conditions and limits of the generator system are very important in determining its potential applications. For example, if the system utilizes atmospheric air for its chemical reactions, it cannot be operated under water. If components of the system must be cooled to a certain temperature, this may limit the ambient temperature it may be operated in. Likewise, the reliability and lifetime of a generator will determine applicability, but may or may not be determining factors to the success of a technology, as long as they meet certain standards. For comparison, rechargeable batteries are typically very reliable but have a less impressive lifetime. Cost is obviously an extremely important metric for any product. A generator that outperforms batteries but is extremely expensive in comparison, may only be useful in a few cost-no-object applications.

When considering the environmental impact of a generator technology, it is crucial

to put it in perspective. Most generator systems would typically output only CO_2 and H_2O, because it is very important to remove any CO or NO_x from the exhaust stream since these generators are likely to be operated inside. So their environmental impact would mostly be a contribution to the greenhouse effect. However, these portable generators are targeted to replace rechargeable batteries in some applications, which are currently being recharged with electricity that is made at a high percentage by the burning of fossil fuels. The increase in overall CO_2 output is therefore likely to be small, and in any case the levels are small compared to those emitted by cars, air planes, farms and other industries. By comparison, batteries do not output exhaust, but they do contain, as mentioned earlier, corrosive and toxic substances that must be disposed of properly to not negatively impact the environment.

1.3 Thermophotovoltaic technology

1.3.1 TPV overview

Thermophotovoltaic (TPV) generation of electricity is based on a heated emitter radiating photons that are converted to electricity by photocells. The concept was proposed as early as 1956 by H.H. Kolm at the MIT Lincoln Laboratories [15]. It did not, however, gain wide popularity as a research area until the late 1980s, when more suitable low-bandgap photocell materials became available. In recent years much of the TPV related research has focused on optimizing photocell and emitter materials and structures, as well as filters [3, 10, 2] and back reflectors [28] for photon recycling. Complete systems have been assembled for applications ranging from waste heat harvesting in furnaces [11] to portable power generators [14, 7, 19]. System efficiencies as high as 12.3%, have been achieved [11].

The TPV principle is analogous to solar cell technology, the only difference being that a locally heated emitter replaces the sun as a source of radiation for the photocell. Since the photocells now can be placed in close proximity to the emitter, the power density can be 150-1500 times higher than in solar cell systems, despite the much

lower heat source temperature. However, because the emitter temperature is inferior to that of the surface of the sun, the photons emitted in a TPV system have lower energy, and different photocell materials must therefore be used to convert radiated energy to useful electrical energy.

The advantages of TPV systems over other portable power generation schemes are manifold. First and foremost, it is a mechanically passive technology, which makes it simpler to construct and less subject to wear than engines and turbines. It is also practically noiseless. Second, there is no physical contact between the hot and cold zones of the device. As a consequence, TPV systems do not exhibit problems associated with large thermal stresses. In contrast, thermoelectric (TE) devices rely on thermopiles physically connecting the heat source to the thermal sink [24]. Finally, the chemistry associated with the heating of the emitter is usually limited to a simple catalytic combustion. This tends to make design and construction of TPV systems simpler than fuel cells, where complicated chemistries and materials also limit the lifetime of the device, especially when subjected to thermal cycling (on-off switching).

Portable TPV power generators are not yet commercially available, and those that have been developed are relatively large. Scaling down TPV generators opens up a new array of potential applications. There are no fundamental problems caused by scaling, since the optics used at this size are identical to those at large scales. In fact, since the surface-to-volume ratio increases with decreasing dimensions, and TPV power output is proportional to emitter/photocell surface area, nominally the volumetric power density increases when scaling down. Also, the small size combined with an enclosed reactor structure allows for vacuum packaging, which can significantly improve the thermal isolation within the system, thus improving the overall efficiency. Effective vacuum packaging is much more difficult to achieve in larger systems.

1.3.2 Thermophotovoltaic system components

A conceptual schematic of a TPV system is shown in Figure 1-2. It shows the main system components and heat flow paths in a portable TPV generator. Green arrows

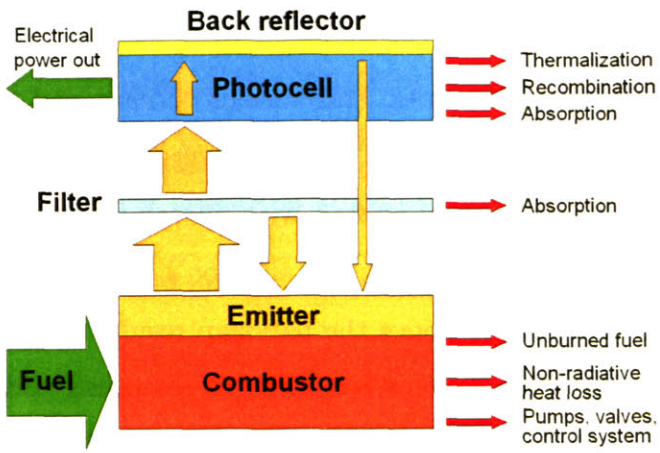

Figure 1-2: Conceptual diagram of TPV thermal management.

signify useful power input and output, orange arrows signify optical heat flow, and the red arrows detail the various waste heat losses. The efficiency of a TPV system is defined in different ways, depending on the application. In waste heat TPV systems [11] and in photocell tests (not complete systems), it is defined as the ratio of electrical power produced to the power radiated from the emitter. This does not include other heat loss paths from the emitter structure. In the TPV system described in this thesis, which falls into the category of portable generators, the efficiency is defined as the ratio of the electrical power produced to the power input in form of heat from the combustion (or for some tests heat from electrical heating). In the future, power spent for auxiliary tasks such as controlling gas flow, pumping air, and photocell cooling, will have to be included for the efficiency to be a good measure of the performance of a portable power source. These are currently powered externally.

Photocell materials

In a photocell (or photo diode) impinging photons with energies larger than or equal to the bandgap of the material contribute to the photo current, which provides the electrical power output. TPV emitters mostly radiate infrared light, so photocell materials with low bandgaps are required to utilize a considerable portion of the radiated spectrum. Silicon, although well suited for the mostly visible solar spectrum,

is not generally useful for TPV because its bandgap (1.1 eV) is too large. Suitable materials for TPV include GaSb, InAs, and various ternary and quaternary III-V semiconductors with bandgaps around 0.7 eV and lower [5, 14, 28, 29].

Photocells are transparent to any photon with energy lower than the bandgap. Each photon with higher energy produces one electron-hole pair that contributes to the electrical current. Any energy above the bandgap results in additional thermalization of the carriers and heating of the cell, without providing additional electrical power. It would therefore be ideal for the energy conversion efficiency if all the incident photons were located slightly above the bandgap in the energy spectrum. However, since radiation at any given wavelength is limited by the black body spectrum at a certain temperature, limiting the emitted spectrum to a narrow peak will result in very low power density. In the context of photocells, power density is given by area (Watts per meter squared), since the power output is proportional to the photocell surface area that the radiation is incident on.

Emitters

The emitter, the source of radiation in the TPV system, is typically heated by the combustion of fuels. Since radiation is largely a surface phenomenon, it is important to ensure that the surface of the emitter not only exhibits a high temperature, but that it also has appropriate material and structural characteristics. Emitter types are typically divided into three categories: broadband, matched and selective [5, 12].

Broadband emitters radiate over the full blackbody spectrum, although at an emissivity lower than 1. They are also known as grey body emitters. Their advantage is that they have the overall highest power density, but this is to the detriment of the efficiency. Photons of energy lower than the bandgap remain unused, and at much higher energies, considerable thermalization occurs in the photocells. To improve the efficiency, filters on the front and mirrors on the back of the photocells can be used to recycle high and low energy photons back to the emitter. The reactors discussed in this thesis behave approximately as broadband emitters.

Many materials can be approximated as grey body emitters. A grey body radiates

a spectrum identical in shape to the black body spectrum for a given temperature, scaled down by a factor ϵ known as the emissivity (a number between 0 and 1, 1 being an ideal black body). When a grey body is illuminated, it absorbs a certain fraction of the incident light. This is called the absorptance, denoted by α, and is equal in value to the emissivity. The rest of the light is either reflected or transmitted.

Matched emitters shape the emitted spectrum without the use of filters. This can be achieved by using materials with special optical properties. For instance, the radiative spectra of certain refractory metals contain very few photons below the bandgap of GaSb [11]. Photonic crystal structures have also been built on the surface of emitters to control the spectrum [3, 16, 12]. When constructed correctly, matched emitters tend to provide a good trade-off between efficiency and power density.

Lastly, selective emitters radiate in a very narrow band just above the bandgap of the photocell material. Rare earth oxides are typically chosen as emitter materials for this purpose, since they have a peculiar radiation spectrum with a single narrow peak. In some cases, this peak matches well with the bandgap of a certain photocell material. An example of such a pair is ytterbia (emitter) and silicon (photocell) [5]. Selective emitters usually give high efficiencies but low power densities.

In general, the performance (efficiency and power density) of TPV systems improves with increased temperature, for two reasons. First, the emitted power is proportional to the fourth power of temperature. Second, except with selective emitters, the peak of the spectrum shifts upwards in energy, allowing a higher percentage of the photons to be turned into electrical power. Typically, it is desirable for the peak of the emitter spectrum to lie somewhat above the bandgap of the photocell material. The photocell material must therefore be chosen according to the emitter temperature, and the temperature of the photocell itself must be kept low (typically not far above room temperature). The recombination rate in the photocell substrate increases with temperature, negatively impacting the efficiency.

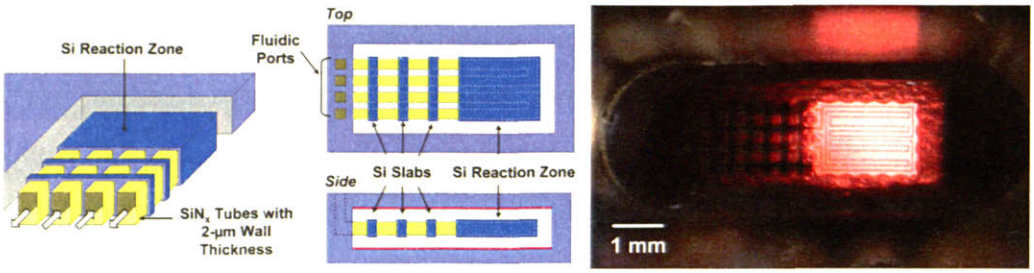

(a) SμRE I schematic.

(b) SμRE I heated to 900°C, substrate at approximately 50°C.

Figure 1-3: SμRE I.

1.4 Background

The work in this thesis builds on the work by Leonel Arana [1] on a catalytic suspended micro-reactor (Sμre). This first generation of the suspended micro-reactor (from now on termed Sμre I) introduced a solution to the difficult problem of achieving good thermal isolation in micro-structures. It achieved this by suspending the silicon reaction-zone from the substrate by thin-walled silicon nitride tubes that also served as fluidic connections for reaction gases. Figure 1-3(a) shows Sμre I in schematic form and Figure 1-3(b) shows the reactor during operation at high temperature. The original purpose of this reactor was hydrogen production from denser energy sources, such as hydrocarbon gases or ammonia, which required high temperature operation of the reactor. For endothermic reactions in one chamber of the device, an exothermic reaction in a second chamber would provide the heat required to keep the reactor at the required temperature. Catalyst was loaded inside the chambers, which were both located inside the silicon reactor, and silicon heat exchangers spanning across the silicon nitride tubes provided a heat flow path from the exhaust gases to preheat the inlet fuel gases.

The ability of Sμre I to achieve *autothermal* combustion (the temperature required for the combustion to take place is provided entirely by the combustion itself) at high temperatures, made it suitable for other purposes as well, such as TE and TPV power generation. It was decided to pursue TPV over TE because of the thermal stresses

that would result from physically connecting the hot reactor to the cold substrate with thermoelectric elements. Furthermore it would require integrating potentially exotic materials into an already complex fabrication process. TPV would allow using of the reactor directly with photocells fabricated separately (obtained commercially) and did not require physical contact between the two elements.

Sμre I was tested in a TPV setup with GaSb photocells, producing net power out, and thus providing a proof of concept for the technology. These experiments are described in Section 6.1. This thesis describes the design, fabrication and testing of a new generation of suspended micro-reactors built specifically for TPV purposes.

Chapter 2

SμRE design

The design of the suspended micro-reactor (SμRE), the combustor-emitter component of the portable TPV micro-generator, is approached in several ways. Thermal considerations common to all generators, scaling of current technology and particular approaches necessitated or allowed by micro-scale dimensions and MEMS (micro-electro-mechanical systems) fabrication technology are all important in understanding the SμRE design.

2.1 Generator thermal management

Certain design rules apply to generator systems of any size, in the thermal domain. Common to all generators is a high temperature zone where chemical reactions take place. In a TPV generator, the temperature required normally exceeds that of any of the other energy conversion technologies, because it relies on radiation, which is proportional to the fourth power of temperature. Maintaining a high temperature in a given zone, it must be well thermally isolated from the surroundings while allowing gas flows to and from it. For this isolation to be effective, heat exchange from the exhaust gas to the incoming gas is a necessity. The only desired heat flow path in a TPV system is radiation, which is therefore enhanced rather than suppressed (as in other types of generators). These design guidelines are illustrated in Figure 2-1.

The pathways for heat loss in any generator system are the following: radiation,

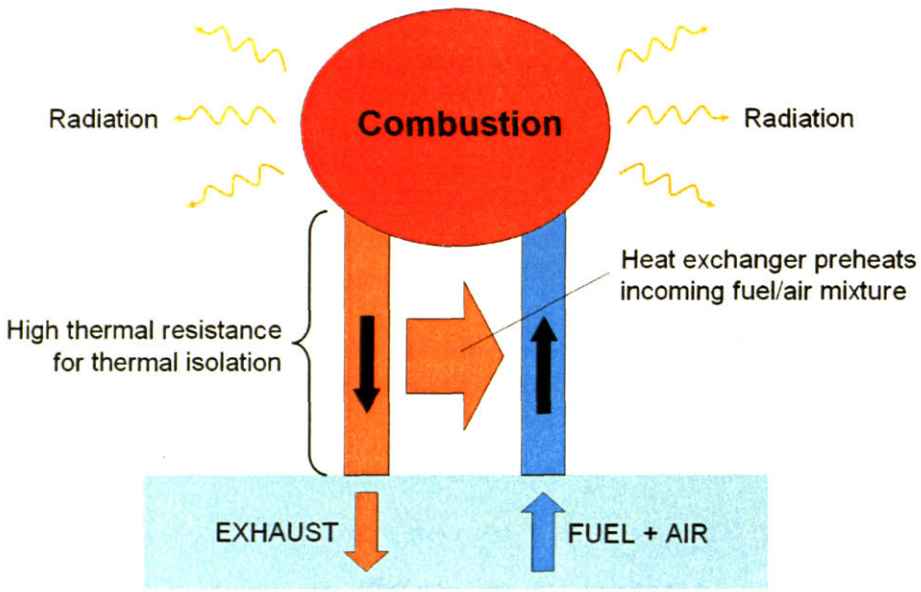

Figure 2-1: General TPV combustor-emitter thermal requirements.

solid conduction, fuel gas forced convection and ambient gas conduction and natural convection. Radiation, if undesired, can be reduced by reflective coatings on the hot zone surface or by surrounding it with reflective surfaces. The emissivity and absorptance of a material are the same. Therefore a highly reflective coating also has a very low emissivity. Solid conduction is usually reduced by applying thick layers of insulation, i.e. materials with very low thermal conductivity. Alternatively, long and narrow structures have a high thermal resistance, as seen from Equation 2.1.

$$R_{therm} = \frac{L}{kA} \tag{2.1}$$

where L is the length and A the cross-sectional area of the structure and k is the thermal conductivity of the material in W/mK. Heat losses by fuel gas forced convection in the system can be reduced by using effective heat exchangers between the incoming and outgoing gas flows. Finally, ambient gas conduction and natural convection can be reduced by surrounding the hot zone with a less conducting gas than air, or can be eliminated by vacuum packaging. In both cases the system must be *fully closed*, meaning that no open flames can be used.

2.2 Scaling

Size and weight are key parameters to any portable system. The energy conversion technologies discussed in Chapter 1 have all been employed with varying success in larger generator systems. Thus one approach to developing a *portable* generator, is to reduce it to a scaling problem. In the context of TPV technology, scaling down existing technology presents both challenges and advantages, due to the particular ways that the physics change with decreasing dimensions. The important aspects to consider are in the optical, thermal, and the fluid mechanics domains. Since the technology does not require moving parts in critical areas, the purely mechanical aspects are not of great importance as a general rule. While a particular fabrication technology may impose more constraints on the scaling, this will be discussed in Section 2.3.

2.2.1 Optics

The optics involved in TPV systems are typically limited to radiative heat transfer between two or more surfaces. (While Section 2.2.2 will treat heat transfer in general, this section concerns the geometric aspects of the radiation.) The surfaces may be complicated systems in themselves, with coatings, filters or photonic crystals to tailor the spectrum emitted or absorbed. However, the structure of these are determined by the spectrum (wavelength), which is independent of the overall size of the system.

In any TPV system it is assumed that a viewfactor close to 1 can be achieved between the emitter and the photocells. This advantage is gained by "scaling down" the emitter from the Sun (solar cells) to a local, containable heat source. Scaling down of TPV systems does not offer any further improvements in that area. The same holds true for the optical cavity that is inevitably created in a high viewfactor, three dimensional system. At very small scales it may actually be more difficult to achieve a high viewfactor due to fabrication constraints.

Optically, other than the particular shape of a system, the scaling problem then reduces to shrinking the gap between the emitter and the photocell. Other than

changing the optical cavity, shrinking this gap has no effect on the radiative transfer until the gap size approaches the wavelength of the light emitted. It has been shown theoretically [21] and experimentally [6] that in this case, a coupling of the evanescent field of the emitter to the photocell surface can greatly increase the radiative transfer. While this may have very interesting applications, it is not a feasible feature to include in the TPV micro-generator described in this thesis. This will be discussed further in the next section.

2.2.2 Heat transfer

The most profound effect of scaling on the heat transfer comes from the change in surface-to-volume ratio. Heat transfer, be it radiative, conductive or convective, is overall proportional to surface area. Therefore, the heat loss relative to system size and weight, is directly proportional to the surface-to-volume ratio of the device. Regardless of the shape of the system, scaling down the dimensions without otherwise changing the geometry, leads to a linear *increase* of this ratio. As an example, for a spherical system, which minimizes the surface-to-volume-ratio for a given size,

$$\frac{A}{V} = \frac{4\pi r^2}{\frac{1}{3}\pi r^3} = \frac{3}{r} \tag{2.2}$$

where $\frac{A}{V}$ is the surface-to-volume ratio, and r is the radius. For a rectangular system:

$$\frac{A}{V} = \frac{2(ab + bc + ac)}{abc} \tag{2.3}$$

where a, b and c are the three edge lengths. In both Equations 2.2 and 2.3, and in general for any three dimensional system, multiplying each dimension by a scaling factor α is equivalent to multiplying $\frac{A}{V}$ by $\frac{1}{\alpha}$. Thus, if α is less than 1, the surface-to-volume ratio is increased by the inverse factor.

This has two significant implications. First, the heat losses from the system, relative to its size, will increase by the factor $\frac{1}{\alpha}$. This in turn lowers the efficiency of the generator. It is therefore crucial to improve the thermal isolation of the reactor

or hot zone. This is typically done with thick layers of insulating material in larger systems. But with scaling down, for the very same reasons, this insulation becomes much less effective. Keeping the insulating material at the same thickness as in the larger system would ensure good thermal isolation, but not only might it be practically impossible to design, it would also increase the system size and weight manifold. SμRE technology solves this problem by the use of long, thin-walled tubes. This will be described in detail in Section 2.3.

The second implication presents an advantage to TPV systems. Since TPV power output is directly proportional to the surface area (of the photocells and the emitter), increasing the surface-to-volume ratio leads to an increased volumetric power density S as shown in Equation 2.4.

$$S = s\frac{A}{V} \tag{2.4}$$

where s is the power per unit area of the emitter-photocell pair, which is dependent on the emitted spectrum, the photocell material and structure, and the viewfactor, but not on scaling. While this increase in volumetric power density is an added advantage of smaller systems, it also suggests that larger systems could benefit from being replaced by clusters of smaller ones, thus achieving an overall higher power density. Again, this depends further on the limitations of the fabrication technology.

Another advantage to smaller systems is that vacuum packaging is more feasible. The purpose of vacuum packaging is to remove the air conduction and natural convection heat loss path between the hot and cold parts of the generator. What constitutes an effective vacuum level for a particular system depends on the gas and the size of the cavity between the cold and hot zones. To achieve an effective reduction in gas conduction and natural convection, the mean free path must be longer than the largest cavity dimension D. Equation 2.5 gives the mean free path of an ideal gas, where λ is the mean free path, k_B is the Boltzmann constant, T is temperature, P is pressure and d is the average diameter of the molecules constituting the gas.

$$\lambda = \frac{k_B T}{\sqrt{2}\pi d^2 P} \tag{2.5}$$

Combining this equation with the condition $\lambda > D$ then imposes the following condition on the pressure:

$$P < \frac{k_B T}{\sqrt{2}\pi d^2 D} \tag{2.6}$$

As a consequence of smaller cavities not requiring as low of a pressure level, portable generators can benefit from vacuum packaging, whereas most large systems have to resort to other means, such as using an ambient gas with lower heat conductivity.

Coupling of the evanescent field through sub-wavelength gap size has the advantage of increased radiative (useful) heat transfer for TPV systems. However, the challenges associated with this are many. First and foremost it is essential to employ vacuum packaging, since the thermal resistance of any gas in between the two surfaces is minimal and would result in very large gas conduction heat losses. Second, controlling the gap size without touching the surfaces directly (which would be catastrophic to the photocells) is complicated. This has so far been achieved by using very thin silicon dioxide spacers, but despite being very small, the diameter is greater than the thickness, which by Equation 2.1 leads to a very low thermal resistance. No solution has yet been published for this challenge. As will become clear in Section 2.3, the SμRE cannot support any direct physical contact between the hot and cold zones (other than the tube section), due to the fragility of the suspended tubes and the slight movement of the reactor with changing temperature. The reactor also moves slightly from acceleration and gravity, making other means of controlling a sub-micron gap unlikely to work.

2.2.3 Fluid mechanics

The fluid mechanics of the fuel gases in a generator are important primarily because they determine the flow resistance and therefore back pressure of the system. The Reynolds number, given in Equation 2.7, is a unitless expression that indicates how the flow behaves.

$$Re = \frac{\rho v_s L}{\mu} \tag{2.7}$$

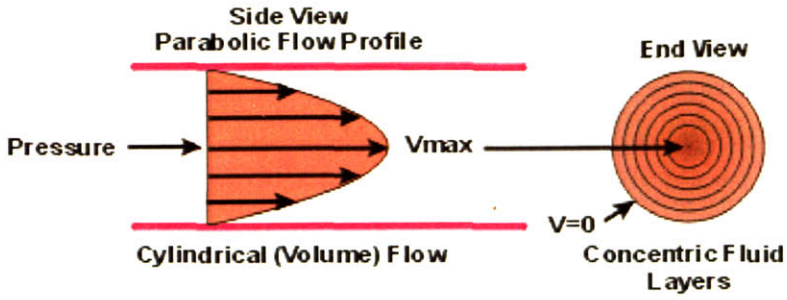

Figure 2-2: Conceptual representation of laminar flow velocity profile (*http://www.cvphysiology.com/Hemodynamics/H006.htm*).

where ρ is the density of the fluid, μ is the viscosity, L is the characteristic length (the diameter for a circular tube) and v_s is the mean flow velocity (averaged over a cross-section perpendicular to the flow direction). For Reynolds numbers less than about 2000 (in tubes), viscous forces dominate, and the flow can be assumed fully laminar. For numbers higher than about 4000, the inertial forces of the gas will dominate, and the flow will be fully turbulent. For sufficiently small dimensions, which is typically the case in micro-systems, the flow is laminar.

Laminar flow is smooth and constant, with a parabolic cross-sectional velocity profile, which goes to zero at the side-walls, as shown in Figure 2-2. The domination of viscous forces creates a higher flow resistance, which leads directly to a higher back pressure in the system. Fuel gases are typically driven through the system by the pressure in the fuel tank. For compressed liquid fuels, this pressure corresponds to the vapor pressure of the gas. As an example, butane has a low vapor pressure of only about 250 kPa at room temperature. Thus, for a back pressure of 150 kPa (1.5 atmospheres), pure butane can no longer be used without supplemental pumping. Additionally, pumps must typically be used to inject air into the fuel stream, and more energy must be spent for the pumping for high back pressures. All energy spent on pumping decreases the overall system efficiency.

2.2.4 Conclusion on scaling

Treating portable power generators as a case of scaling down already existing technology is at best a good starting point or partial solution. While the approach can be used to get important answers and guide design to some extent, it is important to realize that key differences exist that either require new thinking in design to avoid, or that can be taken advantage of only if deviating from traditional design rules. Furthermore, at sufficiently small scales, fabrication techniques impose very different constraints on geometrical shapes and layout than with large scale machining. This limits how directly scaling can be applied.

2.3 SμRE III design

The design of the latest generation of the suspended micro-reactor, SμRE III, will now be described in detail. It is fundamentally based on the first generation of the reactor, and a comparison between the two will be given towards the end of the section, highlighting key improvements.

2.3.1 MEMS technology

Micro-electro-mechanical systems (MEMS) or micro-fabrication, was chosen as the enabling technology for SμRE for several reasons: micro-scale dimensions, high temperature materials and the potential for mass fabrication. The choice of MEMS should always be carefully justified because of the high equipment and research costs, and ultimately a requirement for very large scale production to become profitable. For some applications, methods such as micro-scale injection molded plastic may present a much cheaper and fully functional alternative.

First and foremost, the TPV micro-generator was designed to be very small in size. Although the overall size of the reactor is on the order of millimeters, the smallest dimension is on the order of microns. As explained in Section 2.2.2, thick layers of insulating material cannot effectively be used in very small systems to reduce

solid heat conduction. Rather SμRE relies on the concept of a long and narrow suspension structure to achieve this, the width of this structure being on the order of microns. Second, the reactor must be able to withstand temperatures in excess of 800-900°C. Silicon and other materials accessible in micro-fabrication are compatible with this requirement, whereas e.g. plastic materials clearly are not. Third, should this technology become a viable commercial product in the future, the market for longer lasting alternatives to batteries is large, both in military and civilian applications. This both demands and thus justifies mass fabrication.

Silicon based micro-fabrication is a mature technology with many techniques available for approaching the design. But it also imposes many restrictions on geometry. It is mostly limited to linear extrusions of 2D patterns by etching. Methods such as wafer bonding and sacrificial molds are therefore used to create more complex 3D structures, which add to the complexity of the fabrication. The SμRE design will now be presented, with a detailed discussion of important design features. A comprehensive description of the fabrication process will be given in Chapter 3.

2.3.2 SμRE III: Important design features

Four crucial features of the reactor will be discussed in detail here. They are the silicon nitride suspended tubes, the silicon heat exchangers, the reaction chamber (also the emitter) and the metal resistive heater. In addition, a brief discussion will be given of the packaging scheme employed for the purpose of testing while protecting the fragile structure. Figure 2-3 shows four 3D model views of SμRE III. All of the important design features can seen in these pictures (not the packaging). Other details about the design, especially relating to moving from an idealized design to a micro-fabricatable structure, will be discussed in Section 2.3.3.

Suspended tubes

The heart of the SμRE technology is the suspended tube design. It allows the reaction chamber or hot zone to be connected to the substrate only by a set of long and thin-

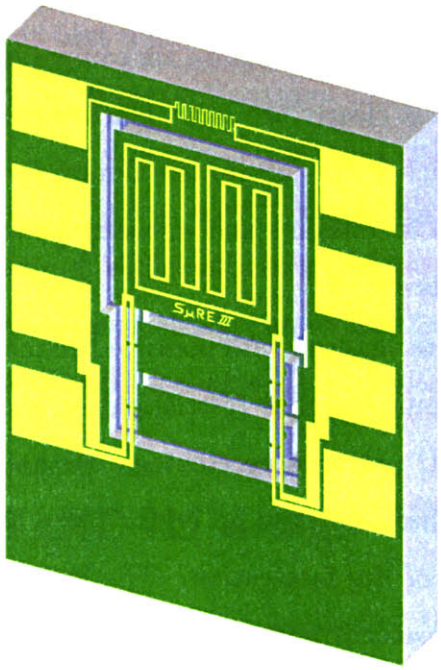

(a) SμRE III front side with resistive heater.

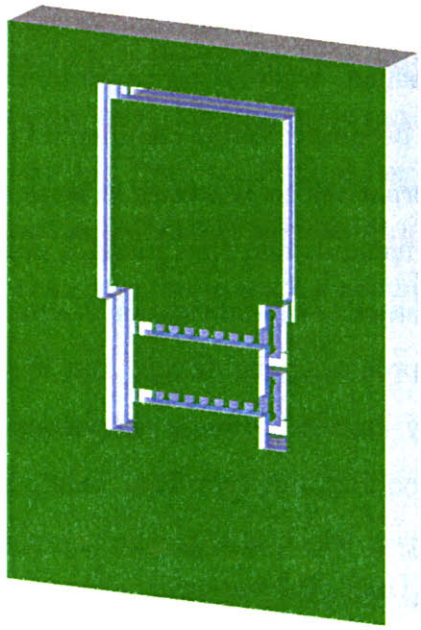

(b) SμRE III backside with fluidic connections.

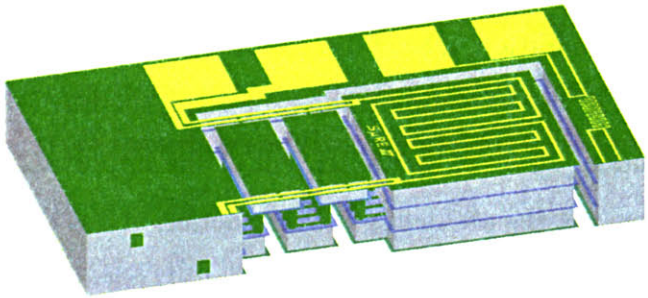

(c) SμRE III side view with silicon nitride tubes.

(d) SμRE III internal flow channel system (seen from back side).

Figure 2-3: SμRE III model. Color scheme: silicon=grey, silicon nitride=green, silicon dioxide=blue, metal=yellow.

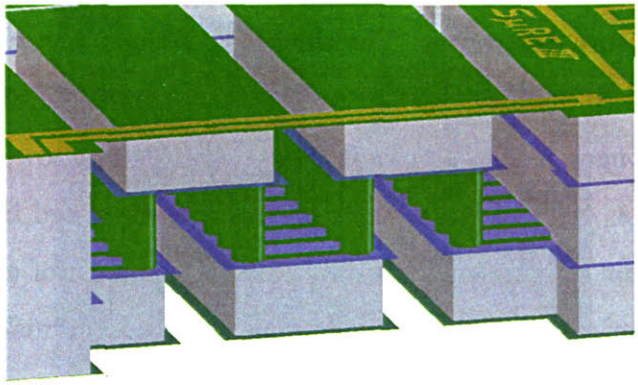

Figure 2-4: SμRE III silicon nitride tube section with heat exchangers.

walled silicon tubes. The tubes are suspended or free-standing between the silicon substrate, heat exchangers and reactor, or alternatively the reactor is suspended from the substrate by the tubes. While the tubes provide a very high thermal resistance to help thermally isolate the structure, they also allow fluidic access to the reactor. This design solves the problem of maintaining steep thermal gradients in micro-scale devices. Figure 2-4 shows a close-up picture of the tubes.

Silicon nitride was chosen as the tube material for three reasons. First and foremost it has a low thermal conductivity, which increases the thermal resistance beyond what is provided by the high aspect ratio (see Equation 2.1). The thermal conductivity of the silicon nitride used is about 15-30 $W/m.K$, whereas that of silicon is 150 $W/m.K$. Secondly, a silicon rich, low stress nitride was used to avoid stresses that could easily break the tubes. For comparison, thermally grown silicon dioxide exhibits high compressive stress. Furthermore, this nitride has a thermal expansion coefficient of about $2.3 * 10^{-6}$ per Kelvin, which is close to that of silicon ($2.8 * 10^{-6}$ per Kelvin). Third, and most fundamentally, because the tubes are fabricated in a molding process where the mold is created in silicon, a different material is required for the tubes, so that they can withstand the removal of the silicon mold at the end of the fabrication process.

A circular cross-section was chosen for the tubes, because it is the optimal shape to achieve a high burst pressure. In tubes with rectangular cross-section, on the other hand, stress concentrations tend to develop at the corners, leading to a lower

tolerance to high pressure differences. The thickness of the tubes, ranging between 2 and 4 μm, was picked to balance thermal resistance with structural strength. While a thicker tube is stronger it also conducts heat more readily, lowering the thermal isolation of the reactor. The length of the tubes will be discussed in Section 2.3.3 as it is determined by the fabrication process. Given the length of each tube, 4 tube sections in thermal series were used as a balance between thermal isolation on the one hand and overall system size and flow resistance or back pressure on the other. There are 4 complete and separate flow paths in the device, resulting in 8 parallel tubes at each stage.

The suspended design minimizes stress problems related to expansion during heating of the reaction chamber. Since the reactor is only physically constrained at one end, it is free to expand and move, without causing any strain and breakage. Like a diving board, fixed at one end, the suspended reactor will move slightly with accelerations, in particular perpendicular to the top/bottom surface, which is the direction of lowest stiffness. Experimentally the tubes have been found to be robust enough to withstand acceleration from normal handling.

Heat exchangers

Heat exchange between incoming and outgoing gas flows is important to avoid high heat losses through the exhaust. The 8 parallel tubes represent 4 input/output pairs, which are connected physically and more importantly *thermally* by massive silicon heat exchangers. As is shown in Figure 2-5, the gas flow path through the heat exchangers has a relatively high aspect ratio (length to perimeter), leading to good heat exchange between the gas and the walls. The high thermal conductivity of silicon ensures good heat conduction between the various flow paths. The 4 tube sections allow 3 heat exchangers to be placed in the structure.

Because the exhaust gases carry large amounts of heat relative to the conductive heat loss paths, using some of this energy to preheat the input fuel air mixture greatly enhances the thermal isolation and thus the efficiency of the system. The silicon heat exchangers are covered on both top and bottom by a thin film of silicon dioxide and

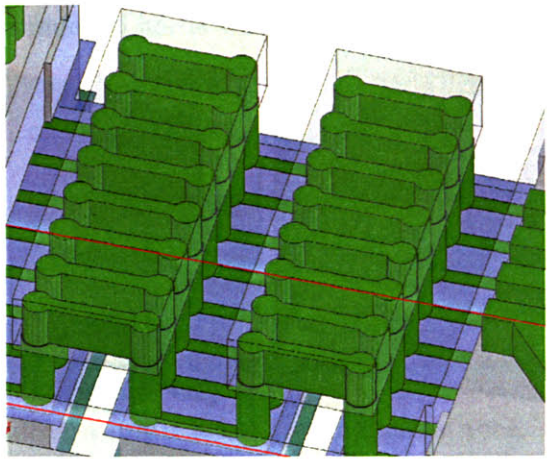

Figure 2-5: SμRE III heat exchangers with nitride covered channels. (Top heat exchangers are here shown transparent to display the inner channel.)

on the top by an additional layer of silicon nitride, of the same thickness as the tubes. This is a consequence of the fabrication process.

Reaction chamber

The SμRE reaction chamber consists of a silicon box with a complex network of flow channels inside. The channel walls are lined with catalyst, and the combustion of fuel and air takes places inside it. The heated reactor then serves as the emitter for the TPV generator. As with the heat exchangers, the high thermal conductivity of silicon ensures good thermal uniformity across the outer reactor surface, avoiding hot spots caused by localized reactions inside. A higher temperature tends to develop where the fuel first encounters the catalyst, due to the high concentration of reactants. Figure 2-6(a) shows the reaction chamber seen from the outside, and Figure 2-6(b) shows the network of flow channels inside it, displayed through the silicon nitride that lines the inside surfaces everywhere. The nitride is present due to the molding process that creates the free-standing tubes. Each overall flow path splits into two once inside the reactor, to increase the surface area where catalyst will deposit. The complex crossings of the flow paths is necessary to ensure equal flow lengths and resistances for each flow path. Near the entrance to the chamber is a set of fluidic stop valves

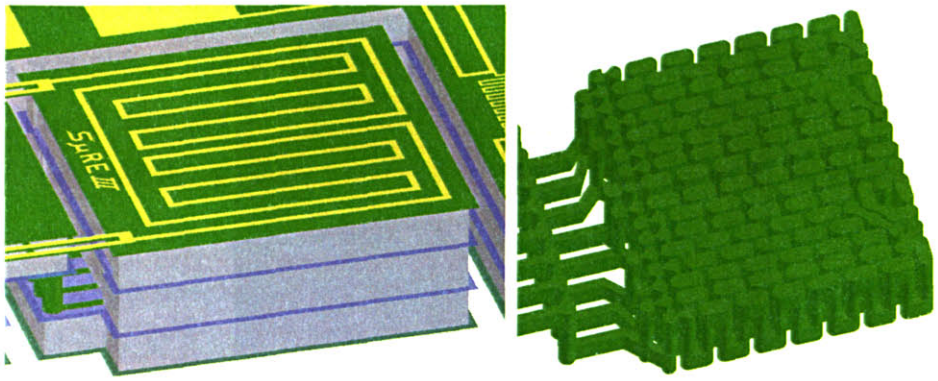

(a) SμRE III reaction chamber with resistive heater.

(b) SμRE III reaction chamber internal flow network. Fluidic stop valve constrictions for controlled catalyst loading can be seen on the left side.

Figure 2-6: SμRE III reaction chamber.

that are used for loading catalyst into the reaction zone. These will be discussed further in Chapter 5.

The reactor is covered on the top and the bottom by thin films of silicon dioxide underneath silicon nitride. These are present due to the fabrication process. They do not significantly change the emissivity of the underlying silicon, which is about 0.7. The metal resistive heater on one side of the reactor is highly reflective, but because it covers only a small percentage of the surface area, it only reduces the emissivity by a small amount.

Metal resistive heater

SμRE III has two metal resistors that can be seen in Figure 2-3(a) and 2-3(c). The substrate resistor is used for monitoring the substrate temperature, while the reactor resistor has two functions: monitoring the reactor temperature and preheating it. By driving a current through the reactor resistor (resistive heater), thermal power is dissipated into the reaction chamber, a necessary tool for initiating the combustion reaction. Once the reaction has started, the electric heater is turned off, and the combustion provides the heat required to keep the reactor at high enough temperature

for the reaction to continue. This is termed *autothermal combustion.* The reactor resistive heater leads cross directly from the substrate to the hot zone on silicon nitride bridges. The bridges run next to the heat exchangers rather than over them (which was the case with SμRE I), and they are anchored to the two heat exchangers on the front of the device for stability. This configuration is used to minimize heat losses through the highly thermally conductive metal. The alternative, running the metal across the heat exchangers, would reduce the length of the heat flow path to the 3 narrow gaps, yielding a much lower thermal resistance.

Temperature is measured in the resistor by sending a current (usually small, unless the heater is active) through it, and then measuring the voltage that develops across it. This allows calculation of the resistance of the heater by Ohm's law. Metals change resistivity with temperature, and the temperature can then be deduced from a resistance vs. temperature plot for the particular metal in use. Such a curve is shown in Figure 2-7 for platinum. The normalized resistance r_{norm}, given in Equation 2.8 is used because each reactor heater has a slightly different resistance.

$$r_{norm} = \frac{R(T) - R_0}{R_0} = \frac{\Delta R}{R_0} \tag{2.8}$$

where $R(T)$ is the actual measured resistance at a given temperature, R_0 is the resistance measured at room temperature, and ΔR is the change in resistance, positive for increasing temperature. Platinum is used for the SμRE III metalization because it can withstand high temperatures in an oxidizing atmosphere, and because the resistance vs. temperature curve is close to linear.

For better temperature measurement accuracy, both resistors have a 4-point probe configuration. This allows the current to be driven through one set of leads while the resulting voltage is measured across the other pair. This ensures that only the voltage, and hence the resistance, across the resistor itself is measured, leaving out the leads. Especially for the reactor resistor, including the lead resistance would give a slightly low measurement of temperature, because the leads become cooler farther away from hot zone. The 4-point probe concept is illustrated in Figure 2-8. V_0 is the driving

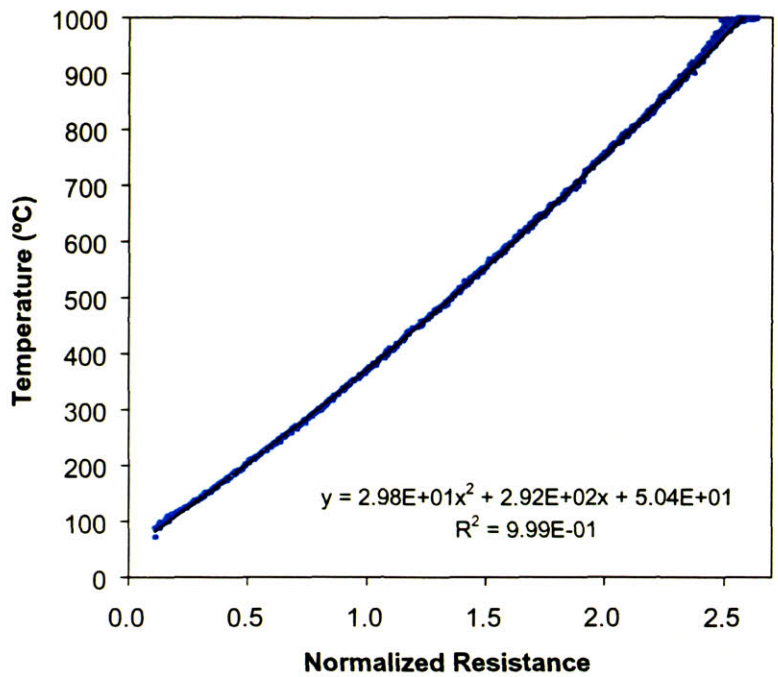

Figure 2-7: Plot of resistance change with temperature, with quadratic fit, in a platinum thin-film resistor [1].

voltage, resulting in a current I_0 that also goes through the resistor of interest R_H. V_1 is measured by a voltmeter, which is essentially an open circuit, and thus I_1 is zero. V_1 is therefore the voltage across R_H. The R_L are the lead resistances.

Packaging

SμRE can in some ways be a very fragile structure due to the thin-walled tubes that suspend the reaction chamber from the substrate. While the tubes can withstand the acceleration of the reaction chamber at normal handling, any direct physical contact with the suspended structure will cause it to break. A spacer chip is therefore added to each side of the die (see Figure 2-9), to protect it from physical contact when lying on a flat surface and while being handled. Both chips have open areas to allow electrical connections to the metal pads, and one side has holes for the 8 fluidic connections. The holes are circular to facilitate catalyst loading with a syringe. The chips are covered with a thin film of silicon dioxide to ensure electrical isolation.

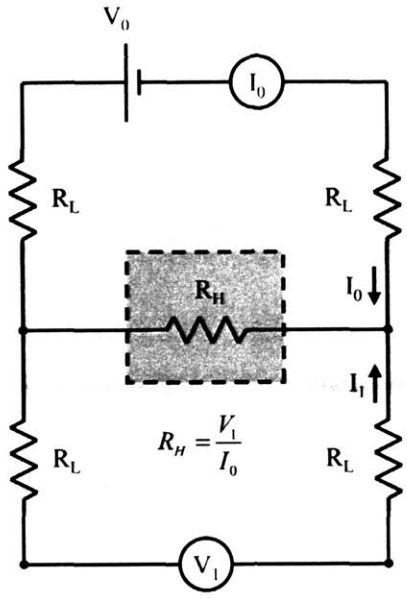

Figure 2-8: 4-point probe circuit diagram.

2.3.3 From design to fabrication process

MEMS fabrication technology imposes many restrictions on the design. Most striking is perhaps the tube configuration. The silicon mold for the circular tubes can only be etched vertically through the wafer, perpendicular to the wafer surface. Whereas SμRE I employed tubes of rectangular cross-section etched horizontally in the wafer, there is no reliable way of achieving smooth-walled circular horizontal tubes. Furthermore, connecting the flow paths through the wafer can only be achieved by bonding one wafer to each side that has connecting channels etched into it. The result is the peculiar, winding flow paths of SμRE III.

The length of the tubes and therefore also to some extent the length of the whole flow network, is determined by the thickness of the wafers used. In particular, the center wafer thickness is of great importance. A thicker wafer yields longer tubes and better thermal isolation. However, wafers of very great thickness are impractical to use for etching all the way through. The possible range of thicknesses is therefore around 500-900 μm.

During the process of growing silicon nitride inside the tube molds, it is in fact

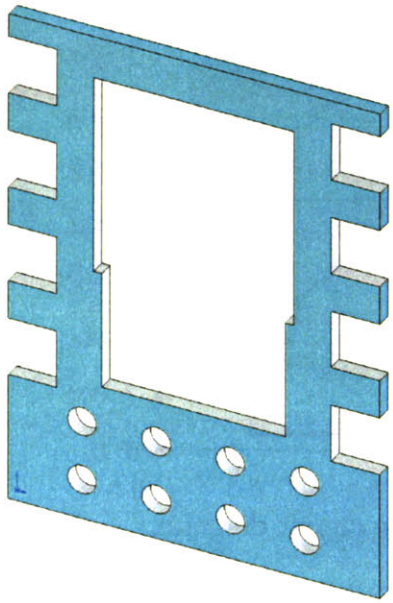

(a) Backside protection chip.

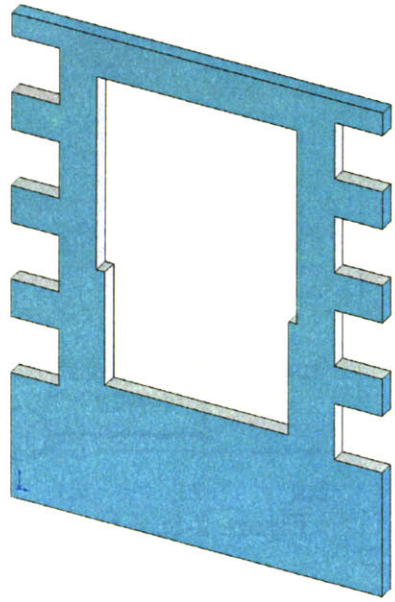

(b) Front side protection chip.

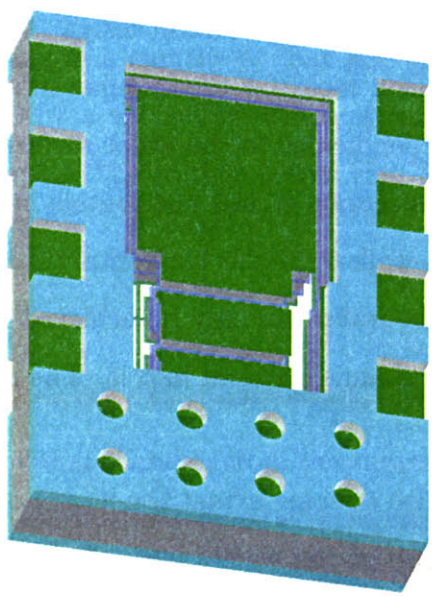

(c) SμRE III packaged, seen from the back.

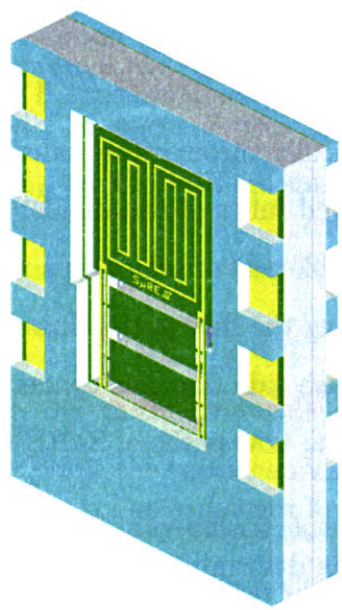

(d) SμRE III packaged, seen from the front.

Figure 2-9: SμRE III protected with packaging chips.

deposited on all surfaces that are exposed at that point in the fabrication process. This includes the whole flow path through the reactor, as well as the entire top and bottom surfaces. This is the reason why the heat exchangers and the reaction chamber are all covered with nitride. This nitride has two functions other than serving as the tube material: providing sturdy bridges for the resistive heater leads and serving as an etch mask in the final release.

In an ideal world, for the TPV micro-generator, SμRE III would be surrounded on all sides by photovoltaic cells. But as is apparent from Figure 2-3(a) and 2-3(b), the reactor is surrounded on all sides (except the top and bottom) by the substrate. This is the case for two important reasons. First, the substrate must contain 8 electrical contact pads, the substrate resistor and 8 fluidic connection holes. All of these have to be large enough and spaced far enough apart to be accessible to the test equipment. At the same time it is desirable to minimize the overall space used so that many devices can fit on each stack of wafers. Laying these features out around the reactor allows for a very compact design. Second, because of the fragility of the tube section, the reactor must be protected against physical contact with external objects during handling and testing. The surrounding substrate, in conjunction with the packaging chips, achieves this goal. As a result, photovoltaic cells can only be placed on two sides of the reaction chamber. Thin reflective mirrors could be inserted vertically in the gaps around the reactor to try to recuperate some of the otherwise lost radiation.

A detailed description of the entire fabrication process is given in Chapter 3. The particular geometries of the features discussed in this section, as well as other details, are more easily understood in the context of the fabrication.

2.3.4 SμRE III evolved from SμRE I

A comprehensive description and study of SμRE I is given in Leonel Arana's doctoral thesis [1]. Here it will suffice to explain the major differences between the two generations of suspended micro-reactors. It should be mentioned that while SμRE I was originally developed for hydrogen production, SμRE III was designed with TPV power generation in mind. This explains the first key difference between the two:

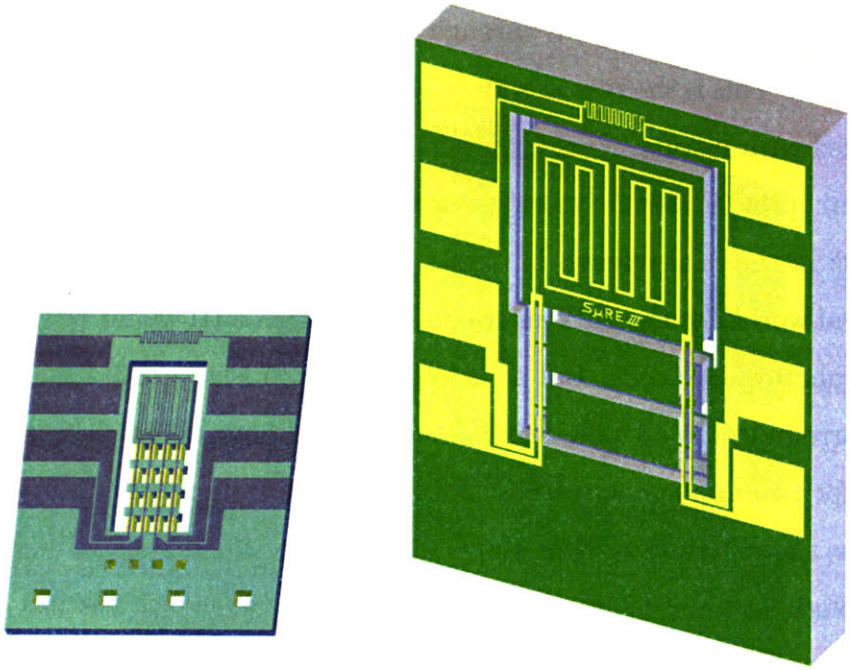

(a) SμRE I. (b) SμRE III.

Figure 2-10: SμRE comparisons to relative scale.

the size. The top and bottom surface areas of the SμRE III reaction chamber are 5x5x2 mm, while those of SμRE I are only 1.5x2.5x0.5 mm. It is difficult to obtain photocells with dimensions as small as the latter, and SμRE III was designed to be used with a wider range of cells, as well as produce a higher total power output. The two reactors are shown next to each other in Figure 2-10 to relative scale. As a result of the larger size and reactor weight of SμRE III, eight parallel tubes are used to assure sufficient mechanical strength, whereas the first generation only has 4. This allows for 4 separate flow circuits rather than just two, adding to the versatility of the reactor.

Another key difference is that the first generation had tubes with rectangular cross section, whereas those of SμRE III are circular. The change was made because the burst pressure of the rectangular tubes was quite low (around 2 atmospheres difference across the tube wall). If the tubes had been perfectly rectangular, the burst pressure would have been higher [1], but many imperfections resulted from the fabrication

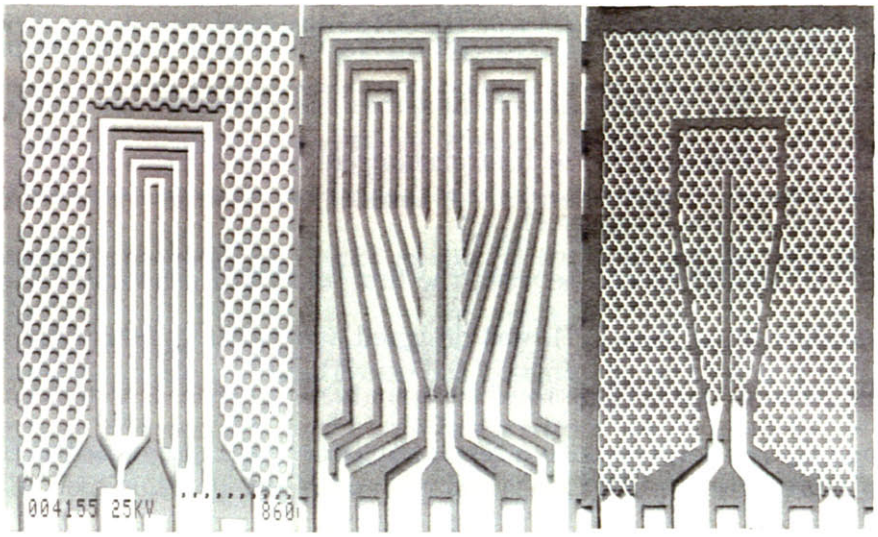

Figure 2-11: Three SμRE I internal reaction chamber geometries.

process, especially at the corners, leading to high stress concentrations. The circular tubes were designed to solve this problem. A consequence of the choice of cross-sectional shape is that while SμRE I has straight tubes and flow channels parallel to the wafer surface, SμRE III is forced to use a meandering "3D" configuration. As will be seen from the fabrication process, while this solves some problems with the former process, it is a more complex design with many fabrication challenges.

SμRE I employed in its reaction chamber various layouts of posts and channels to increase the surface area where catalyst could attach, in this way increasing the throughput of burned fuel possible. Arbitrary geometries could be used because the chamber was etched into the silicon leaving a small amount of silicon at the bottom (see Figure 2-11) and then capping the top with another wafer. SμRE III on the other hand relies on etching straight through the center wafer, so any posts or walls would fall out. However, the network of flow channels in the third generation is quite extensive with a large surface area. If desired, some posts could be placed in the capping wafer channels, but this would increase the already high back pressure of the system.

As can be discerned from Figure 2-10(a), the resistive heater leads in SμRE I are located straight above each tube. The result is that the metal is only free-standing

(on nitride) between the heat exchangers, producing a formidable heat loss path with a lower thermal resistance than that of the tubes. In SμRE III the metal runs on thin, long nitride bridges next to the heat exchangers, reducing this heat loss path to negligible proportions (see Chapter 4).

These are the key differences between the first and third generation reactors. A second generation reactor, SμRE II, was designed and partially fabricated but then abandoned for reasons that will be touched upon in Chapter 3. It was essentially an identical design to SμRE I, but with a reaction chamber the size of SμRE III.

2.4 Applications of SμRE III

SμRE III was designed specifically to be the combustor-emitter component of a portable TPV micro-generator. However, it is a versatile design with other potential applications. One of these is to serve as a hydrogen production unit for fuel cells, the intended purpose of SμRE I. The volumetric energy density of hydrogen gas is quite low, due to the fact that it is very hard to compress. It cannot be compressed to liquid form without extreme cooling, and the storage tanks for high compression must be very sturdy and therefore heavy. Hydrogen storage in metal hydrides [25] is one partial solution to the problem, but even these do not have very high energy densities. Hydrogen is therefore a difficult fuel to include in a portable generator system, unless it comes from a denser source.

Denser sources of hydrogen include ammonia, NH_3, and hydrocarbons such as propane, C_3H_8, and butane, C_4H_{10}. By extracting hydrogen from these easily compressible gases, it can then be fed to a fuel cell for direct chemical-to-electrical energy conversion. There are different methods for extracting the hydrogen: ammonia cracking, and steam reforming and partial oxidation of hydrocarbons. The two first are endothermic reactions, while the third is exothermic, all of them requiring high temperatures to work efficiently. As with combustion, the exothermic reactions are easily carried out in SμRE III with the appropriate catalyst, running autothermally due to the good thermal isolation of the structure. For the endothermic reactions, another

heat source is required. Because SμRE III has 4 separate flow circuits, this heat can be supplied by running a combustion reaction in one or more of the circuits, as necessary. Heat is transfered between the streams inside the reaction chamber (and the heat exchangers) through the silicon. A comprehensive study of these reactions in SμRE I was carried out by Leonel Arana [1] and will not be discussed in more detail here.

As a simple combustor, SμRE III also has potential to be used as a thermoelectric power generator. Thermopiles would have to span from the hot zone to the substrate, and the tube configuration would have to be redesigned to compensate for stresses. Otherwise the rigid connection created by the thermopiles would cause breakage at high temperatures. Integrating the thermoelectric materials deposition into the fabrication process would also introduce challenges. In general, SμRE III is a candidate for chemical reactions that require high temperatures to function. It is all made possible by the suspended tube design.

Chapter 3

SμRE III fabrication

The fabrication process for SμRE III is a 3 wafer, 11 mask procedure (some of these 11 masks are used several times).. The process is complex from two points of view. On the one hand, the three-dimensional geometrical layout can be difficult to grasp, in particular understanding the transition from the planar masks to the final device. In Section 3.1 the process flow is described, accompanied by 3D models and cross-sections to explain this transition. On the other hand, there are several challenges associated with carrying out certain fabrication steps. These critical fabrication steps are described in detail in Section 3.2. Pictures of fabricated devices are presented in Section 3.3, and a discussion of the evolution of the fabrication from previous generations of SμRE is given in Section 3.4.

3.1 Fabrication process

The fabrication process of SμRE III utilizes 3 DSP (double-side polished) (100)-orientation silicon wafers. There are 44 dies per wafer, but only individual dies are shown in this section for clarity. First each wafer undergoes several fabrication steps, before they are bonded together. Then the bonded triple-stack undergoes further steps before the device wafer is finished. The planar masks referred to in this section are found in Appendix A. A detailed step-by-step flow chart of the fabrication process is given in Appendix B.

3.1.1 Center wafer: tube mold

The center wafer in the triple stack serves as the mold for the silicon nitride tubes. Several thicknesses were used for the center wafer, varying from 650 to 800 μm. Thick photoresist patterned with Mask *TUBES* is applied to the wafer's front side, and the wafer is then etched all the way through by using Deep Reactive Ion Etching (DRIE). The result is shown in Figure 3-1(a). Figures 3-1(b) and 3-1(c) illustrate how the tube mold works. After bonding, the green areas are where the nitride will eventually be deposited, because they are part of the open flow paths. All the non-circular holes through the wafer (except the square holes towards the bottom of the die that are part of the fluidic connections network) are enclosed cavities after bonding and are only opened up after the nitride has been deposited. These will be termed the *release pits* from now on. Figure 3-1(d) further shows how the final release etch will remove the silicon grid around the tubes and the reaction chamber, leaving the tubes free-standing and the reaction chamber intact. This is only an illustration to explain the concept of tube mold, and the center wafer by itself (unbonded) will not have the nitride present. The top and bottom surface of the center wafer does not have any film on it prior to bonding.

3.1.2 Capping wafer #1

The first capping wafer (Cap1) forms what will be referred to as the back side of the device. It forms the fluidic connections to it. It also provides, like the other capping wafer, the connections between the tubes, inside the heat exchangers. The wafer, 650 μm thick, is covered with a thin film of silicon dioxide (0.5 μm) on both sides. The first step is to etch the oxide (BOE:buffered oxide etch) using thin photoresist patterned with Mask *CAP1OUT* (see Figure 3-2(a)). The photoresist is then stripped and new thick resist is applied on both sides. The inside is patterned with Mask *CAP1IN* and the outside with Mask *CAP1THRU*. After removing the oxide with BOE, DRIE is then used to etch 400 μm from the inside and then 250 μm from the outside to make the fluidic connections. The result is illustrated in Figures 3-2(b), 3-2(c) and 3-2(d).

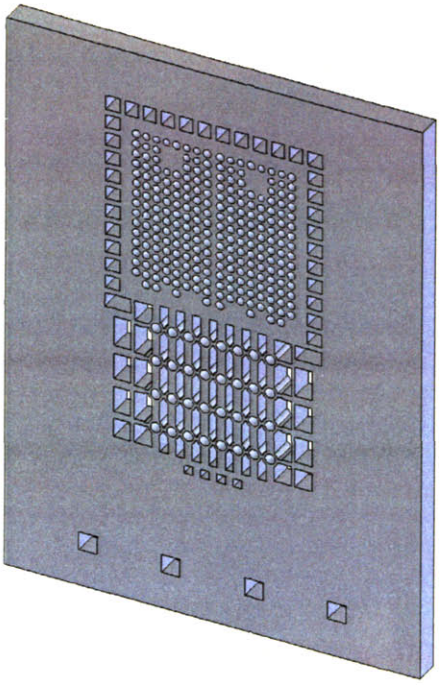

(a) Center wafer tube mold.

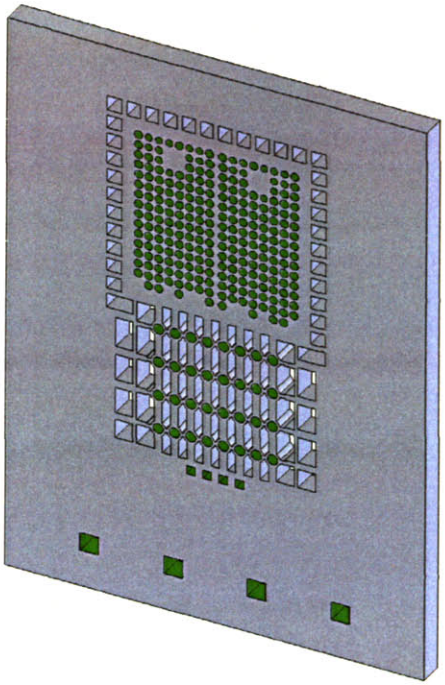

(b) Illustration of where the silicon nitride will be deposited after bonding.

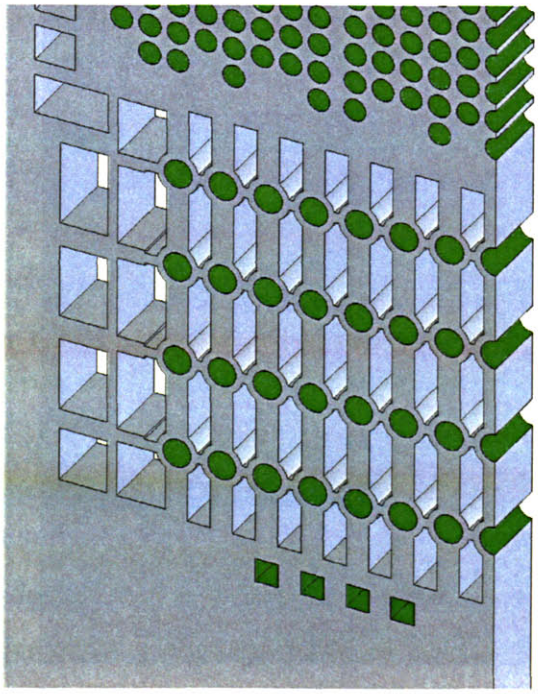

(c) Enlarged cross-section of 3-1(b).

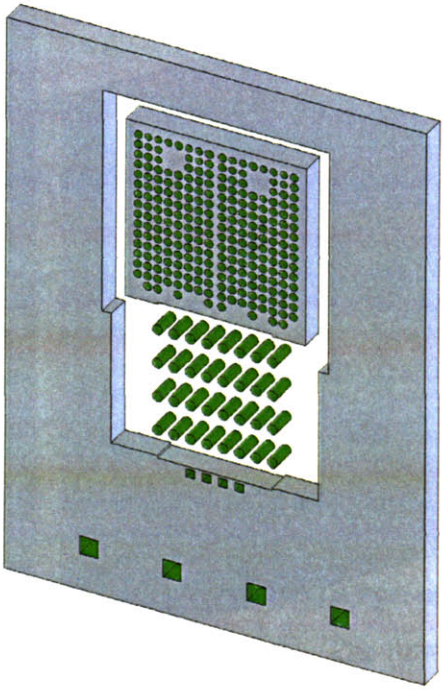

(d) Illustration of free-standing tubes after final release.

Figure 3-1: Center wafer tube mold and silicon support grid for tube section and reaction chamber.

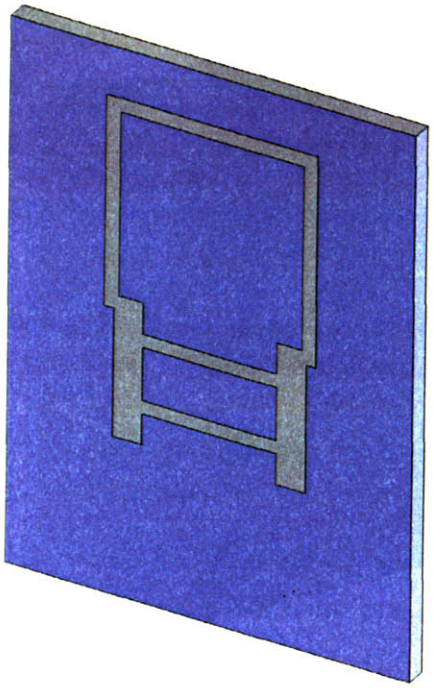

(a) Cap1 outside with patterned oxide.

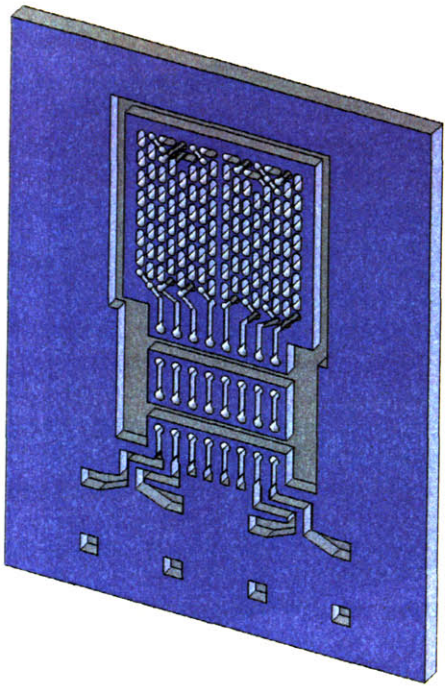

(b) Cap1 inside with tube connections and heat sinks etched.

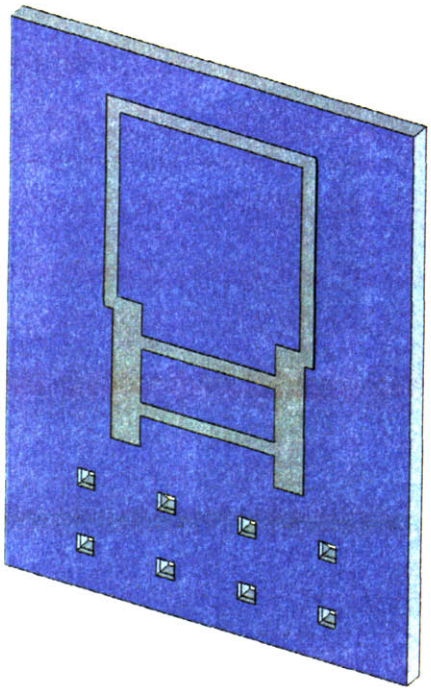

(c) Cap1 after through etch of fluidic connections from the outside.

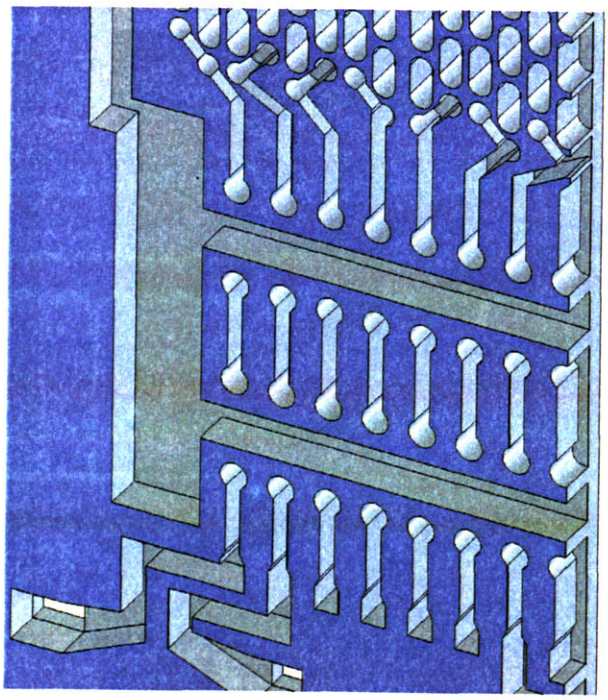

(d) Enlarged cross-section of Cap1 inside after through etch.

Figure 3-2: Cap1 fabrication steps.

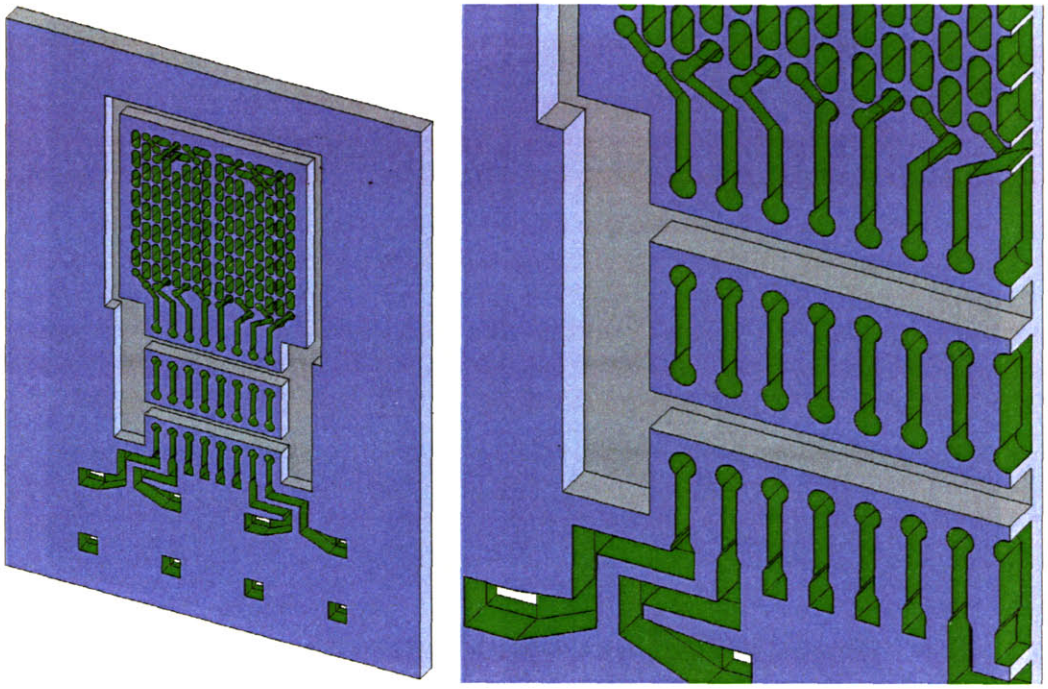

(a) Illustration of where the silicon nitride will deposit after bonding of the complete wafer stack.

(b) Enlarged cross-section of 3-3(a).

Figure 3-3: Illustration of Cap1 after nitride deposition.

The wafer is now ready for bonding. The silicon dioxide is left on the wafer because it has an important function in the final release etch. Again, Figures 3-3(a) and 3-3(b) illustrate where the silicon nitride will be deposited after bonding. One can clearly see the 250 μm thick silicon membrane that will enclose the release pits after bonding. These are the areas with no nitride present.

3.1.3 Capping wafer #2

The second capping wafer (Cap2) forms what will be referred to as the front side of the device, where the metal resistors are located. The fabrication steps are similar to those of Cap1 except for the absence of fluidic through-connections. The first step is to etch the oxide (BOE) using thin photoresist patterned with Mask *CAP2OUT*. The result is shown in Figure 3-4, and the pattern for the metal bridges next to the heat exchangers can be seen. The photoresist is then stripped and new thick resist

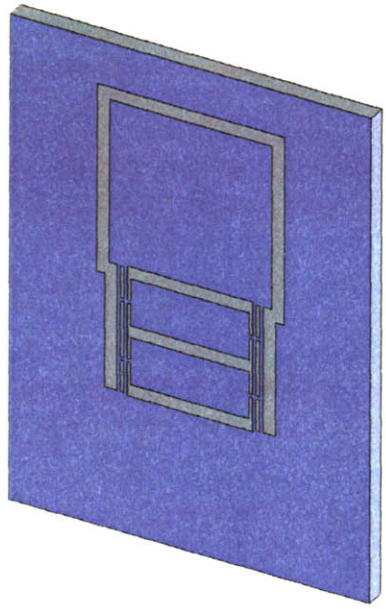

Figure 3-4: Cap2 outside with patterned oxide.

is applied on the front side and patterned using Mask *CAP2IN*. After removing the oxide with BOE, DRIE is used to again etch 400 μm into the wafer. Figures 3-5(a) and 3-5(b) show the result, and Figures 3-5(c) and 3-5(d) illustrate where the nitride will later be deposited. In all the 4 models, the stop valve constrictions for catalyst loading are seen near the bottom of the reaction chamber. The wafer is now ready for bonding.

3.1.4 Bonding and preparation for release

After a very thorough clean of the three wafers, they are bonded together with the insides of the capping wafers towards the center wafer, as illustrated in Figure 3-6. "Silicon direct" bonding with silicon dioxide on one of the two surfaces is used, followed by an hour long anneal at 1000°C to strengthen the bond. The result is shown in Figure 3-7 with a cross-section through the right-most part of the tube section and the reaction chamber.

Next silicon nitride is deposited using LPCVD (low pressure chemical vapor deposition), leaving 4 μm of nitride on the outer surfaces of the wafer, as well as everywhere

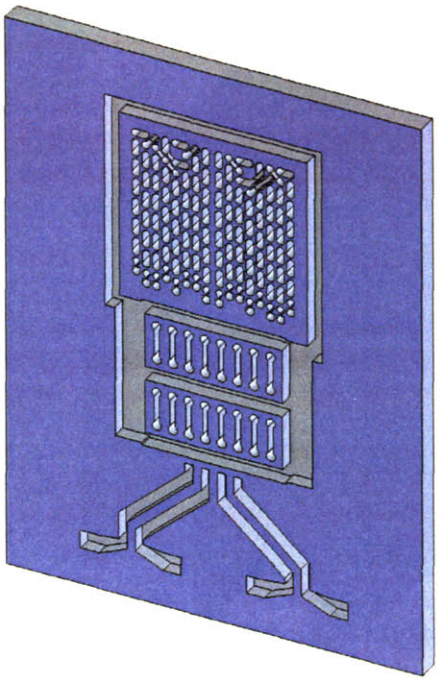

(a) Cap2 inside with tube connections and heat sinks etched.

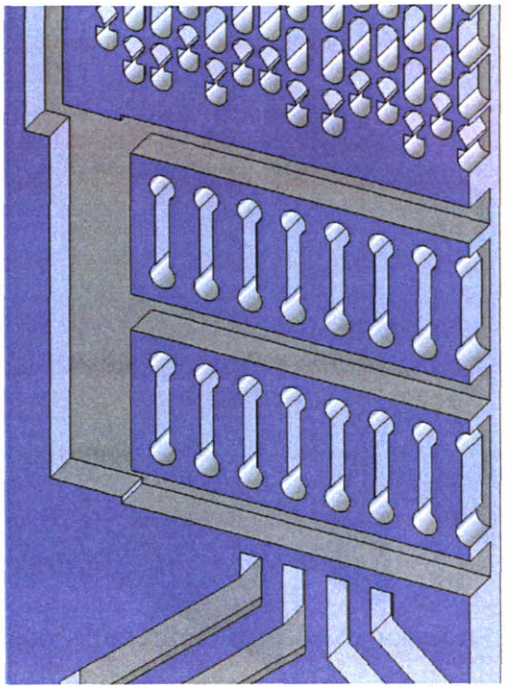

(b) Enlarged cross-section of 3-5(a).

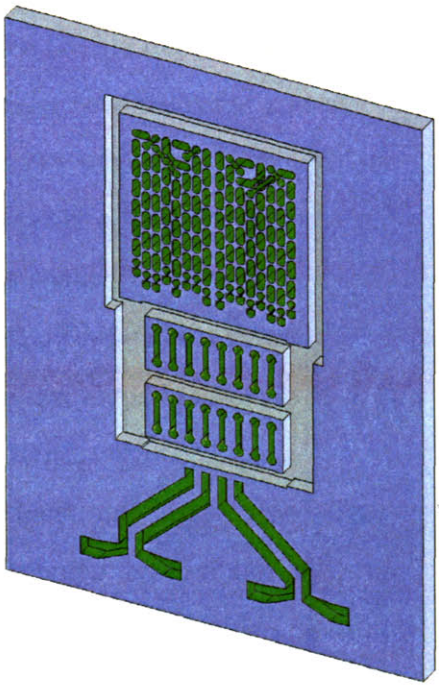

(c) Illustration of where the silicon nitride will deposit after bonding of the complete wafer stack.

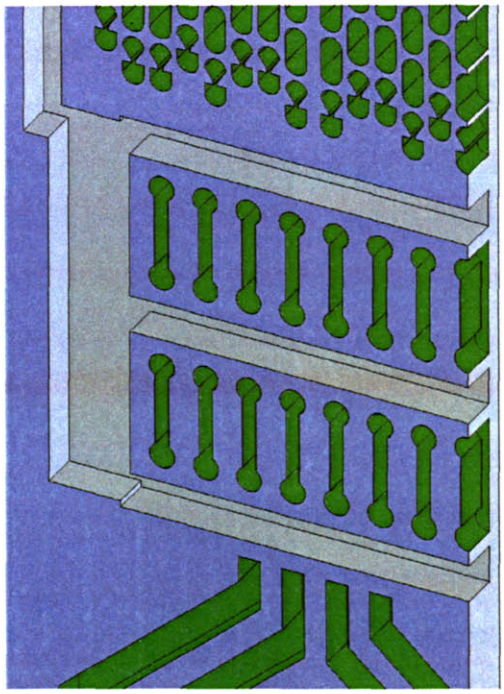

(d) Enlarged cross-section of 3-5(c).

Figure 3-5: Cap2 fabrication steps.

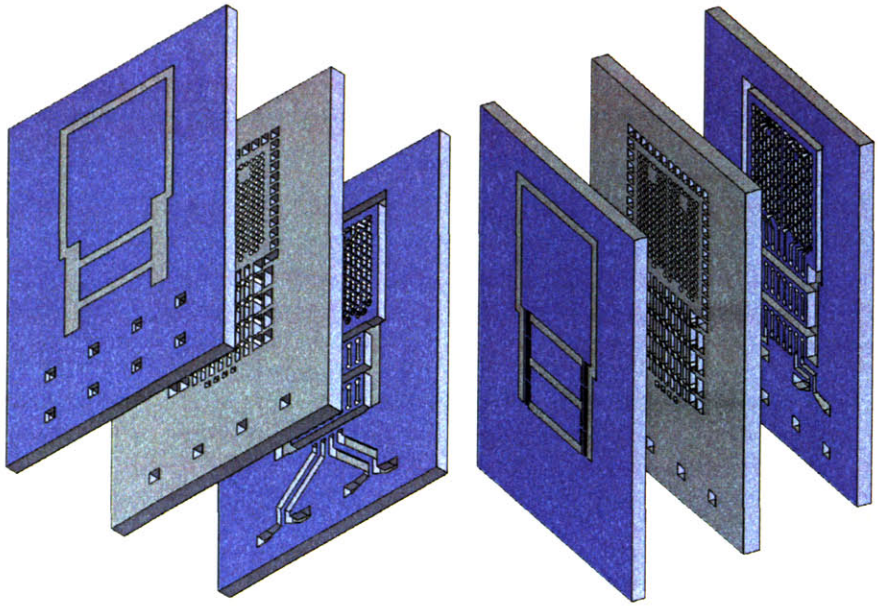

(a) Back view. (b) Front view.

Figure 3-6: Illustration of bonding orientation of the three wafers.

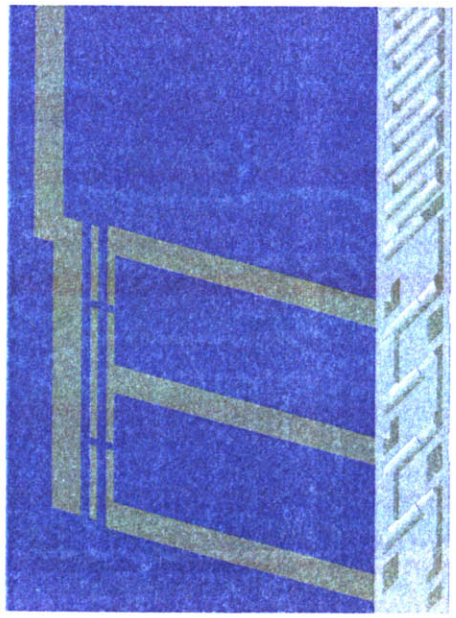

Figure 3-7: SμRE III cross section after bonding (front view).

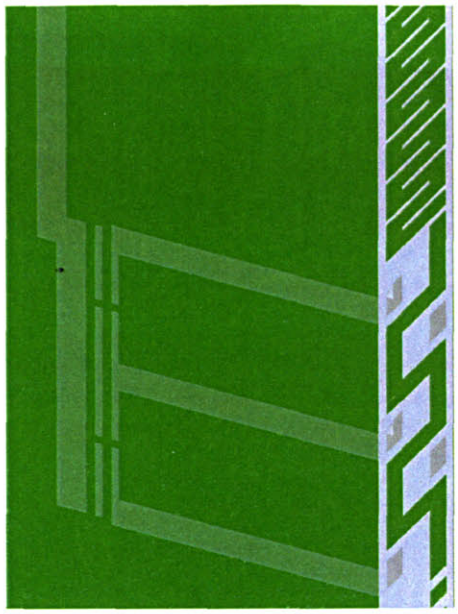

Figure 3-8: SμRE III cross section after silicon nitride deposition.

in the flow channels, entering through the fluidic connections on the back side (Cap1). The result is shown in Figure 3-8.

After nitride deposition, the metal resistors are deposited. Mask *METAL* is used with image reversal resist to leave photoresist in the areas where metal is not desired. A thin (15 nm) tantalum adhesion layer and a thick (200 nm) platinum layer are then deposited in an electron beam (e-beam) deposition system, and finally the wafer stack is soaked in acetone to remove the unwanted metal with photoresist below it. This *lift-off* procedure leaves the metal resistors, as illustrated in Figure 3-9.

The last steps before the final release are to open up the release pits. This is done using DRIE, with thick photoresist patterned with Masks *CAP1OUT* and *CAP2OUT* on the back and front respectively, the same masks that were used in the beginning of the process, to etch the oxide on Cap1 and Cap2. The oxide was etched early on because while the nitride and silicon can easily be etched in the DRIE system, the oxide is more resistant. At this stage in the process, wet etching chemistry is avoided due to the long flow channels that would get filled with liquid. The result of etching the nitride and then the silicon on each side is shown in Figure 3-10. The triple-stack is now ready for the final release.

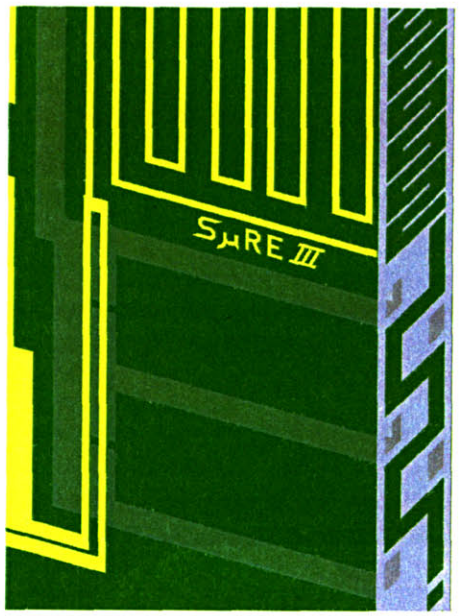

Figure 3-9: SμRE III cross section after platinum deposition.

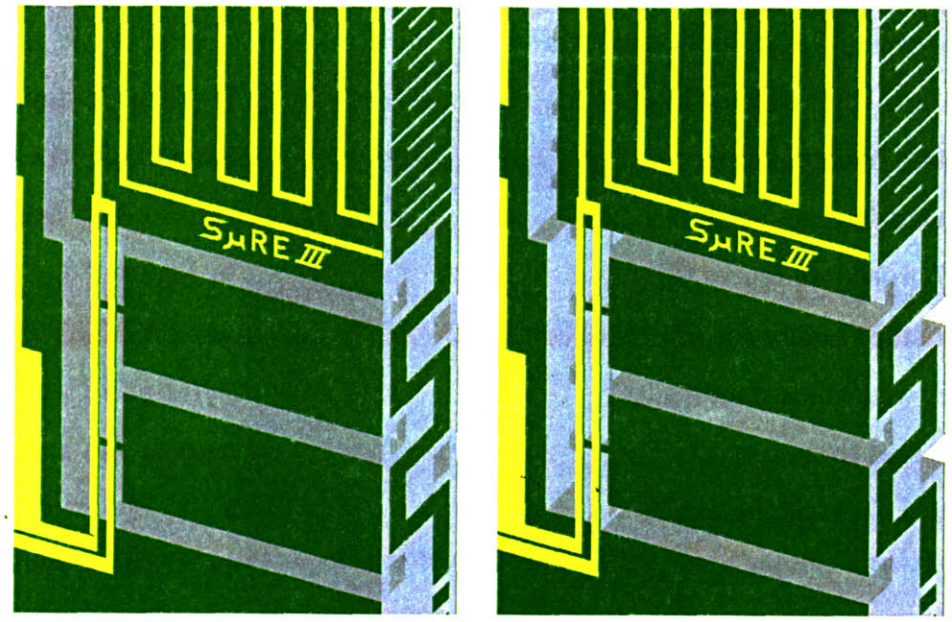

(a) After etching the nitride.

(b) After etching through the silicon.

Figure 3-10: SμRE III cross section during and after opening up the release pits.

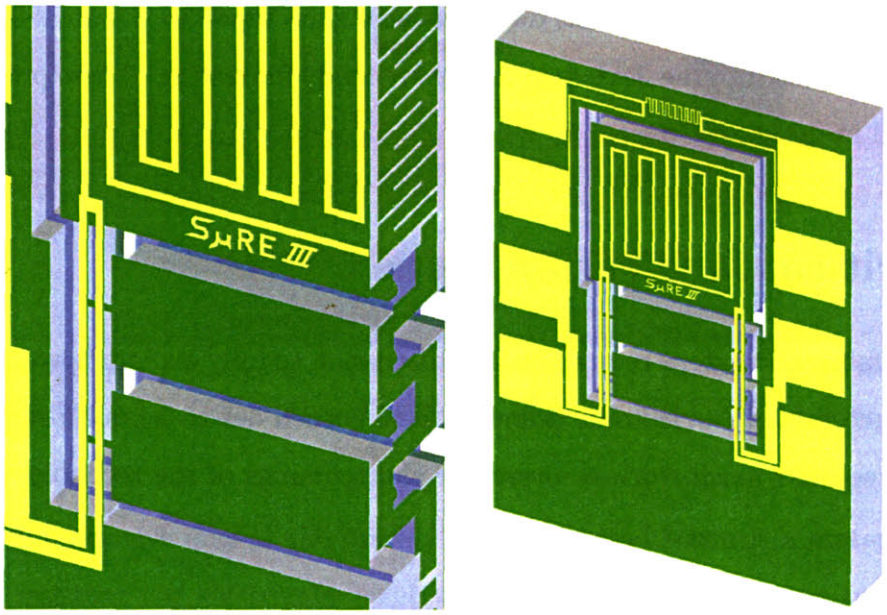

(a) After final release.

(b) Full view of completed device.

Figure 3-11: SμRE III cross section and full view after final release.

3.1.5 Final release

At this point in the process, the tubes are covered with silicon and the reaction chamber and tube section are connected to the substrate with a network of silicon walls (see Figure 3-1(a)). These are etched away in the final release. The process is designed to use an isotropic etchant, such as fluorine gas, but for reasons that will be discussed in Section 3.2.5, tetra-methyl ammonium hydroxide (TMAH), an anisotropic liquid etchant, was used instead. The center wafer pattern is designed so that by etching 115 μm in all directions, the device is completely released. TMAH etches silicon, while leaving silicon dioxide, nitride and platinum mostly untouched. This is why the nitride and oxide protecting the heat exchangers and the reaction chamber are undercut, but not attacked. The result is shown in Figure 3-11 for an *isotropic* etch.

At this point the devices are annealed for 30 minutes at 1000°C to stabilize the metal. An annealing temperature well above the highest likely temperature during operation (800-900°C) is used to avoid resistance drift. After the anneal the packaging

chips are applied to either side of the device using a glass tape (see Figure 2-9). Then the catalyst is loaded into the devices and they are ready for testing. These procedures are explained in detail in Chapter 5.

3.2 Critical fabrication steps

A few of the fabrication steps require further discussion to fully explain how they were eventually successfully carried out. Some of them turned out to be quite complex in nature and required much work to overcome shortcomings of the technology or the equipment.

3.2.1 DRIE through etch

Given the capabilities of DRIE in etching very deep and high aspect ratio features, it is perhaps somewhat surprising that etching through a wafer should be problematic. The challenge does indeed not lie in the depth or the aspect ratio, but rather in breaking cleanly through the backside of the wafer. This clean cut is necessary for the tube mold, because any deviation from the cylindrical shape of the tubes would introduce stress concentrations and weaknesses. The problem is that when the etching gases finally break through the last microns of silicon at the bottom of the wafer, the features tend to blow out on the back side, ruining the smooth and narrow bonding surfaces on the back side.

DRIE tools employ helium gas to cool the wafers in the chamber from the underside. The wafer is pressed down on a circular rubber lip seal by ceramic fingers. If the helium leaks into the chamber in sufficient quantities, the plasma is diluted too much and is no longer effective. Therefore, to break through a wafer, it must be mounted on another wafer to avoid helium leakage. (While this makes the blow-out problem worse, it would still exist without it.) Typically, fused silica wafers are used for mounting because they are very resistant to the SF_6 used to etch in the DRIE process. However, these wafers, as well as using an oxide coating on the back of the device wafer, will result in *footing*.

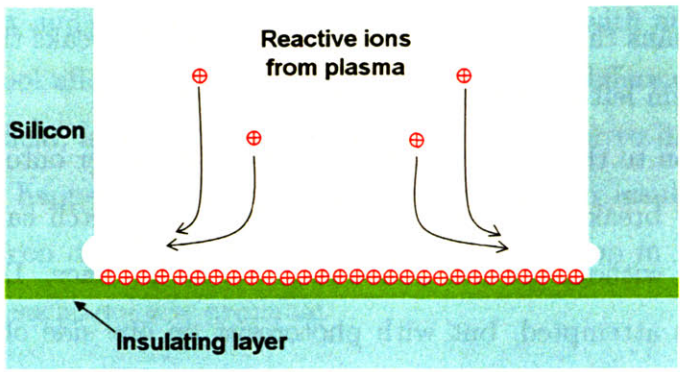

Figure 3-12: Conceptual illustration of footing in DRIE process.

When the reactive ions of the plasma are accelerated towards a material that is both etch resistant and electrically insulating, they are trapped on the surface of the material, charging it up, with no free charge to neutralize them. The charged surface then exerts a force upwards on the downwards accelerating ions, which are deflected sideways. If the charged surface is at the bottom of a deep feature in silicon, it will etch the silicon laterally, creating "feet" at the bottom. Hence the name *footing*. This is illustrated in Figure 3-12. When footing occurs at the bottom of the features in the center wafer, the bonding surfaces surrounding the tube molds on the wafer back-side are destroyed, rendering the wafer useless.

While footing is not instant upon breaking through the wafer, another non-ideality of the DRIE tools makes it necessary to keep etching after the features have been broken through: non-uniformity. As the plasma forms above the wafer, it is used to etch the surface. This leads to depletion of the reactive species in areas with a high percentage of exposed silicon. Since there is always more unreacted plasma near the wafer edges, it etches faster here, and slower towards the center. Additionally, smaller features typically etch slower than larger features. Unfortunately, trying to create conditions where both of these non-uniformities are eliminated is impossible. In a very simplified view, faster etching, more aggressive recipes tend to be quite uniform across the wafer but very non-uniform between features of different size, while slower etching recipes that tend to be more uniform between features of varying size are more non-uniform across the wafer. For SμRE III, which has a relatively large variation in

feature size, this means that when the first die on the wafer breaks through, there is still at least 40-50 μm left to etch in the center.

The final solution to the through etch is to mount the wafer onto another silicon wafer, so that after breaking through the device wafer, the etch can continue into the mounting wafer without too much distortion at the interface. Direct silicon-to-silicon bonding was attempted, but with photoresist on one side of the wafer, the back side could not be cleaned well enough to achieve a good bond. Therefore thin photoresist was applied in a few places, and the wafers contacted, yielding a very thin but thermally connecting film of resist between the two wafers. Upon break-through, this very thin resist offers minimal resistance to the etch species, leaving time for very little footing before it has been broken through. After baking, the resist is never smooth but full of bubbles. Therefore, there are many gaps between the two wafers that upon break-through allow reactive species to enter and roughen the surface underneath, making bonding impossible.

This is solved by protecting both sides of the center wafer with silicon dioxide. The oxide is then patterned, on the front side with Mask *TUBES*, and on the backside with Mask *TUBES-BACK*, the latter being a slightly widened version of the former. In *TUBES-BACK* all the features are extended by 12 μm in all directions, making them 24 μm wider. This allows for some misalignment for the front to back alignment of the photolithography and also for some blowing out at the bottom before the backside oxide is encountered and footing becomes a reality. With this method, a reasonably clean break-through is achieved, leaving a clean bonding surface.

A better alternative would be to coat the backside of the the wafer with aluminum. Aluminum does not etch in SF_6, and it is electrically conducting. Very promising results have been achieved in breaking through a wafer in this fashion [22]. But due to the limitations in the MIT fabrication facility relating to cross-contamination of equipment, the LPCVD silicon nitride deposition tube furnace does not allow wafers that have already seen metals of any kind, and this method could therefore not be used.

Another possible solution would be to leave all the silicon dioxide on the back

of the wafer intact and etch down to it using a DRIE tool with an "SOI-kit". This addition to the tool allows the plasma to be created at a different radio frequency electro-magnetic field, and the switching allows the insulator to discharge, avoiding any footing from happening. SOI refers to SOI (silicon on insulator) wafers that have a buried silicon dioxide layer often used as an etch stop in MEMS processes. Unfortunately no such tool was available.

3.2.2 Wafer bonding

The bonding of the three wafers is a relatively standard process. The key to successful silicon-direct bonding is smooth and clean surfaces. In each of the two bonding steps, one surface is silicon while the other is covered with silicon dioxide. This is essentially the same as bonding two silicon surfaces, because there is a native oxide present. The wafers must be very smooth and to assure that they are entirely particle free, they go through a series of cleans: oxygen plasma ash, piranha clean (sulfuric acid:hydrogen peroxide 3:1), concentrated hydrofluoric acid clean (49%) and RCA clean (ammonium hydroxide:hydrogen peroxide:water 1:1:6 followed by hydrochloric acid:hydrogen peroxide:water 7:1:1, both at 80°C). The wafers are bonded immediately following the cleans to avoid particles depositing on their surfaces. Even a single particle in the wrong place can inhibit the bond in that area and destroy a device.

The bonding is carried out in two steps. First Cap2 is bonded to the center wafer. Then this two-wafer stack is bonded to Cap1. The second step is carried out in vacuum to ensure that there is no air in the resulting enclosed cavities. The wafers are then pressed overnight to make sure all of the narrow bonding surfaces contact well. In the following 1000°C anneal, any trapped air in the cavities will expand, potentially leading to the bond being pried apart. The vacuum bonding ensures that this does not happen.

3.2.3 LPCVD silicon nitride growth

LPCVD deposition of silicon nitride was chosen for its ability to deposit uniformly, even inside the long channels winding through the wafer. But for such long channels, the gases are depleted before moving all the way into the reaction chamber. As a result the nitride thickness decreases the farther into the tube section one moves. The original target wall thickness for the tubes was 2 μm. However, early tests showed that with this thickness on the wafer surface, the innermost tubes only had a thickness of about half of that and were too fragile. It was therefore decided to increase the thickness on the wafer surface to at least 4 μm, to ensure that all the tubes were at least 2 μm thick.

LPCVD is a relatively slow deposition method, and growing 4 μm takes almost 24 hours. Other, faster methods, such as PECVD (plasma enhanced chemical vapor deposition) cannot be used, however, because the deposition does not reach far inside the flow channels. It is also crucial that the nitride is low stress (silicon rich), and not stoichiometric, since the latter would be stressed compared to the silicon and crack for such a thick layer.

3.2.4 Metal deposition

Surprisingly the metal turned out to be one of the most problematic parts of the fabrication process. SμRE I had resistors made of an e-beam deposited sandwich structure of Ta-Pt-Ta at thicknesses 10nm-400nm-30nm from bottom to top. The bottom Ta is an adhesion layer while the top Ta layer helps improve the high temperature lifetime of the Pt. Platinum has a tendency to agglomerate at higher temperatures [9], cutting the electrical contact. This occurs above about 800°C, with increasing speed as the temperature rises. Unfortunately the top Ta layer only increases the lifetime of the Pt somewhat and the structure is not operable at 1000°C.

Other metal structures were attempted, including pure tantalum. While pure Ta can survive well at very high temperatures in vacuum, most of the SμRE testing is done in air, and Ta oxidizes quickly at such high temperatures. Additionally, the only

tool available in the MIT fabrication facility for depositing Ta is the e-beam. This tool does not provide a sufficiently good vacuum, and as a result the Ta film deposited contains about 18% oxygen (measured by XPS:x-ray photoelectron spectroscopy) and is not electrically conductive enough to be used. Other refractive metals, such as Tungsten, undergo catastrophic oxidation at such high temperatures, meaning that the oxide that forms is a gas, and the metal quickly disintegrates.

It was therefore finally decided to revert back to the metal sandwich structure of SμRE I, but due to a yet unsolved problem, the Pt thickness had to be reduced to below 200nm, and the top Ta layer was skipped. Thicker layers would cause the metal to peel off the wafer during the deposition, sometimes with photoresist so that metal was deposited where not desired, and sometimes everywhere on the wafer. The problem was clearly a build-up of stress in the Pt that would consequently peel off despite a good adhesion layer. The exact cause of the problem is not yet known.

3.2.5 Final release etch

SμRE III was designed for an isotropic final release. SμRE I was released using fluorine gas at 25% in nitrogen at room temperature and atmospheric pressure. This was the first choice for SμRE III as well, but the narrow trenches between the heat exchangers did not allow the gas to diffuse in quickly enough, leading to depletion of the reactive species before getting into the release pits around the tubes. The result was over-etching in some places and under-etching in others. Xenon difluoride (XeF_2) was also attempted, with less success. Not only was the same problem made worse, but the silicon nitride was also etching too quickly.

The next attempt was with potassium hydroxide (KOH), an anisotropic etchant of silicon. It is very selective to nitride and somewhat to oxide. While KOH does not have a problem with depleted etch species, giving a uniform etch across the device, peculiar shapes result because of the different etch rates of the various etch planes of single crystalline silicon. In particular, this effect created wedges of silicon along the nitride tubes (see Figure 3-13(b)), serving as a thermal shunt and essentially rendering them useless for thermal isolation. Leaving the devices in the etching bath

long enough to remove these wedges results in over-etching of other areas.

The final solution was to use TMAH instead of KOH. Even though it is also an anisotropic etchant of silicon, with similar characteristics to KOH, it is only about half as selective to the slower etching planes. The devices are therefore released successfully. Figure 3-13 shows pictures comparing the various methods attempted.

3.2.6 DRIE halo etch

Although not shown Section 3.1, as is evident from Masks *CAP1IN, CAP2IN, CAP1OUT* and *CAP2OUT*, the trench separating the reaction chamber and the tube section from the substrate, is not etched out directly in its entirety. Because this would expose large amounts of silicon to the DRIE etch, potentially causing more non-uniformity and black silicon (silicon grass making the surface appear black), a *halo* pattern was used. Rather than exposing the whole feature, only a thin line (in this case 100 μm wide) around the feature is exposed. Once the etch is complete, the feature then falls out. The feature to be removed at the end must not be bonded to the center wafer. This is avoided by using Mask *OXHALO* to etch about 7 μm into the inside of the two capping wafers, after removing the oxide in that feature. While ensuring that this surface does not bond to the center wafer, it is also shallow enough that thick resist can readily be applied to the surface without any problems with streaking in the photoresist spinner. This is done near the beginning of the process.

3.2.7 Dry photoresist

After depositing metal on the triple wafer stack, the final DRIE etches open up the release pits for the final release. However, at this point, there are holes leading into the fluidic channels on one side of the wafer, making it difficult to spin photoresist there. The resist becomes very non-uniform and developer enters the holes, consequently coming out during drying and post bake to mar the features. To avoid this problem, a dry resist produced by Dupont, MX5030®, was used instead. It is in the form of a tape, with protective films on both sides. One film is removed, the tape is applied

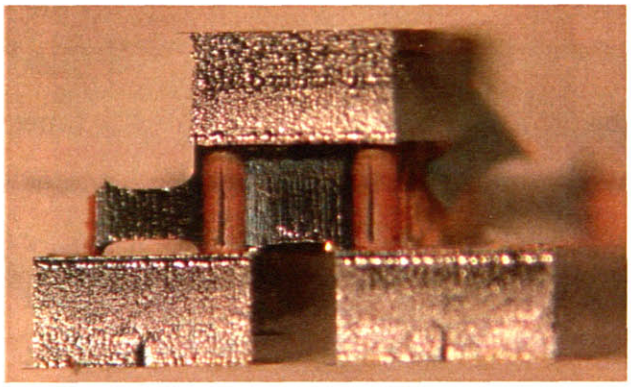

(a) Part of tube section after fluorine release. The isotropic etch gives straight side walls. Tubes are not fully released.

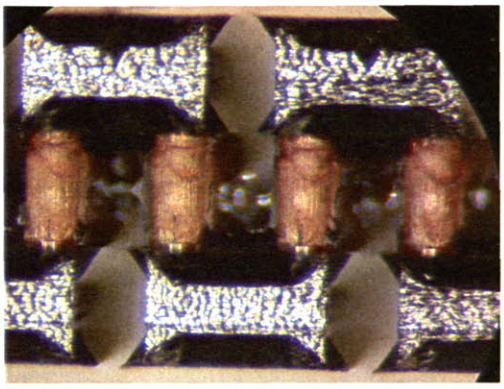

(b) Part of the tube section after KOH release. The slower etching crystal planes are apparent, as well as the silicon thermal shunts on each side of every nitride tube.

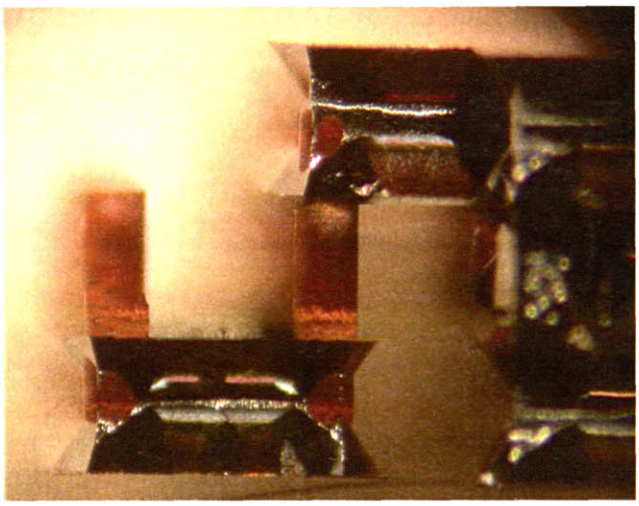

(c) Part of the tube section after TMAH release. Similar to KOH, but with tubes completely released.

Figure 3-13: Various SμRE III final release methods.

to the wafer. After exposure, the tape is removed for developing. The wafer is baked between all the steps, to promote adhesion and straight side walls. This 30 μm thick resist clearly has no problems with streaks since it is not spun, and the holes are covered by the photoresist until after developing. The holes being 500x500 μm are too wide for the resist to span across, and it breaks at the following bake. The holes are therefore covered with Dupont Capton® tape during the DRIE etch. The tape resist is also used on the other side of the wafer because both sides are patterned at the same time, and developing with different developers does not work.

The MX5030® is a negative photoresist, which is why Masks *CAP1OUT* and *CAP2OUT* exist in two versions, the positive masks for the positive photoresist at the beginning of the fabrication process, and the inverse masks for the negative tape resist at the end. The pattern achieved on the wafer is the same. The appropriate developer for the MX5030® is a solution containing potassium carbonate as the active ingredient. For contamination reasons this developer was not allowed in the fabrication facility. Instead, a mixture of AZ917® and water (1:1) was successfully used to develop the resist. The tape resist was removed by acetone soaking and oxygen plasma ashing.

3.3 Fabricated devices

Figure 3-14 shows the front and back of a SμRE III device, completely released with TMAH. From this angle, the anisotropic artifacts are only seen by the overetched corners of the reaction chamber and the heat exchangers. On the back side some dried up chemical residue is seen on the surface. Cleaning this off is tricky because touching the suspended structure easily breaks it. The apparent roughness of the platinum resistor stems from the thin metal film being deposited on a thick and somewhat rough silicon nitride layer, not from the etching. The 8 dark stripes seen in each of the trenches between the heat exchangers are the silicon nitride membranes covering the heat exchanger channels, but with a "roof top" of silicon left on top of it. This is another etch artifact.

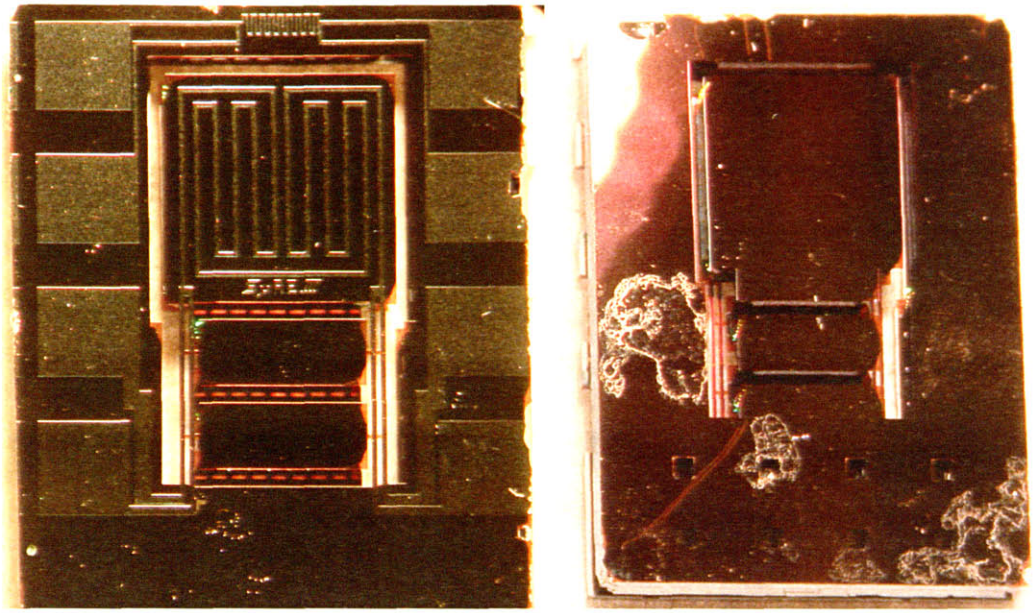

(a) Front side view with platinum resistive heater.

(b) Back side view with fluidic inlets/outlets.

Figure 3-14: SμRE III device completely released with TMAH.

Unfortunately, because of the geometry of the device, the tubes cannot be properly inspected without first breaking the SμRE III. Figure 3-15(a) shows a broken off reaction chamber with part of the tube section still attached. A close-up of the tubes is shown in Figure 3-15(b). The TMAH etch artifacts are very clear from these pictures. They do not cause any trouble for the device. Even the partially exposed nitride from the inside of the heat exchangers probably do not weaken the device, because the silicon at the tube-heat exchanger interface is still intact. This interface, however, is clearly the structurally weak link in the device, since most of the tubes broke off exactly there. This is discussed further in Chapter 6. A side view of the tube section is shown in Figure 3-13(c).

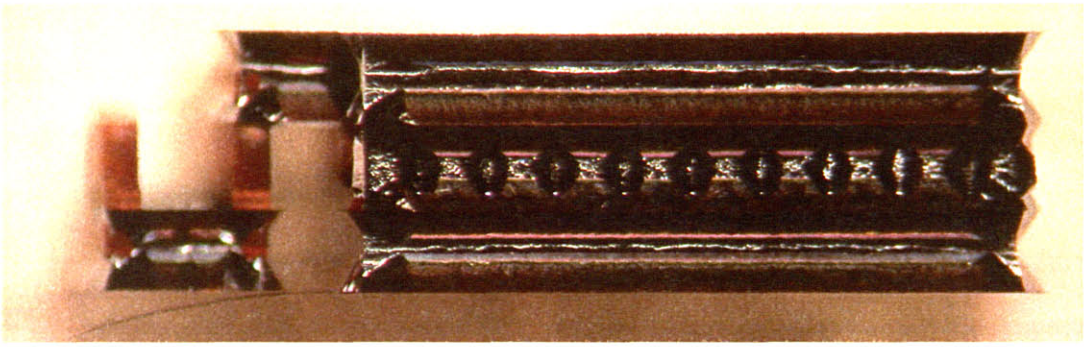

(a) Released reaction chamber seen from the side, with anisotropic etch artifacts.

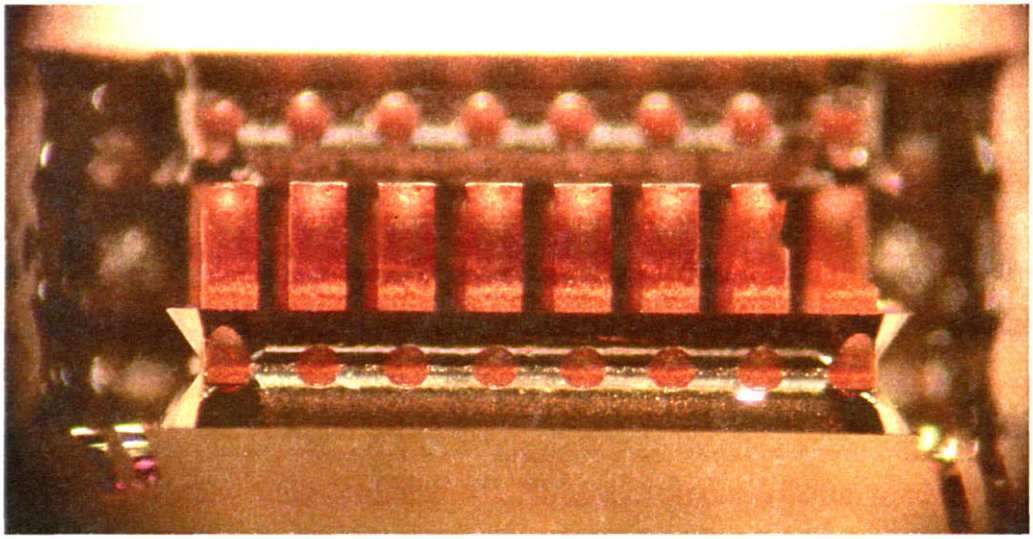

(b) 8 parallel silicon nitride tubes with reaction chamber in the background.

Figure 3-15: Views of reaction chamber and tubes from broken TMAH-released device.

3.4 Fabrication evolution from previous SμRE generations

SμRE I and II were both based on the same fabrication principles. The general idea of a tube mold was the same as for SμRE III, but the tubes were of rectangular cross-section, etched in the plane of the wafer. This was achieved by etching the channels almost through the wafer, but leaving about 50 μm of silicon at the bottom. A second, ultrathin wafer 50 μm thick was then bonded to the top, creating a complete tube mold. The final release of the device was dependent on this thickness being close to the target number. This process had several problems associated with it. The first was related to the non-uniformities of the DRIE etch tools, discussed in Section 3.2.1. Etching deeply into the wafer and leaving 50 μm of silicon at the bottom is literally impossible in a regular DSP wafer, because the difference in etch depth across the wafer at best is close to that number.

Figure 3-16(a) shows an SEM (scanning electron microscope) image of a SμRE II cross section etched with a recipe made for good uniformity across the entire wafer. Clearly the uniformity between features of different size is very bad. On the other hand, Figure 3-16(b) shows a plot of the etch depth across the wafer for a recipe that is locally uniform between features of different size. Neither case is satisfactory. Another solution was therefore sought: SOI (silicon on insulator) wafers.

SOI wafers consist of a thick silicon wafer with a thin film of oxide on it, and another layer of silicon on top of the oxide. This top silicon layer is called the device layer and can be just about any thickness one might desire. The handle layer is typically regular wafer thickness for robustness. For the earlier SμRE processes, SOI wafers with 50 μm device layers were used, etching the channels from the back side, to ensure that the DRIE would stop on the insulating oxide and leave exactly 50 μm of silicon. But unfortunately, by the time the buried oxide had been reached in all the features across the wafer, the footing effect had undercut the fastest etching features, making walls and posts detach from the wafer, essentially destroying the devices. Figure 3-17 shows mild and severe footing on the buried oxide layer in SμRE

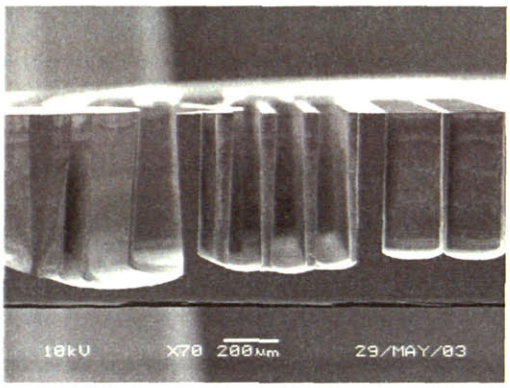

(a) Local non-uniformity between features of different size, within one die.

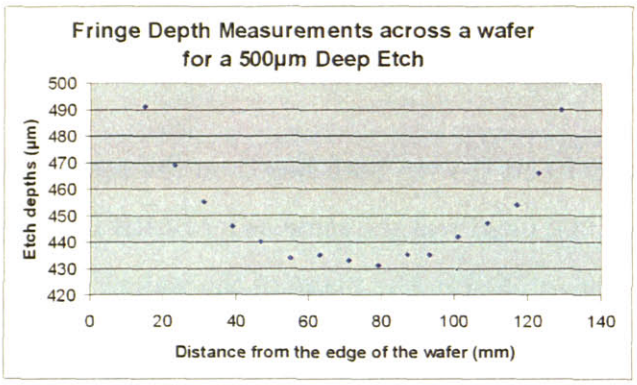

(b) Plot of global non-uniformity across a wafer.

Figure 3-16: Non-uniformities in DRIE.

II. Different methods were attempted to overcome this problem, including covering up devices that were done and then continuing the etch. SμRE I, which was built on 4-inch wafers, was marginally successful due to the small area and the thinner wafers. SμRE II, however, was built on 6-inch wafers, due to a change in laboratory policy, and the footing problem became insurmountable. This was the main reason that SμRE II was abandoned.

The second problem was related to the ultrathin wafers. Not only are 50 μm thick, 6-inch diameter wafers difficult to work with (they can be bent 180°, touching the opposing edges without breaking). They are also difficult to manufacture, especially when they have to be smooth enough for silicon direct bonding, and no reliable source of good ultrathin wafers was found. An alternative would be to use full thickness DSP wafers and then grinding, polishing or etching it down to the appropriate thickness after bonding.

The final main problem that was SμRE III aimed to eliminate, was the poor burst resistance of the rectangular tubes. In particular due to the footing, one set of corners of the tube cross-section was very non-ideally shaped. This is probably the main reason why the burst pressure of the tubes was only about 2 atmospheres. The circular tubes of SμRE III are designed to be much more resistant to bursting.

In conclusion, the radically different design of SμRE III manages to eliminate

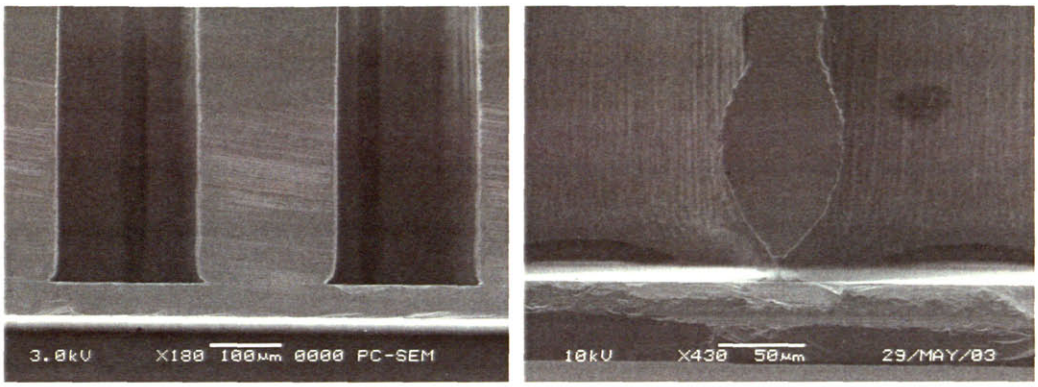

(a) Mild footing on buried oxide layer.

(b) Severe footing on buried oxide layer, with complete undercut connecting two adjacent channels.

Figure 3-17: Cross-sections showing footing on buried oxide layer in SμRE II.

the SOI and DSP wafers (which are both very expensive and less readily available compared to DSP wafers). It also addresses the problem of burst pressure, along with several other improvements discussed in previous sections and chapters. However, the improvements come at a price. SμRE III has 2 bonding steps with alignment, while the earlier generations had 1 bonding step without alignment. The process otherwise has many more steps too, some of them introducing challenges as discussed in Section 3.2. It is therefore a trade-off between improvements and new complications.

Chapter 4

Modeling

The modeling of SμRE III is almost entirely concerned with its thermal and optical characteristics. This is because the device is mechanically passive, and the only really important aspect of the mechanical structure is that it is sturdy enough for testing and normal handling. This amounts to the silicon nitride tubes supporting the weight of the reaction chamber for accelerations and supporting internal pressures high enough for the needed gas flows, with vacuum outside. Leonel Arana in his Ph.D. work [1] modeled the burst pressure for various shapes but found the real values to be very far below the theoretical ones. The usefulness of this calculation is therefore questionable and experimental results will be used.

Modeling the thermal and optical behavior of the TPV micro-generator is done in two steps: (1) calculating the heat losses through all the different pathways of the reactor at various temperatures, and (2) incorporating experimental black body measurements of the photocell responses and modeling of partially illuminated photocell areas. Section 4.1 describes the modeled structure, including geometric and physical assumptions. A discussion of the various thermal pathways and their individual mathematical models with justifications are given in Section 4.2. The complete model and simulation results are given in Section 4.3, while the the photocells are described in Section 4.4.

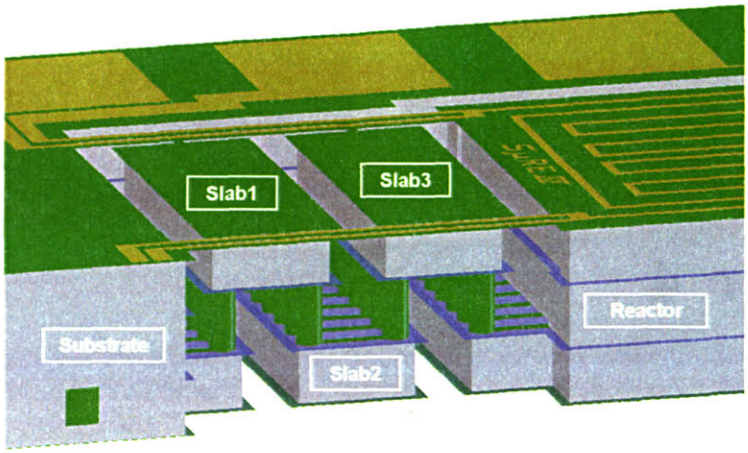

Figure 4-1: Annotated model of SμRE III detailing the five thermal components considered for the modeling. The ambient surrounds the device.

4.1 Modeled structure

An annotated side view of SμRE III is shown in Figure 4-1. The structure is modeled by simplifying it to 5 discrete thermal units: the reactor, the 3 heat exchangers, and the substrate surrounding the reactor with the ambient surroundings. Each thermal unit is treated as isothermal. Heat flow is considered only between these discreet units. The heat loss paths are the following:

- Solid conduction through the platinum resistor bridges
- Solid conduction through the silicon nitride tubes
- Forced fuel and exhaust gas convection inside the tubes
- Radiation
- Air conduction and natural convection

The most significant simplification of the model is the assumption that each of the five thermal components is isothermal. This assumption can be made because of the high thermal conductivity of single crystalline silicon. The substrate is, relative to the dimensions of the tubes, a massive and thick piece of silicon. Hence thermal gradients of any significance will not develop in it. Even if the temperature near

where the tubes connect and the opposite side are of slightly different temperature, the only significant heat exchange between the reactor and the opposite side will be through radiation, and a few degrees difference on the cold side will not make much difference to that calculation.

The reaction chamber is in a similar way to the substrate a massive box of silicon. The flow channels inside only occupy 8.6% of the total volume of the box and can therefore be largely ignored in terms of the heat conduction. Results from SμRE I showed that hot spots had a tendency to form near where the fuel first encounters the catalyst, but in SμRE I, the inside channels of the chamber occupied about than 22.5% of the box volume (depending on the reaction chamber inner geometry) with only a thin layer of silicon on the top and bottom, leaving much less silicon to distribute the heat evenly and quickly. Furthermore, at a given average temperature of the reactor, even if there are some differences in temperature across the surface, they would have to be large to significantly change the total radiated power. In the case of air conduction and natural convection, it would not make a difference since it is generally treated as linear with temperature, averaging out to the same. For these reasons. the reaction chamber will be treated as isothermal.

The heat distribution of each heat exchanger was shown to be essentially isothermal by Alexander Mitsos, in collaboration with Michael Hencke, in his Ph.D. thesis [17]. A fully three dimensional (though with square cross section tubes) model of a heat exchanger with gases flowing in and out of it was simulated in Femlab®. As shown in Figure 4-2, the silicon part of the heat exchanger is isothermal, and this assumption will be made in the overall model of the system. What the simulation also reveals is that the exiting gas in both direction has time to attain the temperature of the silicon before exiting the heat exchanger. This result will be important in the calculations for the forced gas convection.

Another way to show this, is to compare the quotient of the thermal conductivity over the characteristic length of the tubes and the heat exchangers. For the tubes, $k_{SiN_x} = 3.2\ W/mK$ and the length is about 700 μm, while for the heat exchangers, $k_{Si} = 150\ W/mK$ and the length is the longest distance between an inlet stream

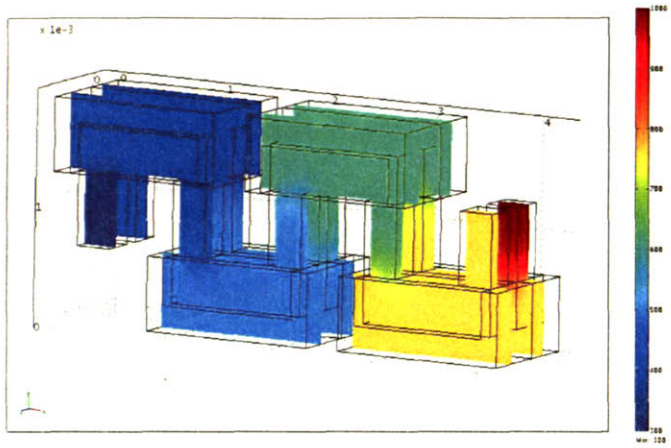

Figure 4-2: Femlab® model of tubes and heat exchangers with 3D counter-current flow [17]. Inlet velocity: 1 m/s. 2 of 8 parallel tubes shown, with flow in opposite directions in adjacent tubes.

and an exhaust stream, which is 900 μm from center to center of the channels. We therefore have

$$4.57 * 10^3 = \frac{k_{SiN_x}}{l_{tube}} \ll \frac{k_{Si}}{l_{char}} = 1.67 * 10^5 \tag{4.1}$$

confirming to some extent the model results.

For the simplicity of the calculation, the peculiar shapes created by the anisotropic release etch are ignored, and the structure is assumed to be released by an isotropic etch, as shown in Figure 4-1. This is unlikely to change the results significantly, since the surface areas are approximately the same. Heat exchange between the Substrate and the Ambient is not taken into account because the Substrate is thermally grounded. Further assumptions will be explained in the discussions of various heat flow paths in the next section.

4.2 Thermal pathways of SμRE III

4.2.1 Platinum/nitride bridges: solid conduction

The platinum on silicon nitride bridges next to the heat exchangers represent the mathematically simplest heat flow problem of SμRE III. It also turns out to be the

least significant one. The bridges are treated as a simple solid conduction problem between the the Reactor and Slab1, Slab1 and Slab3, and Slab3 and the Substrate (see Figure 4-1). At each attachment point the metal is assumed to take on the temperature of that particular thermal component. The governing heat flow equation is Equation 2.1, with a two layer structure the thermal resistance becomes

$$R_{therm} = \frac{L_{bridge}}{k_{Pt}A_{Pt} + k_{Si_3N_x}A_{Si_3N_x}} \tag{4.2}$$

where Si_3N_x is the silicon rich silicon nitride. The x is used because the exact proportions may vary. Heat flow from a component i to another component j connected by the bridge is then

$$Q^{bc}_{i\to j} = \frac{T_i - T_j}{R_{therm}} = \frac{(T_i - T_j)(k_{Pt}A_{Pt} + k_{Si_3N_x}A_{Si_3N_x})}{L_{bridge}} \tag{4.3}$$

where T is the temperature of a component. There are 4 bridges, so the cross sectional area is the area of one bridge, multiplied by 4. The heat flow, Q, is in Watts. The bridges are not considered thermal components in themselves because they have a very small surface area compared to the rest of the structure and radiation and other losses to the ambient are therefore very small.

4.2.2 Nitride tubes: solid conduction and forced convection

Heat flow through the tubes is a two-fold problem. On the one hand, solid conduction through the tube walls is nominally linear with the temperature difference between the two thermal components they connect. On the other hand, the forced convection of the gas going through the tube cannot necessarily be treated entirely separately, because there is also heat flow between the gas and the tube wall. Finally there is ambient air conduction and natural convection and radiation on the outside of the tubes. To reduce the complexity of these codependent phenomena, the following assumptions were made:

1. Heat transfer from the gas to the tube wall has a negligible contribution to the

overall solid conduction.

2. Heat transfer in the gas can be approximated as purely forced convection.

3. The tubes have near zero emissivity, and radiation can therefore be neglected.

Equation 4.4 giving the solid conduction in the tubes resulting directly from the temperature difference between two thermal units i and j is therefore similar to Equation 4.3.

$$Q^{tc}_{i\rightarrow j} = \frac{(T_i - T_j)(k_{Si_3N_x} A_{wall})}{L_{tube}} \tag{4.4}$$

where A_{wall} is the cross-sectional area of the tube *wall* of one tube multiplied by 8 to account for the 8 parallel tubes.

The heat transfered by the gases inside the tubes from a component i to another component j connected by this set of tubes can therefore be simplified mathematically to

$$Q^{fc}_{i\rightarrow j} = \dot{m}_0 c_p (T_i - T_j) \tag{4.5}$$

where $\dot{m}_0$ is the mass flow rate in kg/s and c_p is the heat capacity of the gas in J/kgK. Equation 4.5 can be rewritten as follows:

$$Q^{fc}_{i\rightarrow j} = f_{air} \frac{Q_0}{\Psi_{C_3H_8}} c_p (T_i - T_j) \tag{4.6}$$

where Q_0 is the power, in Watts, added to the Reactor by the combustion of the fuel, propane, $\Psi_{C_3H_8}$ is the specific energy of propane based on the lower heating value (see Table 1.1), and f_{air} is a multiplication factor accounting for the air in the fuel air mixture. Without it, only the mass flow rate of propane would be accounted for. It is assumed that all the propane is completely converted. Since a very large proportion of the gas mixture is nitrogen, the heat capacity for nitrogen is used for simplicity.

Silicon nitride is an electrical insulator with a very large bandgap. It is therefore transparent far into the infrared, which means that it is practically non absorbent and has a negligible emissivity. While this is not entirely true at high temperatures, the surrounding bodies are relatively close in temperature (because the tubes are in

a small area enclosed by the heat exchangers, the reactor and the substrate) and there will be little net heat exchange with a limited emissivity. Gases have negligible absorptance in the wavelengths of interest and therefore can be neglected interior and exterior to the tubes. This justifies Assumption (3).

4.2.3 Radiation

Two assumptions are made about radiation between the five thermal components. The first is that radiation is unperturbed by the tubes and the flow channels where the tubes connect. The transparency of the tubes has already been discussed in the previous section. Neglecting the geometric perturbation of the connection channels in the heat exchangers means that they are assumed to have 6 flat surfaces. As explained in Section 4.1, the geometrical perturbations caused by the anisotropic etch are also ignored.

The second assumption is that the emissivity all the elements is 0.7. The emissivity of silicon at low temperatures is lower than this due to the bandgap, but as the temperature increases, the bandgap fills because of increased amounts of free (thermalized) carriers, as shown in Figure 4-3. The bandgap is completely filled around 740°C but is already very reduced at the temperatures where the radiation becomes of any importance. 0.7 is the limit because the reflectivity is 0.3. Furthermore, the silicon is mostly covered with silicon nitride and silicon dioxide. Theses are considered transparent and therefore do not change the emissivity. The etched sides of the released structure are quite rough. However, the roughness is on order of tens of microns, and does therefore not influence the emissivity much at the wavelengths of interest (shorter than about 3 μm). The platinum resistor certainly has a much lower emissivity than the silicon, but it covers a very small surface area, and is therefore neglected. Finally, this emissivity was experimentally confirmed for SμRE I [1].

To model the radiation it is necessary to include not only the radiation to the ambient, but also between the various thermal components. To calculate this complex exchange and reflection of radiative energy, the *Poljak net radiation method* [26] is used. All surfaces are assumed grey and diffuse, and the net power radiated from a

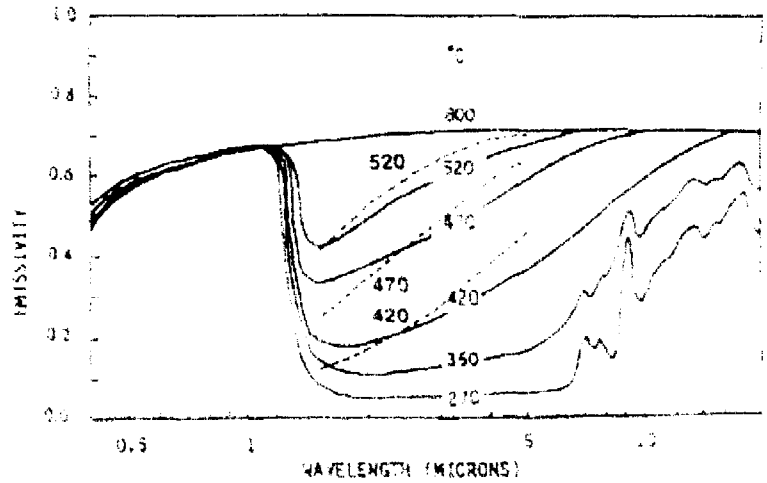

Figure 4-3: Silicon emissivity as a function of temperature [27]. The bandgap is filled as the number of thermalized carriers increases with temperature. (Dotted lines refer to certain mathematical models while solid lines are measured data.)

component k per unit area, q_k, can be expressed in two ways, as given in Equations 4.7 and 4.8.

$$q_k = \frac{\epsilon_k}{1-\epsilon_k}(\sigma T_k^4 - q_{o,k}) \tag{4.7}$$

$$q_k = q_{o,k} - \sum_{j=1}^{N} F_{k\to j} q_{o,j} \tag{4.8}$$

where $q_{o,k}$ is the power radiated from component k (*not* the *net* power), ϵ_k is the emissivity of component k (which in the case of the SμRE can is the same for each component and can therefore be replaced by just ϵ), $T-k$ is the temperature, σ is the Stefan-Boltzmann constant ($5.670 * 10^{-8}$ Wm^{-2}K-4), and $F_{k\to j}$ is the viewfactor from component j to k. The equations can be rewritten as follows:

$$\sigma T_k^4 = \frac{1-\epsilon}{\epsilon} q_k + q_{o,k} \tag{4.9}$$

$$0 = q_k - q_{o,k} + \sum_{j=1}^{N} F_{k\to j} q_{o,j} \tag{4.10}$$

and can then be solved since it is a set of $2N$ equations of $2N$ unknowns, the q_k and the $q_{o,k}$, the latter of which are of no interest to this modeling. It is important to

remember that q_k is per unit area, and the areas must therefore be included in the calculations.

4.2.4 Ambient: gas conduction and natural convection

There are two cases to consider for this heat flow path. First, the simplest one is for a vacuum packaged device. In this case, gas conduction and natural convection on the outside of the device is eliminated and need not be taken into account. If operated in air, however, this is an important heat loss mechanism. Typically heat losses to the air are modeled as a linear function of temperature, as in Equation 4.11.

$$Q_{i \rightarrow Amb} = hA_i(T_i - T_{Amb}) \tag{4.11}$$

where h is the heat transfer coefficient in W/m^2K and A_i is the surface area interacting with the ambient. While this accounts for the losses to the air, conduction through the air to neighboring components (such as between the Reactor and the Substrate), has a different heat transfer coefficient. While guesses could be made for the values of h, they must eventually be obtained from experimental data. Furthermore, the thermal characterization of both SμRE I and III shows that these heat loss mechanisms are not entirely linear. With all of this in mind, the usefulness of a model to describe this heat loss path becomes questionable, and experimental data will be used directly instead. Since the other heat flow paths can be modeled independent of this one, the model will only be made for the case of vacuum.

4.3 SμRE III thermal model results

The Matlab® code for the simulations is given in Appendix C. The equations described above are used for the calculations in matrix form. Convergence is obtained by fixing the temperature of the Reactor and the Substrate, and giving a thermal capacitance to each of the slabs to simulated a timed response to an initial guess of slab temperatures. The initial guess is a linear temperature distribution, which is

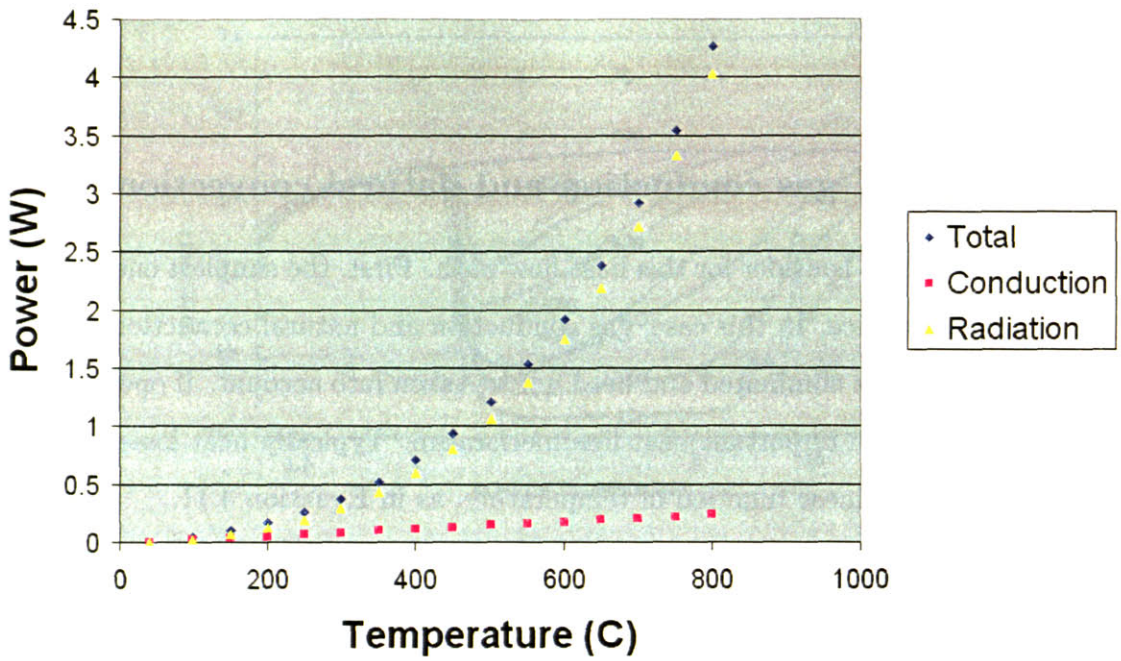

Figure 4-4: Reactor heat losses as a function of temperature in vacuum with no gas flow. Total, conductive and radiative heat losses plotted.

corrected until the net flow of energy out of each slab is close to zero. Each run takes only a few seconds to converge.

Two scenarios are modeled. The first is for electrical testing reactor in vacuum. In this scenario, the only heat loss paths are solid conduction and radiation. The results are shown in Figure 4-4. The total heat losses along with the individual components are plotted. It is important to notice that the plot is of heat losses from the Reactor. All the heat conducted through one path from the Reactor to Slab3 is not necessarily passed on to the substrate by the same heat loss paths. For instance, more power is radiated to Slab3 than leaves it by radiation, balancing out by more conduction.

The second scenario is still in vacuum, but now with combustion heating the reactor. After calculating the heat flow for a given temperature distribution, the amount of propane and air flow needed to provide this power to the Reactor by combustion is introduced along with the added heat loss of the flow. 100% conversion of the propane is assumed, along with stoichiometric air flow. The results are shown in Figure 4-5. Notice that the forced convection starts out lower than the conduction

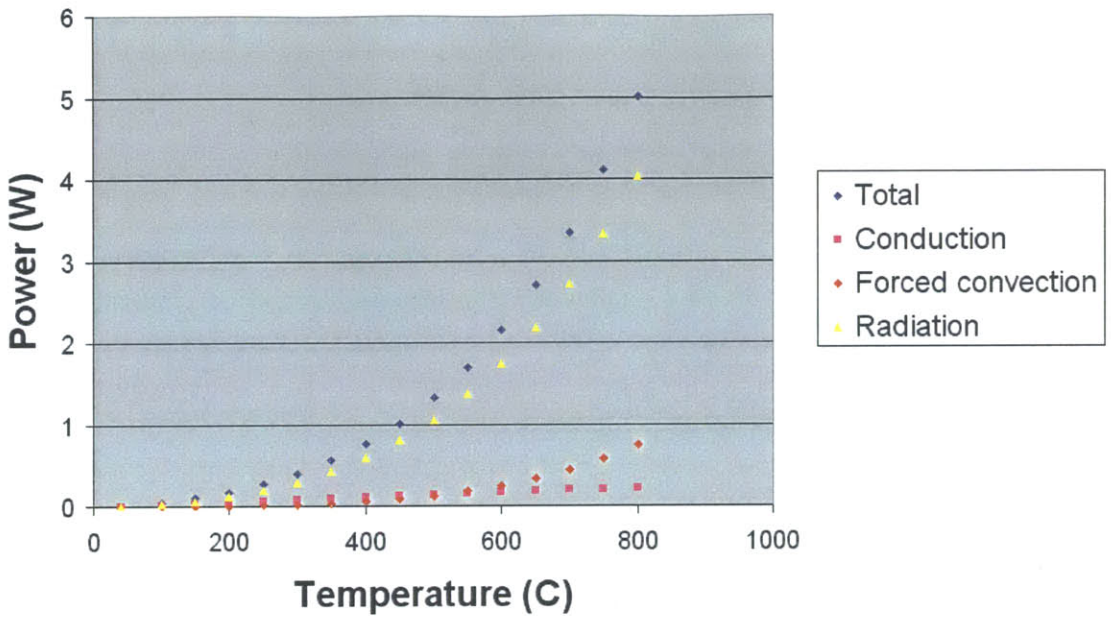

Figure 4-5: Reactor heat losses as a function of temperature in vacuum with gas flow forced convection. Total, conductive, convective and radiative heat losses plotted.

but overtakes it around 550°C. Also, close examination of the conduction shows that it is not altogether linear,since there is no solid conduction path from the Reactor to the Substrate.

For comparison, the total heat losses with and without forced convection are plotted in Figure 4-6. The extra heat losses introduced are not negligible, but they do not threaten the dominance of the radiation at higher temperatures. To quantitatively assess this dominance, a plot of the thermal efficiency, defined as the power radiated from the Reactor divided by its total heat loss, vs. temperature is given in Figure 4-7. Notice that it has a broad peak between 600°C and 700°C. Above this the increasing forced convection begins to limit the efficiency. Keep in mind that not all the radiated power is usable by the photocells, so higher temperatures will benefit the overall system performance.

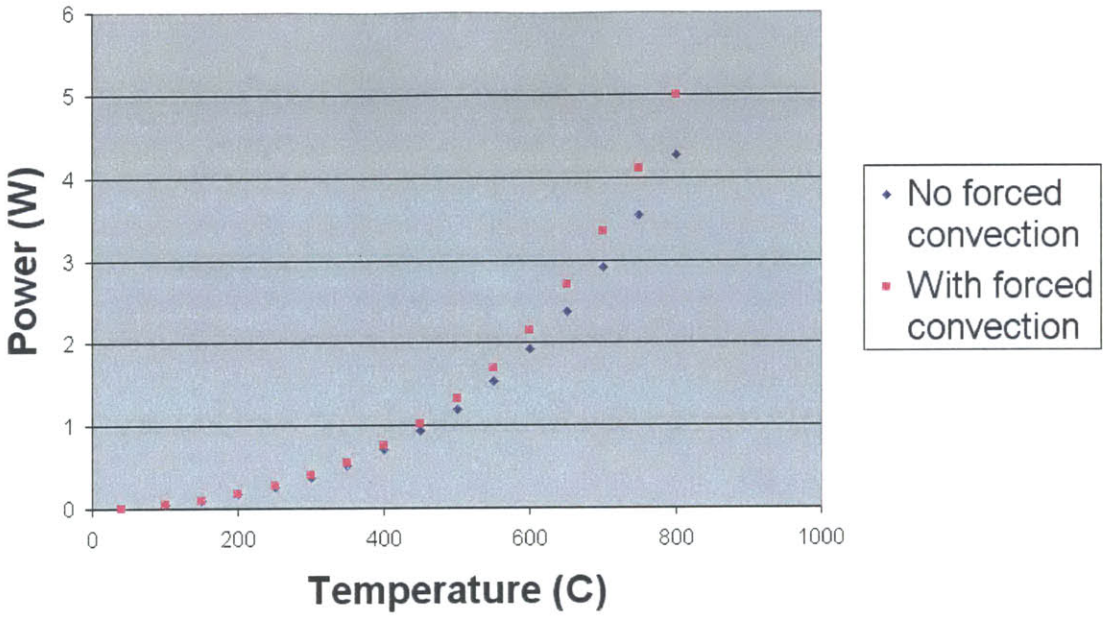

Figure 4-6: Total reactor heat losses as a function of temperature with and without forced convection.

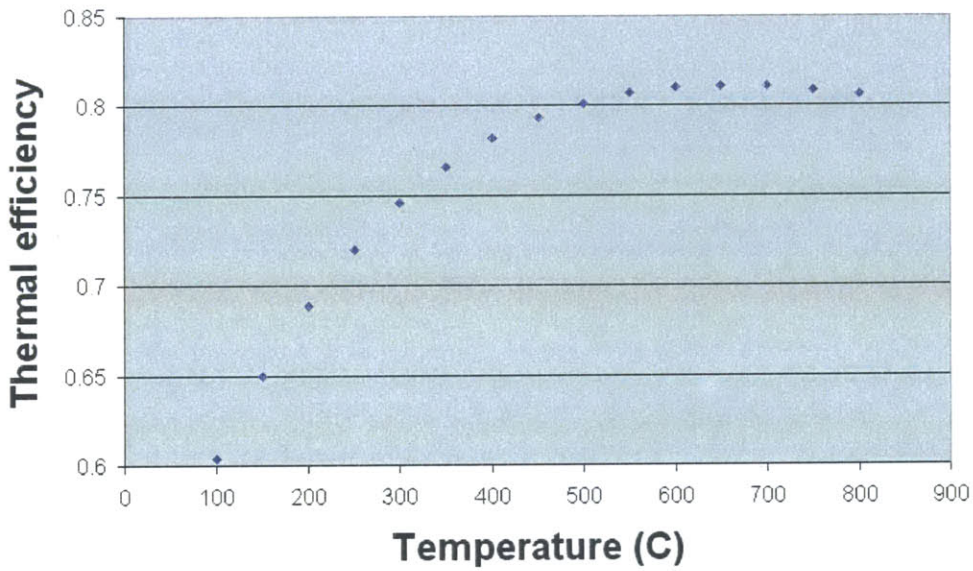

Figure 4-7: Thermal efficiency as a function of temperature (with forced convection). Thermal efficiency defined as radiated power from the reactor over total heat losses.

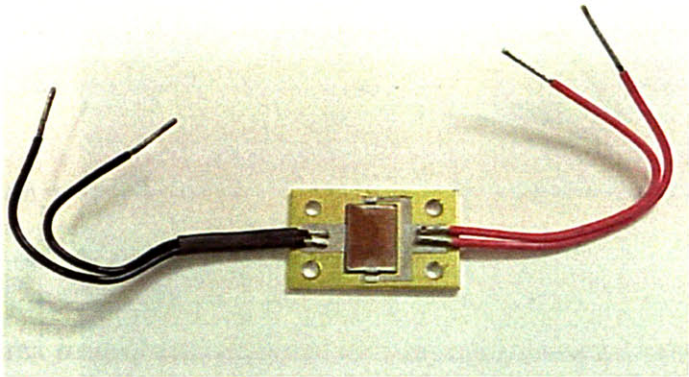

Figure 4-8: Mounted photocell without filter, with 4 leads for Kelvin measurements (JXCrystals Inc.).

4.4 Photocells

4.4.1 Photocell characterization

Diffused junction gallium-antimonide (GaSb) photocells were used for this thesis work. The cells, with an active area of 1x1.2 cm, were produced and mounted with test leads to heat conductive plates by JXCrystals Inc. (see Figure 4-8). GaSb was used because it is the material with the lowest bandgap commercially available. Cells with and without filters were used. The filters, mounted on top of the cells, are 9-layer dielectric filters, produced by the same manufacturer.

The photocells were characterized by David P. Jenicek, under the supervision of Dr. Ivan Celanovic. The experimental setup consisted of a heated silicon carbide emitter of dimensions 7.5x7.5 cm, with the photocell situated directly above it, at a variable distance (9-34 cm). The photocell was cooled with a water-cooled heat sink, most of the heating coming from natural convection of the air above the emitter. The temperature of the cell was controlled by changing the distance of the cell from the emitter surface. Figure 4-9 shows the data normalized by dividing by the viewfactor (since this changes with the distance). The plot gives an indication of the power output that can be expected with different emitter temperatures (with a view factor of 1). While higher cell temperatures were expected to create poorer performance, this may have been balanced by the closer distance to the emitter yielding a more intense

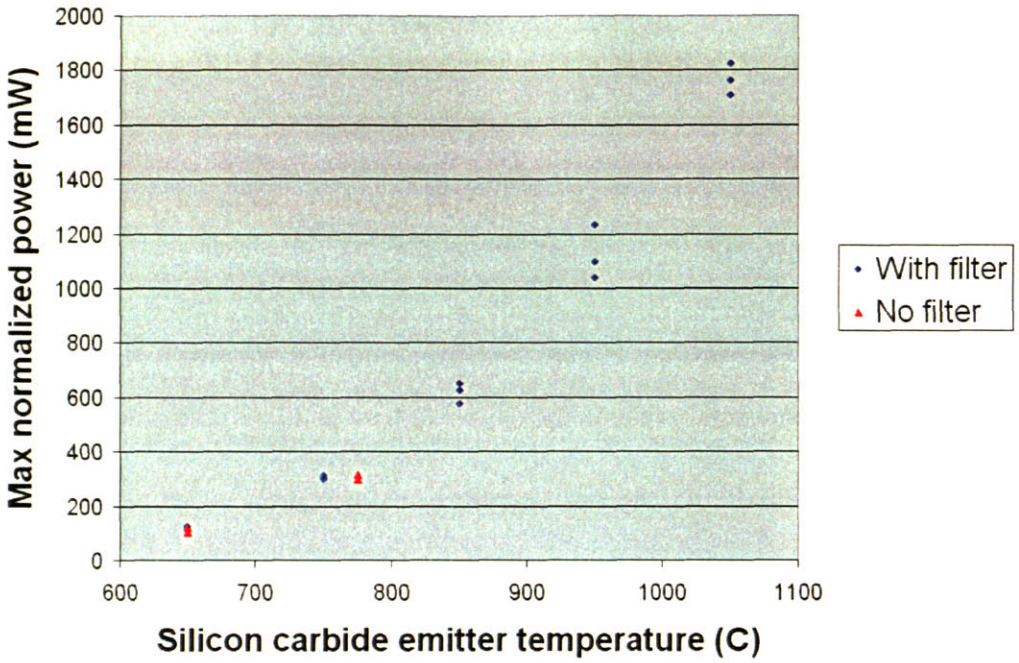

Figure 4-9: Maximum normalized power vs. emitter temperature for GaSb photocells, with and without filter.

illumination, which would give a better performance. Essentially, no conclusions can be drawn from the temperature data. This equally holds true for the fill factors, although they are clearly a little lower for the cell without filter. The power for the filtered cells is essentially equal to that of the unfiltered cells. This excellent performance of the filter is partially due to the large distance between the cell and the emitter resulting in mostly orthogonal radiation reaching the photocell.

4.4.2 Partial illumination

An interesting situation arises, particularly with SμRE I, where the area of the emitter is smaller than that of the photocell, and the distance between them is so small that parts of the photocell do not receive any considerable amounts of illumination. This illumination of only part of the photocell area has negative impact on its performance, because while the dark current is still proportional to the photocell area, the photocurrent is proportional only to the illuminated area. In a simplified manner,

this can be described to the first order by the following equations. The current at any given time in the diode is

$$I = qA_{pvc}(\frac{L_h}{\tau_h}p_{n0} + \frac{L_e}{\tau_e}n_{p0})(e^{\frac{qV}{k_BT}-1}) - qA_{ill}G(L_h + L_e) = I_S(e^{\frac{qV}{k_BT}-1}) - I_{ph} \quad (4.12)$$

where q is the electron charge, A_{pvc} and A_{ill} are the area of the photovoltaic cell and the illuminated area respectively, L is the diffusion length and τ is the carrier lifetime for *h*oles and *e*lectrons, p_n0 and n_p0 are the minority thermal equilibrium minority carrier concentrations, V is the voltage on the diode, T is the temperature, k_B is the Boltzmann constant and G is the carrier generation rate caused by the illumination. I_S is the saturation current (or dark current) and I_{ph} is the photocurrent. From Equation 4.12 the formulas for the short circuit current ($V = 0$), I_{sc}, and the open circuit voltage ($I = 0$), V_{oc}, can be deduced.

$$I_{sc} = -qA_{ill}G(L_h + L_e) = -I_{ph} \quad (4.13)$$

$$V_{oc} = \frac{k_BT}{q}\ln\frac{I_{ph}}{I_S} = \frac{k_BT}{q}\ln\frac{A_{ill}G(L_h + L_e)}{A_{pvc}(\frac{L_h}{\tau_h}p_{n0} + \frac{L_e}{\tau_e}n_{p0})} \quad (4.14)$$

Using these equations to compare the characterization results of the photocells (for which the whole cell was illuminated) with illumination by the SμRE, let $I_{sc,0}$ and $V_{oc,0}$ be the values from the characterization. For these, $A_{ill} = A_{cell}$. Also, let $I_{sc,p}$ and $V_{oc,p}$ be the values for the partial illumination case. Then we have the following:

$$I_{sc,p} = \frac{A_{ill}}{A_{pvc}}I_{sc,0} \quad (4.15)$$

$$V_{oc,p} = \frac{k_BT}{q}\ln\frac{A_{ill}}{A_{pvc}} + V_{oc,0} \quad (4.16)$$

Assuming that the fill factor does not vary much (which may not be entirely true, but is a necessary assumption), one can compare the maximum power outputs by comparing the products of I_{sc} and V_{oc}. This assumption also allows using the V_{oc}

data, normalized by dividing by the square root of the view factor.

$$\frac{P_{max,p}}{P_{max,0}} \approx \frac{I_{sc,p}V_{oc,p}}{I_{sc,0}V_{oc,0}} = \frac{A_{ill}}{A_{pvc}}(1 + \frac{\frac{k_BT}{q}\ln\frac{A_{ill}}{A_{pvc}}}{V_{oc,0}}) \tag{4.17}$$

For SμRE I, the reactor surface has an area of 3.15 mm^2, so assume for simplicity that this is also the illuminated area. The GaSb photocell used has an are of 1.2 cm^2, that A_{ill}/A_{pvc} is equal to 0.02625. Furthermore, the silicon carbide heater used for the photocell characterization has an emissivity of about 0.9, whereas the reactor is at 0.7. This must be corrected for. Assuming the photocell has a temperature of about 75°C, Equation 4.17 then becomes

$$\frac{P_{max,p}}{P_{max,0}} \approx (\frac{0.7}{0.9})(0.026)(1 - \frac{106mV}{V_{oc,0}}) = (0.020)(1 - \frac{106mV}{V_{oc,0}}) \tag{4.18}$$

While this result includes many approximations, not least about the photocell processes, it should give some indication of the reduction in power as a result of the partial illumination.

Chapter 5

Experiments

5.1 Overview of experiments

To characterize SμRE III and prove its utility for TPV power generation, it is desirable to carry out a number of experiments on the devices.

- Thermal characterization
- Mechanical characterization
- Combustion testing
- TPV power production testing

The thermal characterization aims to determine the magnitude of the various heat loss paths of the device for different reactor temperatures. Experience from SμRE I shows that it is difficult to control the temperature of the reactor while running an autothermal combustion in it. The electrical resistive heater is therefore used for these tests. The reactor is heated by applying a voltage across the resistor leads. The power input is easily measured along with the temperature of the reaction chamber, using the change in resistance with temperature. By increasing or decreasing the voltage, the temperature can be set arbitrarily, and a plot of power vs. temperature is obtained. This test can be carried out relatively easily in both air and vacuum.

Two things are important to note. First, the measured heat loss is from the reactor only, since this is where the 4-point measurement is taken. This means that information about the temperature and heat losses of individual heat exchangers are not experimentally known. Second, the test is initially carried out without any gas flow through the tubes. This eliminates one important heat loss path, which allows breaking the results down into the other paths more easily. By subtracting the the vacuum results from the results in air, the heat loss to air conduction and natural convection is extracted, since it is the only difference between the two. Furthermore, solid heat conduction is linear with temperature, and since radiation at low temperatures is negligible, a tangent can be drawn to the heating curve near room temperature to obtain the conduction component at all temperatures.

The mechanical characterization essentially has three parts. The first is merely to observe what kind of handling the device can withstand. While SμRE I could withstand being dropped in some cases, this is unlikely with SμRE III because of its much heavier reaction chamber. The second is to measure the burst pressure of the device. This is done by shutting the fluidic outlets of the device and flowing air into it slowly, monitoring the pressure. When a tube bursts, the pressure will immediately drop. Since there are 4 separate flow paths in the reactor, this test can be done 4 times per device. The third mechanical test is related to the fluid mechanics. It is simply measurement of the back pressure in the device for various flow rates. This can be done with an unreleased device, since thermal considerations are not important.

Combustion testing can be carried out on devices successfully loaded with catalyst. This loading procedure is described in Section 5.2.2. While flowing an appropriate amount of propane and air through the reactor, a voltage is applied to the platinum resistor that heats the reaction chamber. When the reaction chamber has reached a critical temperature, the combustion reaction will initiate. Once it is running stably, the voltage is turned off to let an autothermal reaction of the fuel-air mixture take place. The temperature of the reactor is monitored with the resistor. The inlet flow is precisely known from operating mass flow controllers, and the outlet exhaust gases are analyzed using a mass spectrometer. The fraction of reacted propane (preferably

100%) multiplied by the input amount and the energy density, give the power furnished to the device by the reaction. Once again, a comparison between temperature and power loss can be made. The combustion test is most easily carried out in air, while it is more complicated to achieve in vacuum, particularly if the use of photocells are required, since it requires feeding both reaction gases to the device and water cooling to the photocells, inside a vacuum chamber.

TPV power production is simply done by locating a photocell above and/or below the reaction chamber, either during electrical testing or combustion testing as described above. The photocell temperature is measured with a thermocouple, and water cooling can be applied as needed. As already explained, combustion testing in vacuum with photocells can be difficult. However, testing with electrical heating is more easily achieved. If the device is only heated for short amounts of time to the desired temperature, active cooling of the photocell, and therefore a water feed, may not be necessary. I-V characteristics for the photocells at various illuminations are measured to obtain the maximum power at a given time.

The experiments described above together enable a very thorough characterization of SμRE III and its potential as a combustor-emitter in a TPV system. It also helps determine its potential usefulness for other tasks, such as hydrogen production. A description of the complete test setup used for the various experiments is given in Section 5.3.

5.2 Device preparation

Once the devices have been released with TMAH, three important preparation steps are taken before they are ready for testing. These include applying the packaging chips to protect the reactor during handling, loading of the catalyst into the reaction chamber and mounting the device on an aluminum bar provides fluidic connections, stability and quick switching capability of devices to the test setup.

5.2.1 Packaging

Although the packaging chips do not provide a complete protective cover to the device, they are crucial in avoiding breaking the tubes. Moving an unpackaged device around on a very flat surface can be enough to pull the reaction chamber loose, by friction or by particles on the surface creating a small high difference between the reactor and the substrate. The chips are bonded to the device with a glass tape. The procedure was developed by Kerry Cheung and is described in detail in his Master's thesis [4]:

The tape has protective films on both sides. The side with adhesive is removed first and the tape applied to the packaging chip. After pressing it tightly to the surface with a rubber stamp, the other protective layer is removed. The chip is then heated to 450°C in air to burn off the organic binders in the tape. Figure 5-1 shows the packaging chips with and without glass tape applied. After this presintering, the chips are placed on each side of the reactor in a stainless steel chuck with lid (see Figure 5-2(a)) which allows pressure to applied to the devices in a controlled fashion. The chuck with devices is then loaded back into the furnace with heavy weights on top and heated with the following procedure: Ramp to 450°C at 2° per minute, hold for 1 hour, ramp to 525°C at 2° per minute, hold for 40 minutes, ramp down to room temperature at 3° per minute. This allows the glass to reflow and bond the packaging chips securely to the devices without any risk of leaky fluidic connections.The devices can now be handled a little more easily although still with care. Figure 5-2(b) shows a picture of a packaged device.

5.2.2 Catalyst loading

Inserting catalyst into the reaction chamber is more complicated than might be expected. The first reason for this is that the catalyst cannot be inserted during the fabrication of the device. The easiest time to insert it would be before bonding the wafers together. However, the catalyst material of choice, platinum, cannot be applied prior to bonding, because it would not survive the following 1000°C anneal and would not be allowed in the LPCVD silicon nitride furnace. Even if it were allowed

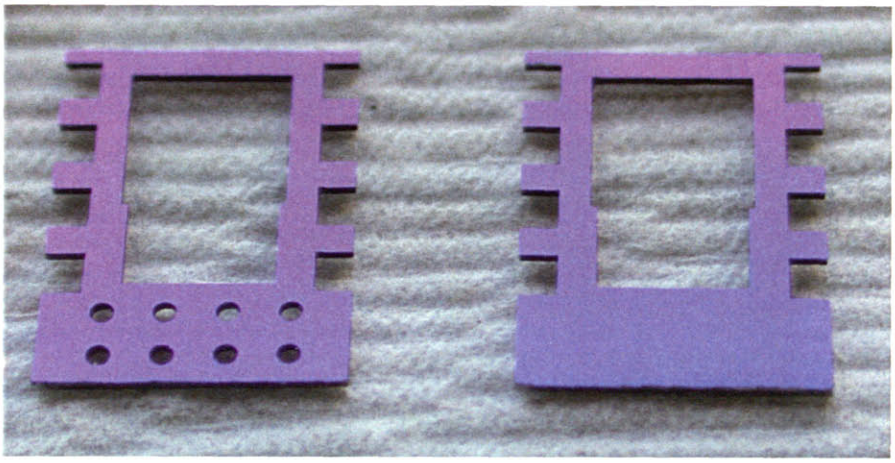

(a) Packaging chips before applying glass tape.

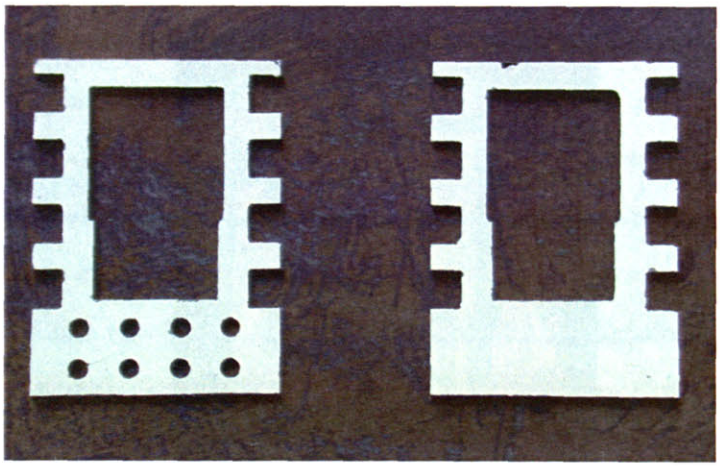

(b) Packaging chips with presintered glass tape layer.

Figure 5-1: Packaging chips with and without glass frit.

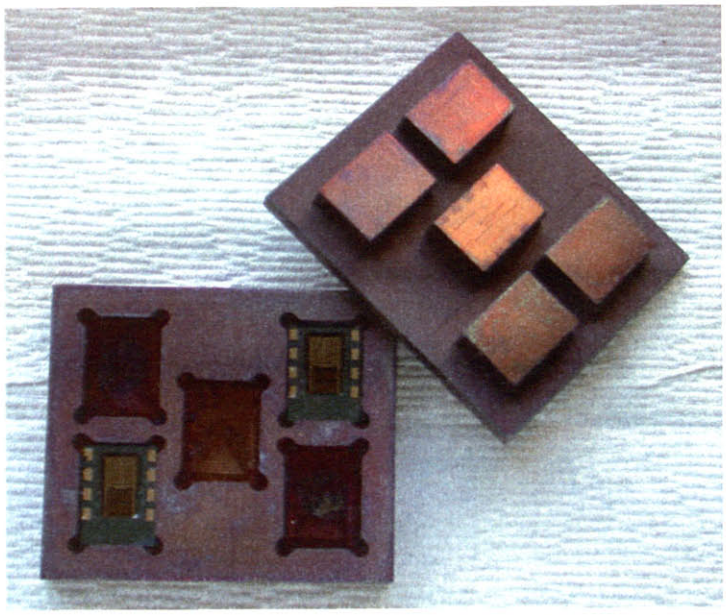

(a) Stainless steel packaging chuck with two devices to be bonded.

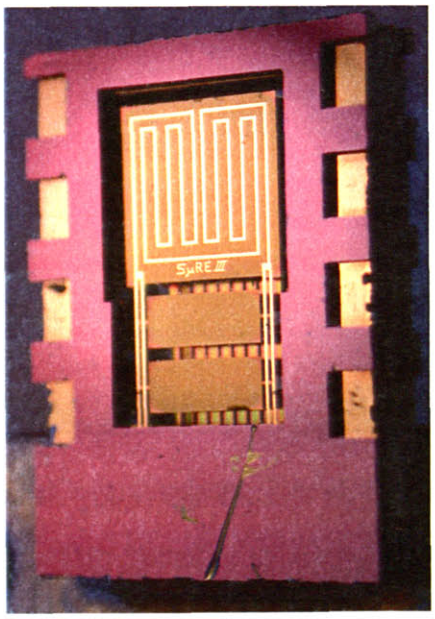

(b) Packaged SμRE III.

Figure 5-2: Packaging chuck and complete packaged device.

in the furnace, it would get covered up with silicon nitride, rendering it useless for combustion applications. This leaves inserting the catalyst afterwards as the only solution.

The second complicating factor is that the catalyst must not be deposited in the inlet tube of the device. If this happens, the fuel can light off before reaching the reaction chamber, which not only leads to heat being dissipated in the wrong place but also to breakage of the tubes. Because the tubes themselves are thermally insulating, a combustion reaction in the free-standing tube area quickly leads to excessive heat and stresses, resulting in device failure. This was observed in SμRE I [1].

The solution developed is described in detail in Leonal Arana's Ph.D. thesis [1] and is explained here in short form. First, the channels of the released and packaged device is treated with a silanizing agent, n-octyltriethoxysilane (OTS, United Chemical Technologies), to make the inner surfaces slightly hydrophobic. The OTS, dissolved at 2 vol% in ethanol, is inserted into the channels with a syringe, and after a few minutes the channels are flushed with ethanol. The device is then dried at 70°C fir 15 minutes and cured at 120°C for 1 hour. A supported platinum catalyst on an alumina support structure, with a grain size of about 1 μm, is then suspended in water and inserted into the *outlets* of the reactor, again with a syringe, after it is completely released and packaged. The suspension then wicks into the channels, working its way into the device until it reaches the fluidic stop valve, located at the end of the inlet of the reaction chamber. Because of the surface tension created by the contact angle and the sudden expansion, the water will not move past this point. This assures that no catalyst is deposited in the inlet tubes. The device is then dried at 50-70°C, and the device is ready. While Figure 5-3 shows the stop valves of SμRE III, the principle is more clearly illustrated by the picture of SμRE I in Figure 5-4.

Notice that SμRE III has stop valves at all entrances to the reaction chamber. This allows an arbitrary choice of which end of each flow path should be the inlet and outlet, because the stop valves only present a sudden expansion in one direction. The purpose of this versatility is to run combustions in different configurations to see whether it makes a difference to the thermal uniformity of the reaction chamber

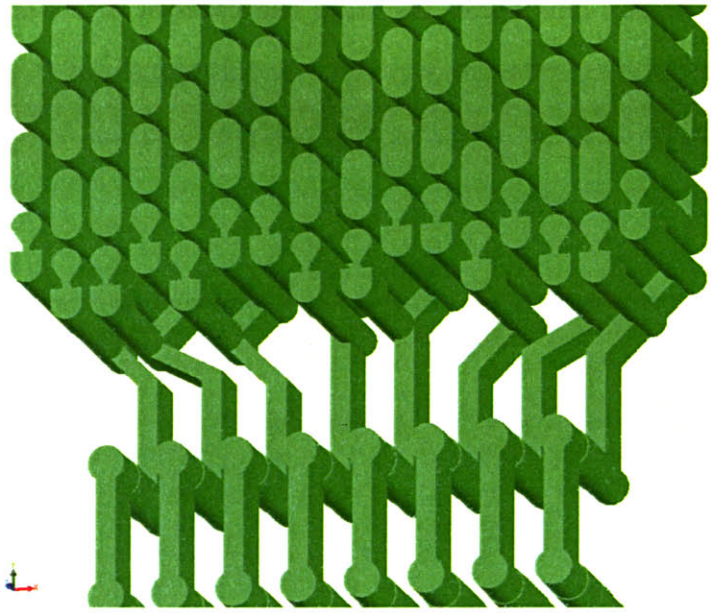

Figure 5-3: Model of stop valve constrictions in SμRE III reaction chamber.

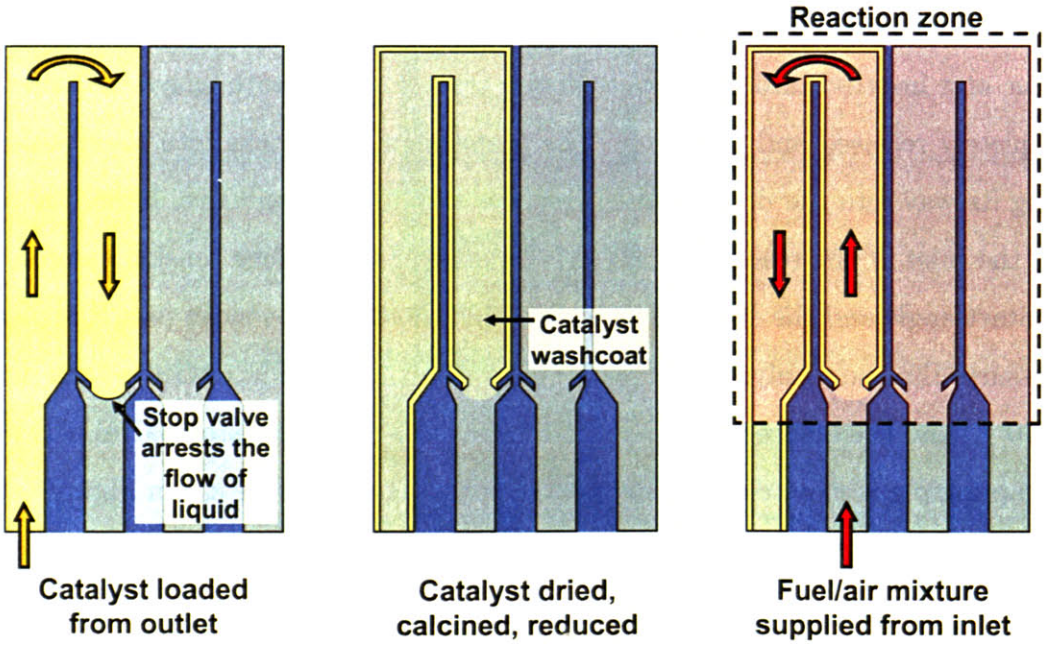

Figure 5-4: Schematic of SμRE I catalyst loading with stop valves [1].

during operation.

5.2.3 Aluminum fixtures

Interfacing the devices with the fluidic connections of the testing equipment is done using small aluminum bars (see Figure 5-5(a)) with fluidic connections and holes for attachment to the test equipment. The devices are attached to the bars using a high temperature epoxy (to allow heating the substrate to 100°C to avoid water condensation in the exhaust) and a mounting jig shown in Figure 5-5(b) and 5-5(d). The jig aligns the holes of the device with the holes of the bar. Once a device is mounted to one of these aluminum fixtures, it can easily be screwed on to the test setup for quick device change. A picture of a mounted device is shown in Figure 5-5(c). The reason for this "diving board" configuration is to allow photocells to be placed above and below the device. At this point, the device is ready for testing.

5.3 Test setup

5.3.1 Hardware

The physical test setup has two main domains: the fluidic and the electrical. Figure 5-6 shows a schematic of the fluidic part of the setup, and Figure 5-7 shows pictures of it. Four mass flow controllers (2 for propane and 2 for air) control the flow of fuel and air to the device. Propane and air are mixed at two T-intersections in the tubing, giving two separate flows. While the devices have 4 separate flow paths, 2 and 2 are connected together in the testing equipment for simplicity. However, either of the two can be closed, so that only one channel is in use, if so desired. Two pressure gauges monitor the device inlet pressure. The device mounted on the aluminum bar is attached to the aluminum flow manifold, with all the fluidic connections. This manifold, along with all the valves involved in the exhaust flow path (built into the massive aluminum plate) are heated by cartridge heaters to 100°C to avoid condensation. The tubing between these are also heated, but to avoid

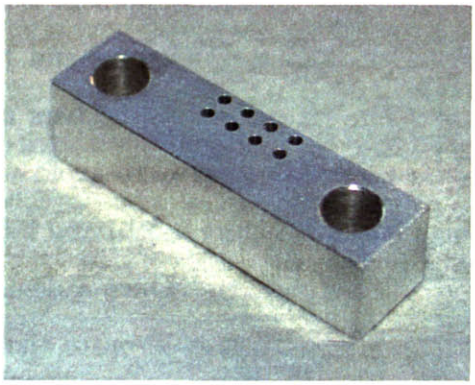

(a) Aluminum bar with 8 fluidic connections and 2 holes for attachment to test setup.

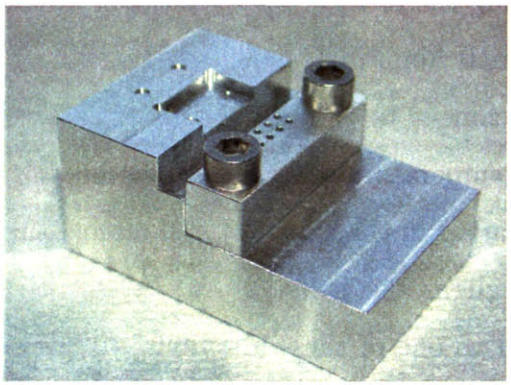

(b) Mounting jig for proper alignment of fluidic connections.

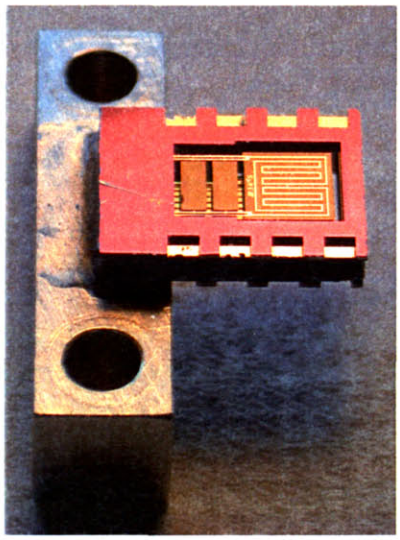

(c) SμRE III mounted on aluminum bar with epoxy.

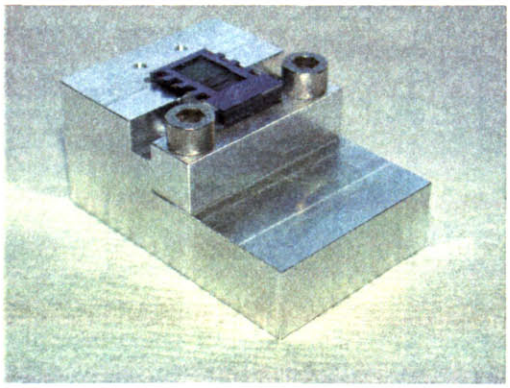

(d) Mounting jig with device.

Figure 5-5: Mounting of SμRE III to aluminum bars serving as interface with the test setup.

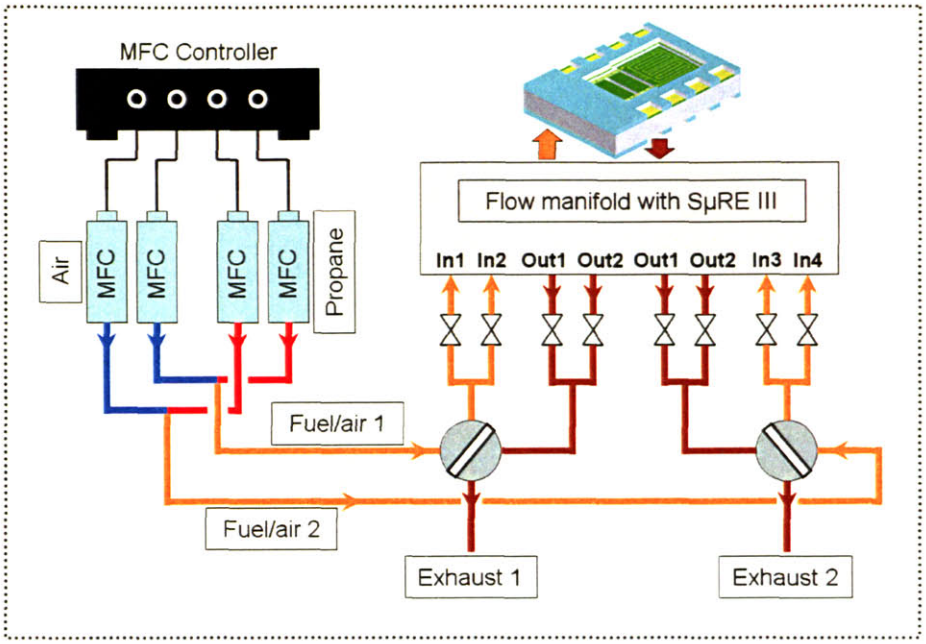

Figure 5-6: Schematic of fluidic test setup. Color scheme: blue=air, red=propane, orange=fuel/air mixture, brown=exhaust. All valves and lines in exhaust path are heated to avoid condensation of water.

very complicated wrapping of heating tape, these are located inside the insulated box, which can be capped with a lid, and where the air heats up along with the aluminum. Various thermocouples are used to monitor the temperatures of these. The two exhaust streams are fed to a mass spectrometer for analysis.

An important feature of this fluidic setup is the bypass that allows flowing the gases around the device. This is achieved with two 4-way valves. When starting the flow of gases, the device is bypassed until the desired flow is stabilized. The mass flow controllers often deliver slight spikes in flow rate when turned on or changed drastically. These spikes can cause momentary surges in pressure be enough to break the silicon nitride tubes. Using the bypass loop avoids these problems.

On the electrical side of things, clips are used to connect to the 8 connection pads on the device. A 120V/250mA DC power supply delivers the voltage to the resistive heater, and this voltage along with the 4-point voltage measurement and current flow, are monitored by an HP34970A Data Acquisition Switch Unit, which also can monitor as many temperatures as is necessary, using thermocouples. The photocell I-

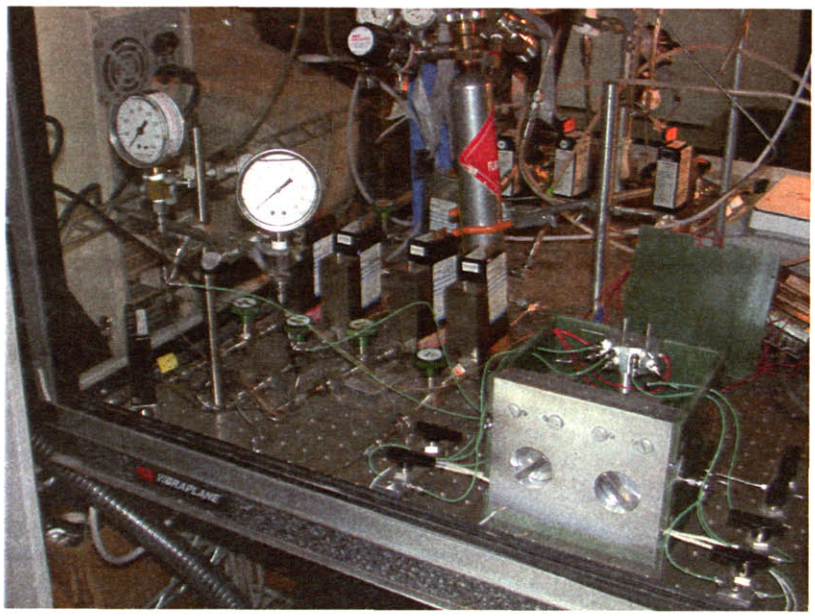

(a) Fluidic test setup with gas supply and flow manifold.

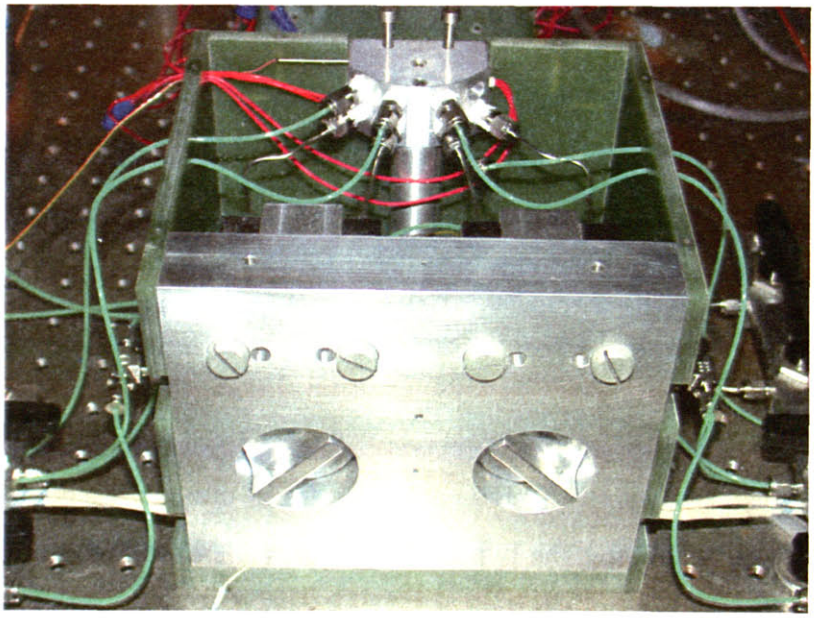

(b) Heated flow manifold and valves.

Figure 5-7: Fluidic part of the test setup for SμRE III.

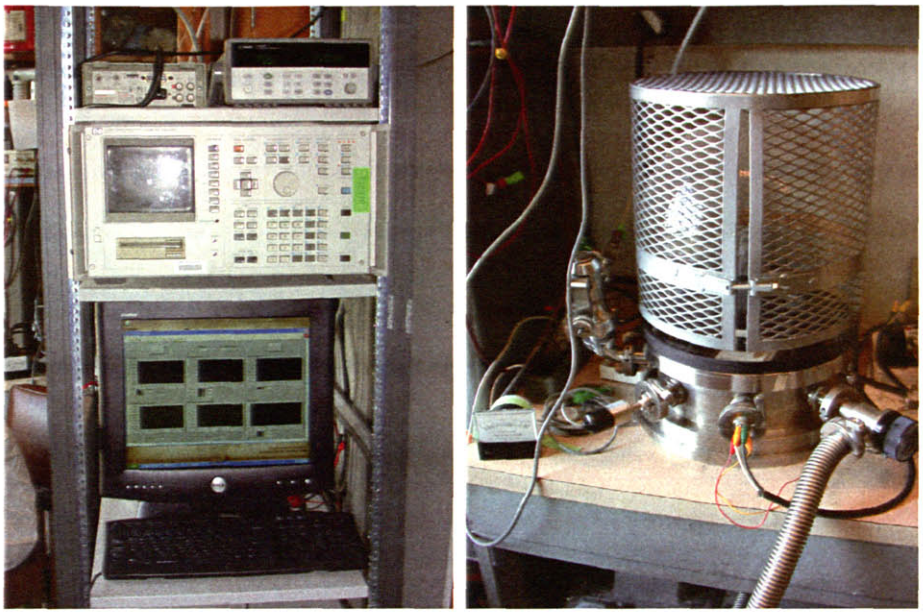

(a) Electrical part of test setup.

(b) Bell jar used for vacuum testing of SμRE III.

Figure 5-8: Electrical test rack for SμRE III and bell jar for vacuum testing.

V characteristics are measured using an HP4145B curve tracer. It has two channels, which allows it to measure both photocells simultaneously. Cell temperatures are monitored with thermocouples. The rack with computer and the electrical equipment is shown in Figure 5-8(a).

For testing in vacuum, a bell jar, shown in Figure 5-8(b), is used with a roughing pump capable of pumping it down to about 12 mTorr. Electrical connections are run through an electrical port on the side of the chamber. Only electrical heating is used in the vacuum, and the photocell cannot be cooled actively.

5.3.2 Software

The HP34970A and HP4145B are both controlled by a LabView® program written by Rebeca C. Diaz, connected to the computer via a GPIB interface. A picture of the graphical user interface is shown in Figure 5-9. The program plots important data in real time, allowing for on-the-fly performance analysis. The top left graph plots

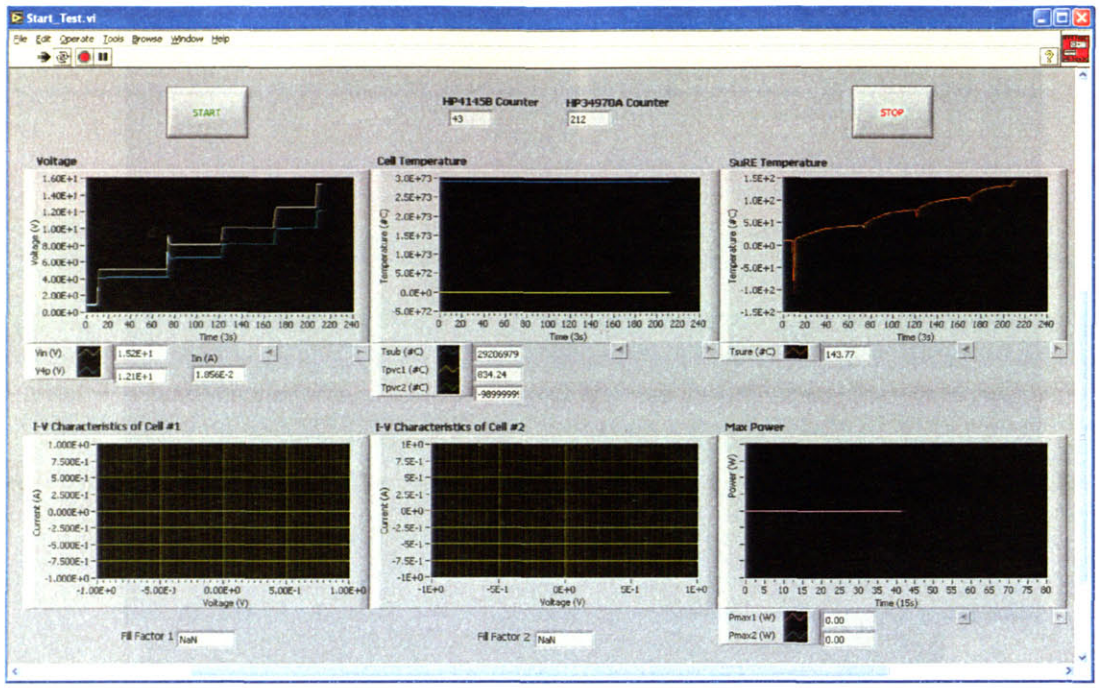

Figure 5-9: Screen capture of the graphical user interface of the test software. In this particular instance the photocells are not being used.

the input and 4-point voltages. Below it are given the instantaneous values of these, along with the current. Monitoring these allows quickly realizing if there is a change in the resistive heater integrity or contact problems. The top middle graph plots the temperatures of the photocells, while the top right graph plots the calculated reaction chamber temperature. This is extremely useful data to have real time, since it has to be derived from the change in resistance. The two bottom graphs give the I-V curves for the photocells as well as a trace of maximum power over time. Because the speed of the HP4145B is not quite as high as that of the HP34970A, the HP4145B is only probed every 12 seconds, while the HP34970A is probed every 2 seconds.

The usefulness of this software cannot be understated. It allows tweaking voltages and flow rates without having to worry about data gathering, but it also gives real time feedback of crucial information that would normally be derived from the raw data after the experiment.

Chapter 6

Experimental results

6.1 SμRE I experimental results

6.1.1 Test setup

Autothermal combustion of propane in air was successfully carried out in SμRE I, along with TPV power generation, yielding a net electrical power output. A simple schematic of the test setup is shown in Figure 6-1. The setup is essentially identical to that of SμRE III. Only one photocell is used, above the reactor, because the device does not protrude far enough from the aluminum fixture to locate a photocell underneath it. This is simply a consequence of the size of the device, and the length of SμRE III was increased to eliminate this problem. Additionally, the electrical clips used impose additional constraints below the device, as seen in the picture in Figure 6-2. This figure also shows one of the gallium-antimonide (GaSb) photocells used for the testing. The cell pictured here has a 9-layer dielectric filter attached to the top of the cell surface, but the results below are from a photocell without filter. During the experiments, the cell was cooled passively with an aluminum fin structure. A 1%wt. Pt on La-doped γ-Al_2O_3 (Alcoa Ga-200LSF Alumina), reduced ex-situ in hydrogen at 300°C, was used as a combustion catalyst. Combustion products were monitored using an on-line mass spectrometer (Inficon) and micro gas chromatograph with TCD detection (Agilent).

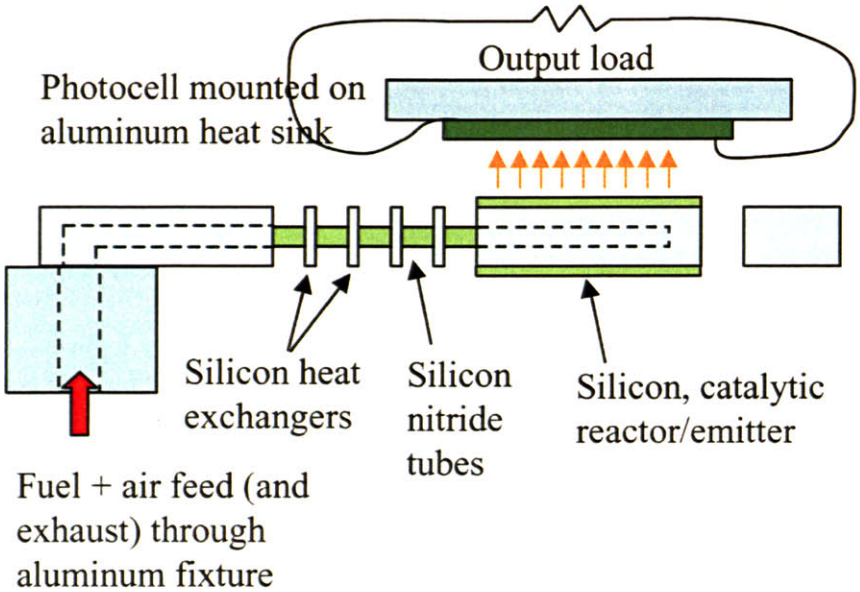

Figure 6-1: SμRE I TPV power generation test setup schematic.

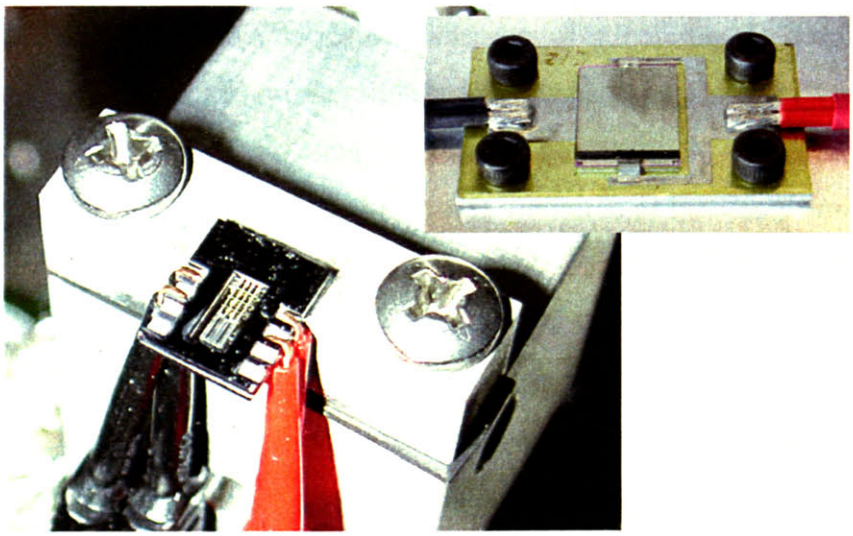

Figure 6-2: Pictures of SμRE I mounted to aluminum fixture and GaSb photocell with filter.

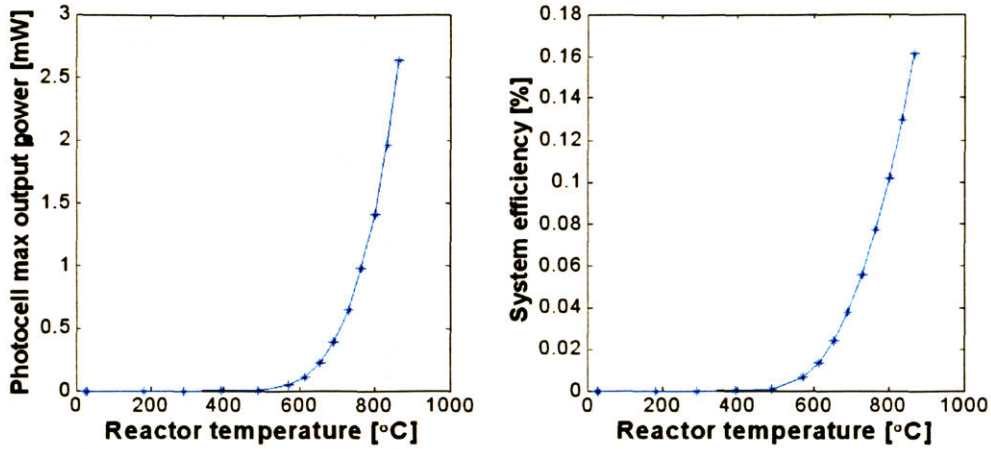

Figure 6-3: SμRE I TPV power generation vs. temperature (with electrical heating).

6.1.2 TPV power output with electrical heating

To characterize the emitter/photocell pair over a range of temperatures, SμRE I was heated electrically with the photocell placed above it. Details on the thermal characteristics of SμRE I itself are found in Leonel Arana's Ph.D. thesis [1]. Figure 6-3 shows the results for the maximum photocell power output and the efficiency. The efficiency is here defined as the electrical power produced by the cell divided by the electrical power delivered to the reactor. The steepness of the curves is explained by two factors. On the one hand, radiation is proportional to temperature to the fourth power. On the other hand, as the temperature increases, a larger percentage of the radiated spectrum becomes useful for the photocell and therefore convertible into electrical power. This is illustrated in Figure 6-4, showing the spectrum of a 0.7 emissivity grey body at 770°C and 1000°C, along with the bandgap of GaSb.

6.1.3 Combustion testing and net TPV power generation

Figure 6-5 shows a graph over time of the propane combustion rate during a test run of SμRE I. Initially, the propane and air flows are stable, and the temperature is gradually increased with the electrical heater until ignition occurs. This transition is marked by a sharp increase in the combustion rate. After the reaction stabilizes, the electrical power is turned off (marked by a small dip in the combustion rate), and the

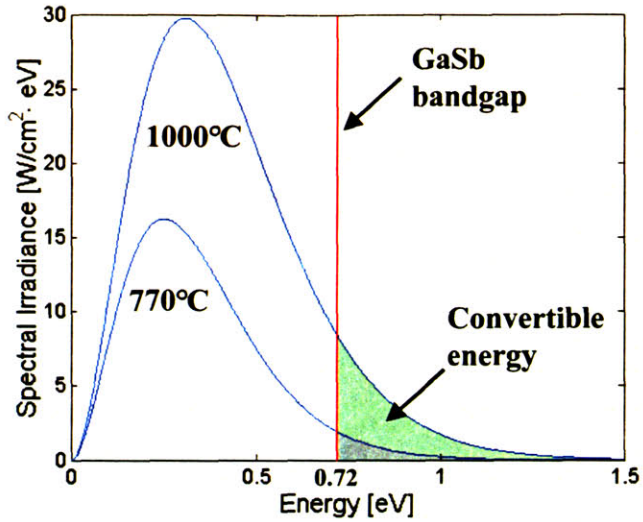

Figure 6-4: Radiation spectrum of a grey-body emitter of emissivity 0.7 (i.e. the SμRE) at 770°C and 1000°C, with the bandgap of GaSb marked.

combustion continues autothermally, sustaining itself by the heat of reaction, with constant thermal emission at 770°C.

During autothermal combustion, the photocell was approached above the reactor, and the maximum power output was 1.0 mW, which corresponds to a power density of 32 mW/cm^2 (based on *emitter* area). This constitutes net TPV electrical power generation. The system efficiency was 0.08%. The efficiency is here defined as the electrical power output of the photocell divided by the thermal power released from the combustion, *not* including the potential power of the unreacted propane. The reason for not including this, is that with sufficient catalyst loading and optimized gas flows, fuel utilization close to 100% should be avhievable. Fuel utilization was in fact 46% These results are summarized in Table 6.1.

This result can now be compared with that of the photocell characterization. The SμRE I emitter temperature of 770°C is very close to that of the silicon carbide emitter at 775°C for the photocell without a filter. Using the normalized V_{oc} from the characterization, 1003mV, Equation 4.18 gives the following:

$$\frac{P_{max,p}}{P_{max,0}} \approx 1.79 * 10^{-2} \tag{6.1}$$

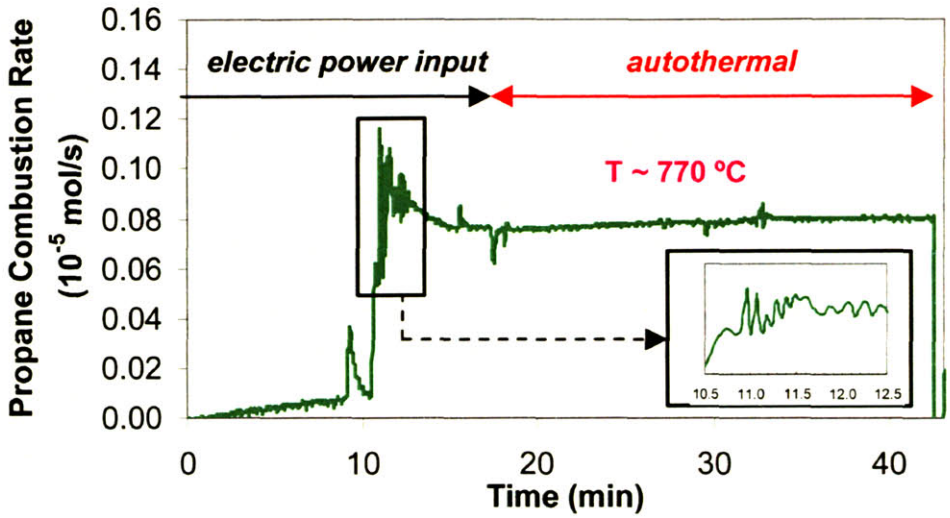

Figure 6-5: Propane combustion rate in SμRE I during test.

Table 6.1: SμRE I TPV power generation with autothermal combustion, with conservative predictions for improvements.

Fuel (propane)	
Flow rate	2 mL/min
Air flow rate	47.6 mL/min (stoichiometric)
Catalyst	1 %wt. Pt–Al_2O_3
Conversion	46%
Combustion power	1.3 W
SμRE I reactor	
Temperature	770°C
Electrical power input	0 W
GaSb photocell	
Power output	1.0 mW
Power density	32 mW/cm^2
System efficiency	0.08%
Projections	2 photocells, in vacuum, 1000°C
Power output	>16 mW
Power density	> 250 mW/cm^2
System efficiency	> 2.4%

The experimental results give about $1mW/310mW = 3.22 * 10^{-3}$, which is off by a factor of 5.6. Not only was the derivation of Equation 4.18 based on many assumptions, but there is also no temperature data available for the photocell temperature during the testing of SμRE I. Being only 1 mm away from the emitter in air with only passive cooling, it could easily have been at a much more elevated temperature, reducing its efficiency drastically.

6.1.4 Discussion

These recorded results are a proof of concept for the TPV micro-generator. Although power outputs and efficiencies are relatively low, they show promise for improvements, in particular with three basic modifications. First, using one photocell on each side of the reactor will double both the power and the efficiency. Second, vacuum packaging will eliminate heat losses to the air, increasing the radiative component of heat loss by a factor of three [1], thereby increasing the efficiency by a factor of three. Third, using a conservative extrapolation of the curves in Figure 6-3 to an emitter temperature of 1000°C, together with the two first improvements, a power exceeding 16 mW, corresponding to a power density of 250 mW/cm2 (based on emitter area), and an efficiency of more than 2.4%. These predictions are included in Table 6.1. Additional modifications, in particular in the optical domain (emitter surface, filters, mirrors) could lead to better performance. A smaller photocell and active cooling would undoubtedly improve performance as well, although this cannot be assessed quantitatively due to the lack of temperature data for the photocell.

These predictions are all based on SμRE I usage. Further improvements in cell illumination and other reactor improvements are expected from SμRE III, but unfortunately TPV power generation results have not yet been obtained with this device, for reasons described in Section 6.2.3.

6.2 SμRE III experimental results

6.2.1 Mechanical strength

Throughout the release process and device preparation steps it is clear that SμRE III is mechanically substantially weaker than SμRE I. While this was expected due to the 29-fold increase in reactor volume and weight while only doubling the number of supporting tubes, it is more fragile than expected from simple structural comparisons. The weak link seems to be the anchor points of the tubes to the heat exchangers. During device failure, the tubes most often break off at the point where they touch down on the oxide surface. While it is possible that the nitride-oxide interface gets slightly undercut in the release etch, leading to stress concentrations in this narrow area, it is more likely that the problem stems from imperfections from the center wafer through etch. As discussed in Chapter 3, etching the tube mold through the center wafer, with straight clean side walls, has proven difficult, in particular near the bottom when breaking through the wafer. These imperfections are most probably the main source of the device weakness.

6.2.2 Thermal characterization

Three devices were successfully tested with electrical heating to determine the thermal characteristics of SμRE III and compare to the modeling results. The testing was done in both air and vacuum, and a compilation of the results in shown in Figure 6-6. Overall the three devices show good agreements amongst themselves, particularly in vacuum. In air, at higher temperatures, some differences become apparent. These are possibly due to the varying ambient conditions surrounding the devices. Device #1 was tested in a ventilated hood, with plenty of air flow, leading to a higher rate of air convection, while the other two devices were tested in an unvented, open area. Since the results in vacuum agree so closely with each other, this seems a likely explanation, rather than differences in the construction of the devices that all came from the same silicon wafer stack.

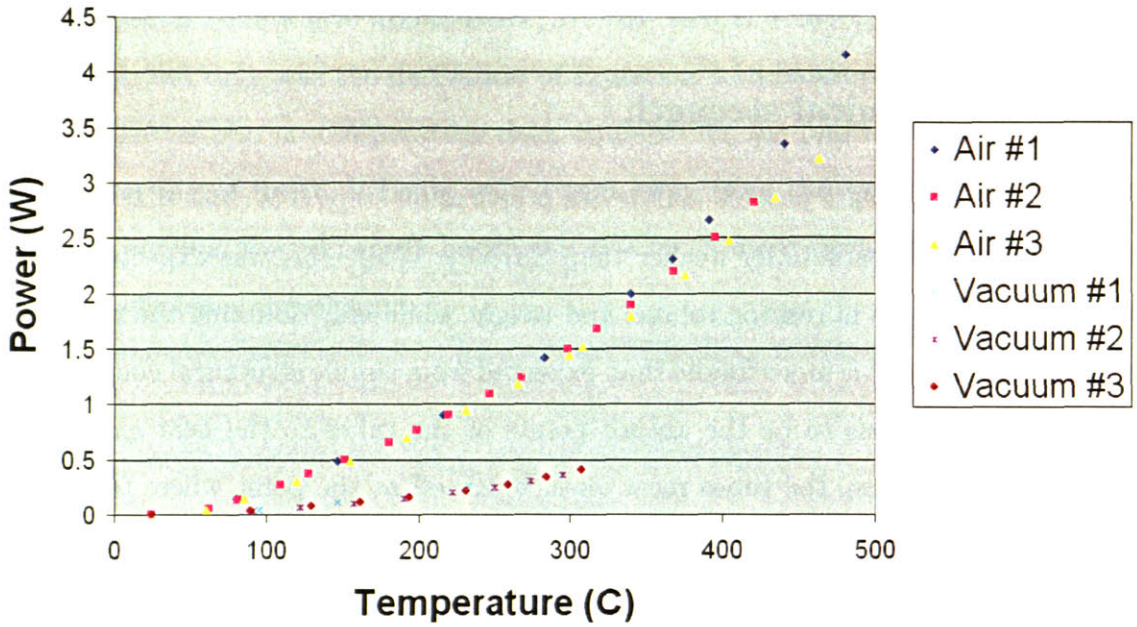

Figure 6-6: Thermal characteristics of three different SμRE III devices. Tests are done with electrical heating, in air and in vacuum.

Unfortunately the vacuum tests were not successful above $300°C$, because of a slight problem with the design. The metal leads running on the suspended nitride bridges, although providing a high thermal resistance for the thermal isolation of the reaction chamber, for the same reasons has very little heat losses from itself, which leads it to quickly heat up when current is passed through the metal. At elevated temperatures the platinum leads fail (presumably by agglomeration) and electrical contact is lost, rendering the device useless. While the temperatures reached should be sufficient to start combustion of propane, so that a combustion reaction could heat it up to higher temperatures, for the electrical testing, the range is quite limited. In air, higher temperatures are reached, as seen from Figure 6-6, because the relative losses to the air of the bridges compared to the reaction chamber is much higher because of the high surface to volume ratio of the bridges.

Figure 6-7 shows a plot of the test data for vacuum, along with the modeled results. The agreement between the two data sets is quite good, and this suggests that even at higher temperatures, the reactor would perform as expected from the

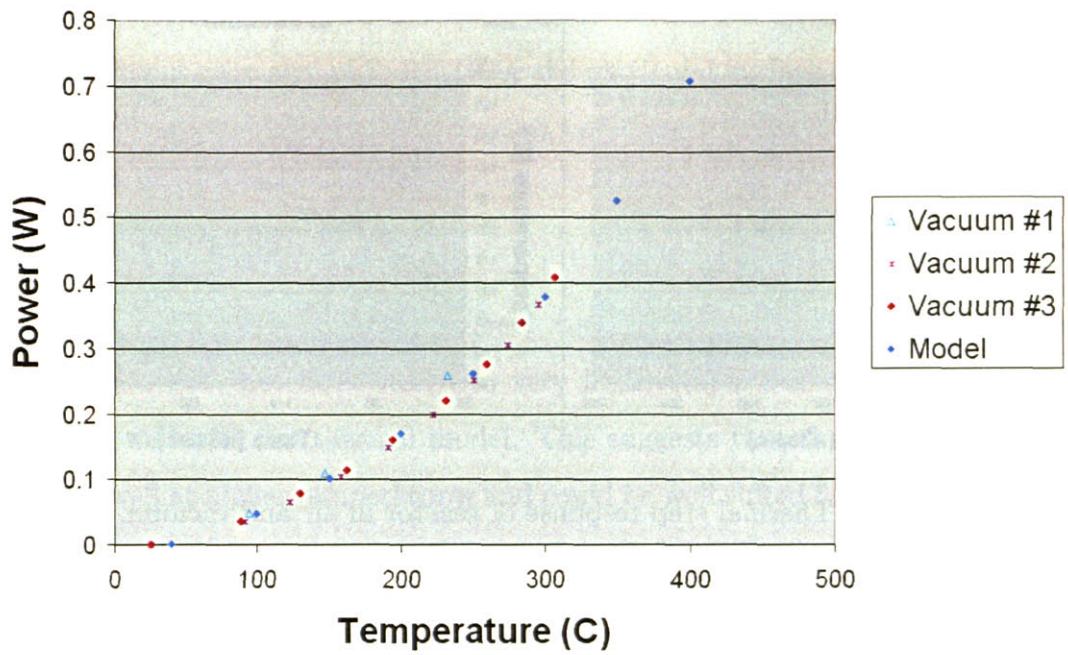

Figure 6-7: Thermal characteristics in vacuum compared with model results.

model, exhibiting a very high thermal efficiency.

The difference between the test results in air and vacuum can additionally be confirmed by comparing the thermal time constants of the same device in the two different ambient conditions. Figure 6-8 shows side-by-side comparisons of the temperature over time in air and vacuum for device #3, within similar temperature ranges. The curves are responses to approximate steps in power input to the device. Since the power is *not* linear with temperature, these responses are not exactly inverse exponentials, but an approximate time constant can still be extracted as a first order tool for comparison. From the plots, in air, the time constant is around 9-10 seconds, while in vacuum it is closer to 40-45 seconds. From 6-6, we see that the heat losses are about a factor of 4.5 higher around this temperature in air than in vacuum. With some margin of error within these measurements from the graphs, this matches quite well, since the thermal time constant in a linear system is equal to

$$\tau_{th} = R_{th}C_{th} \tag{6.2}$$

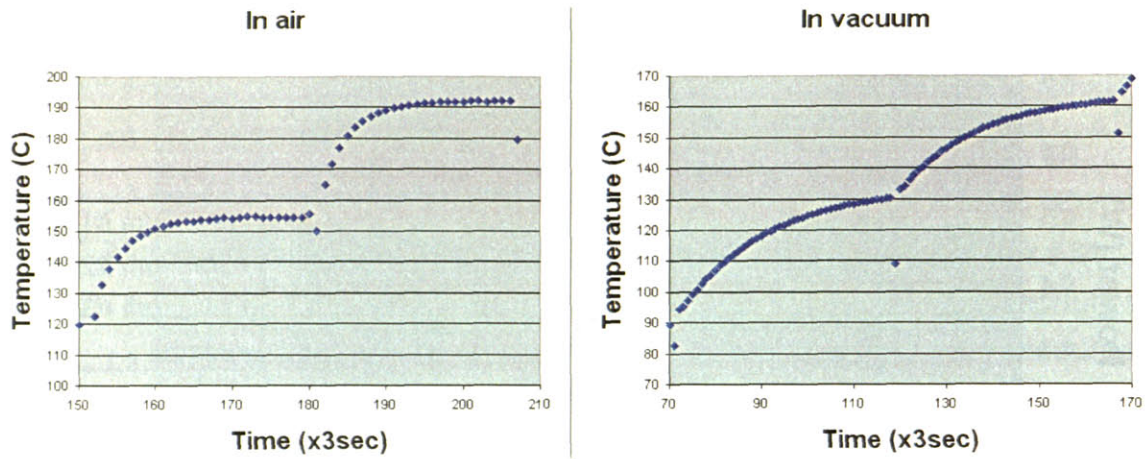

Figure 6-8: Thermal step response of reactor in air and vacuum.

where R_{th} is the thermal resistance (which is proportional to the inverse of the heat loss), and C_{th} is the thermal capacitance (which does not change between air and vacuum, other than whatever air may be contained in the reaction chamber). This result is interesting in that SμRE III is less dominated by air losses than SμRE I. This is logical since SμRE III is a larger device with a smaller surface-to-volume ratio.

6.2.3 Further testing

Unfortunately, further testing has not yet been successful. First, the pressure testing of the tubes has not been completed due to problems with leakage, either from the device-packaging chip interface or the device-aluminum bar interface. It is expected that a solution to this can be found. While this would also inhibit any fluidic testing, such as running a combustion in the device, this is more fundamentally hindered by problems with catalyst loading. Catalyst loading into the reaction chamber has not yet been successful. In particular, the catalyst suspension in water does not wick past the tube section into the reaction chamber. Potentially, the expansion going from the heat exchangers into the next tube could be stopping the liquid in a fashion similar to the stop valves. In any case, it is again expected that this could be solved, either by using a different silanizing agent or none, in conjunction with loading the exact amount of liquid needed to fill the internal volume of the reaction chamber and the

outlet tube section. The OTS silanizing agent worked for SμRE I, and it could be that the different geometry of SμRE III or the particular surface conditions inside the tubes from the different fabrication process, could necessitate a different approach.

6.2.4 Discussion

Although a number of tests have not been successfully carried out and the thermal characteristics have not been tested to very high temperatures, the data obtained agrees very well with the thermal model. This suggests that the devices would perform quite well at higher temperatures and could be well suited for TPV applications, with a higher (radiative) thermal efficiency than SμRE I. Further testing is necessary to confirm this. The fragility of the devices does raise some concern about the fabrication process. This could probably be improved by the use of different fabrication equipment and/or different rules for cross-contamination of machines.

Chapter 7

Conclusion

7.1 Principal achievements

The two principal achievements of this thesis work are the demonstration of net electrical power generated in a MEMS based TPV power generator system, and the successful fabrication of SμRE III, which improves upon the thermal efficiency of previous SμRE generations.

The electrical power generated during autothermal combustion of propane in air in SμRE I with a GaSb photocell, is a proof of concept for this technology. Within the field of TPV most of the research results have been focused on individual work either with emitters or photocells. This thesis therefore contributes to the few reported cases of combining these into a more complete system, in particular for portable power sources. The autothermal combustion of propane is in itself an important result in a field where hydrogen is most often used for experiments because of inadequate thermal isolation.

The design and fabrication of SμRE III pushes the limits of the suspended silicon nitride tube technology, pioneered with SμRE I. It also provides an interesting combination of fabrication techniques to achieve the peculiar geometry necessary to build tubes with circular cross-section. The high thermal efficiency of the device, due to both the tubes and the effective heat exchangers, is interesting in the context of any high-temperature chemical devices.

7.2 Limitations of SμRE III

Despite the good performance of SμRE III thermally, several limitations to the design and the technology in general are apparent. First, from the point of view of the design, the nitride bridges heating up very quickly and destroying the metal leads is a limitation that can easily be fixed by running them over the heat exchangers. This would introduce a higher amount of solid heat conduction from the reactor, but this would only slightly change an already high thermal efficiency. This would allow heating the device electrically to higher temperatures.

Several of the other problems, such as catalyst loading and good gas seals for testing, can be solved with time and effort. Since this has been demonstrated in SμRE I, there is no particular reason why this should be unsolvable.

A more fundamental problem with the device is the fragility, introduced mainly by the anchor points of the tubes and the weight of the reaction chamber. Since the process requires three silicon wafers and the center wafer defines the tube length, it is limited how much lighter the box can be made. As for the tubes, better control of tube mold through etch is likely to ameliorate this problem, but not solve it entirely. The devices as fabricated are too fragile to use in a portable system.

Finally, in the context of TPV, the potential applications for the micro-generator are limited, due to the relatively low efficiency of TPV systems and the resulting waste heat. There is, however, some promise, due to the structural simplicity compared to other generator technologies.

7.3 Recommendations for future work

The first recommended steps to pursue this technology involve catalyst loading, fluidic seals and burst pressure testing. Successful catalyst loading is essential to making the device capable of combustion. Two strategies should be pursued: (1) loading catalyst without silanizing the flow channel surfaces and (2) experimenting with different silanizing agents for different contact angles. Unfortunately the loading cannot be

observed in real time because of the geometry of the device, so it has to be cut open and then inspected.

Obtaining a good hermetic seal between the device, the packaging chip and the aluminum fixture can be done by trying different approaches to cleaning the device bonding surfaces before applying the packaging chips. This is tricky and must be done very carefully to avoid breaking the device. Different epoxies should also be tried if the problem turns out to be with the mounting to the aluminum bars. Once a good seal has been achieved, the device can easily be burst pressure tested, something that is important to assess whether an improvement has been achieved over SμRE I.

With the catalyst and sealing problems solved, the reactor can then be combustion tested, which would allow going to higher temperatures and evaluating the high temperature stability and performance of the device. Photocells can then be applied to both sides of the reactor for power generation.

Beyond this, vacuum packaging is an important step that has already been worked on [4]. The device must ultimately be operated in a vacuum environment to perform at high efficiencies. Integrating photocells with this packaged will be a challenge. It is hoped that this work will be pursued further in some shape of form, as it carries potential for TPV and also other high temperature applications.

Appendix A

SμRE III fabrication process flow

A.1 Process flow

Starting materials: 3 DSP wafers (2 capping wafers of thickness 650 μm and one center wafer of thickness 650-800 μm)

#	Step	Machine	Comments	Lab
A			**ALL 3 WAFERS**	
1	RCA	rca-ICL		ICL
2	Thermal oxide	5C-ThickOx	0.5 μm	ICL
B			**CENTER WAFER**	
1	HMDS	HMDS-TRL	Program 5	TRL
2	Coat	coater	OCG-825, both sides	TRL
3	Photo ALIGN	EV1	Front side, global alignment marks, 2 sec	TRL
4	Photo TUBES	EV1	Front side, 2 sec	TRL
5	Photo TUBES-BACK	EV1	Back side, 2 sec	TRL
6	BOE	acid-hood2	Etch oxide	TRL

#	Step	Machine	Comments	Lab
7	Piranha	acid-hood2	Strip photoresist	TRL
8	HMDS	HMDS-TRL	Program 3	TRL
9	Coat	coater	AZ9260, front side, double layer	TRL
10	Photo TUBES	EV1	Front side, 5x15 sec	TRL
11	DRIE	sts2	Front side, etch until 100 μm left	TRL
12	Mount	coater	Mount with backside down to silicon wafer with thin resist	TRL
13	DRIE	sts2	Etch through into mounting wafer	TRL
14	Dismount		Soak over night in acetone	TRL
15	Piranha	acid-hood2	Strip photoresist	TRL
C			**CAPPING WAFER # 1**	
1	HMDS	HMDS-TRL	Program 5	TRL
2	Coat	coater	OCG-825, both sides	TRL
3	Photo ALIGN	EV1	Inside, global alignment marks, 2 sec	TRL
4	Photo OXHALO	EV1	Inside, 2 sec	TRL
5	Photo CAP1OUT	EV1	Outside, 2 sec	TRL
6	BOE	acid-hood2	Etch oxide	TRL
7	DRIE	sts2	Inside, etch 5 μm to avoid halo bonding	TRL
8	Piranha	acid-hood2	Strip photoresist	TRL
9	Ash	asher-TRL	Oxygen plasma ash to remove passivation residue	TRL
10	HMDS	HMDS-TRL	Program 3	TRL
11	Coat	coater	AZ9260, both sides	TRL
12	Photo CAP1IN	EV1	Inside, 3x15 sec	TRL
13	Photo CAP1THRU	EV1	Outside, 3x15 sec	TRL
14	BOE	acid-hood2	Etch oxide	TRL
15	DRIE	sts2	Inside, etch 400 μm	TRL
16	Mount	coater	Target mount with inside down to fused silica wafer with thick resist	TRL
17	DRIE	sts2	Outside, etch through (appr. 250 μm)	TRL
18	Dismount		Soak over night in acetone	TRL
19	Piranha	acid-hood2	Strip photoresist	TRL

#	Step	Machine	Comments	Lab
D			**CAPPING WAFER # 2**	
1	HMDS	HMDS-TRL	Program 5	TRL
2	Coat	coater	OCG-825, both sides	TRL
3	Photo ALIGN	EV1	Inside, global alignment marks, 2 sec	TRL
4	Photo OXHALO	EV1	Inside, 2 sec	TRL
5	Photo CAP2OUT	EV1	Outside, 2 sec	TRL
6	BOE	acid-hood2	Etch oxide	TRL
7	DRIE	sts2	Inside, etch 5 μm to avoid halo bonding	TRL
8	Piranha	acid-hood2	Strip photoresist	TRL
9	Ash	asher-TRL	Oxygen plasma ash to remove passivation residue	TRL
10	HMDS	HMDS-TRL	Program 3	TRL
11	Coat	coater	AZ9260, inside	TRL
12	Photo CAP2IN	EV1	Inside, 3x15 sec	TRL
13	Protect	coater	Protect outside from BOE with thin resist	TRL
14	BOE	acid-hood2	Etch oxide	TRL
15	DRIE	sts2	Inside, etch 400 μm	TRL
16	Piranha	acid-hood2	Strip photoresist	TRL
E			**ALL 3 WAFERS ***	
1	Ash	asher-TRL	Oxygen plasma ash to remove passivation and other organic residue	TRL
2	Piranha	acid-hood2	Organic clean	TRL
3	HF	acid-hood2	*CENTER WAFER ONLY*, remove oxide, 49%, 15 min	TRL
4	RCA	rca-TRL	Without HF dip	TRL
5	Align/Bond	EV620	CAP2 inside against CENTER, silicon direct	TRL
6	Align	EV620	CAP1 inside against other side of CENTER, fusion	TRL
7	Bond	EV501	Pump vacuum to 1 mTorr before pulling out flags, press overnight	TRL
8	Anneal	B3-DryOx	1000°C, 1 hour, N_2	TRL

#	Step	Machine	Comments	Lab
F			**3-WAFER BONDED STACK**	
1	Nitride	VTR	Low stress silicon nitride, 4 μm	ICL
2	HMDS	HMDS-TRL	Program 5	TRL
3	Coat	coater	AZ5214, front side	TRL
4	Photo METAL	EV1	Front side, 1.5 sec + 60 sec flood	TRL
5	Platinum	eBeamAu	15 nm Ta + 200 nm Pt	TRL
6	Lift-off		Overnight in acetone	TRL
7	Ash	asher-TRL	Oxygen plasma ash to remove organic residue	TRL
8	Tape resist		Apply MX5030 on both sides	TRL
9	Photo CAP1OUT-INV	EV1	Back side, 12 sec	TRL
10	Photo CAP2OUT-INV	EV1	Front side, 12 sec	TRL
11	Develop	photowet-r	AZ917:DI water 1:1, 25-30 sec	TRL
12	DRIE	sts1	Front side, etch 4 μm of nitride, then through (appr. 250 μm) silicon	TRL
13	Mount		Mount to silicon wafer and cover fluidic ports with Capton® tape	TRL
14	DRIE	sts1	Back side side, etch 4 μm of nitride, then through (appr. 250 μm) silicon	TRL
15	Acetone		Remove MX5030	TRL
16	Ash	asher-TRL	Oxygen plasma ash to remove organic residue	TRL
17	Dice	diesaw	Cut into 44 dies	ICL
G			**INDIVIDUAL DIES**	
1	Release	Chemical hood	12.5% TMAH, 3 hours 25 min	SGL
2	Anneal	Box furnace	800°C in air, 5 minutes	JGL
3	Package	Box furnace	See Section 5.2.1	JGL

A.2 Legend

A.2.1 Laboratories

- MTL: Microsystems Technology Laboratories (at MIT)
- ICL: Integrated Circuits Laboratory (class 10 clean room)
- TRL: Technology Research Laboratory (class 100 clean room)
- SGL: Schmidth Group Laboratory (Professor Martin A. Schmidt)
- JGL: Jensen Group Laboratory (Professor Klavs F. Jensen)

A.2.2 Machines

- rca-ICL: Wet chemical station for RCA
- rca-TRL: Wet chemical station for RCA
- 5C-ThickOx: Horizontal tube furnace for wet silicon dioxide growth
- B3-DryOx: Horizontal tube furnace for wet silicon dioxide growth and annealing
- VTR: Silicon Valley Group (SVG) Vertical Thermal Reactor Series 6000 for LPCVD low stress silicon nitride growth (Dichlorosilane 250 sccm, Ammonia 25 sccm, Pressure 250 mTorr, Temperature 775°C, Stress appr. 125 MPa tensile)
- HMDS-TRL: Yield Engineering Systems YES-3 HMDS deposition oven (Program 3 uses 60 sec of HMDS deposition, Program 5 uses 10 sec)
- coater: Solitec Wafer Processing 5110 photoresist spin coater
- EV1: Electro Visions Group 620 Mask Aligner
- acid-hood2: Wet chemical hood for general purpose acid work
- sts1: Surface Technology Systems (STS) Mesc Multiplex DRIE tool

- sts2: Surface Technology Systems (STS) Mesc Multiplex DRIE tool
- asher-TRL: 1000W barrel oxygen plasma asher
- EV620: Electronic Visions EV620 aligner/bonder
- EV501: Electronic Visions EV501 bonding chamber
- eBeamAu: Temescal VES-2550 electron beam deposition system
- photowet-r: Gold contaminated section of a general purpose developing and solvent hood
- diesaw: DISCO Automatic Dicing Saw (DAD-2H/6T)

A.2.3 Acronyms

- RCA: Industry standard for removing contaminants from wafers. Werner Kern developed the basic procedure in 1965 while working for RCA (Radio Corporation of America); hence the name. Procedure: ammonium hydroxide:hydrogen peroxide:water 1:1:6 followed by an HF:water 1:50 dip followed by hydrochloric acid:hydrogen peroxide:water 7:1:1, both at 80°C
- HMDS: Hexamethyldisilazane (photoresist adhesion promoting agent)
- BOE: Buffered Oxide Etch (7:1 water:hydrofluoric acid)
- Piranha: Concentrated sulfuric acid:hydrogen peroxide (30%) 3:1
- DRIE: Deep Reactive Ion Etching
- HF: Hydrofluoric acid
- DI: De-ionized (water)
- TMAH: Tetramethyl ammonium hydroxide

Appendix B

Photomasks

The photo masks were drawn in AutoCad® LT and transferred to chrome patterned glass plates either using printed transparencies and the EV1 exposure tool, or written directly with a laser mask writer.

The packaging chip masks are shown at the end. They are etched all the way through using DRIE. The electrical contact pad areas are halos that fall out at the end.

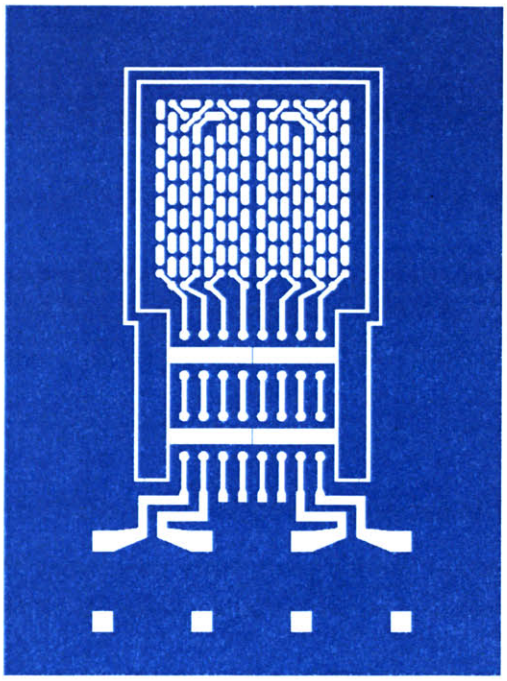

(a) Mask CAP1IN.

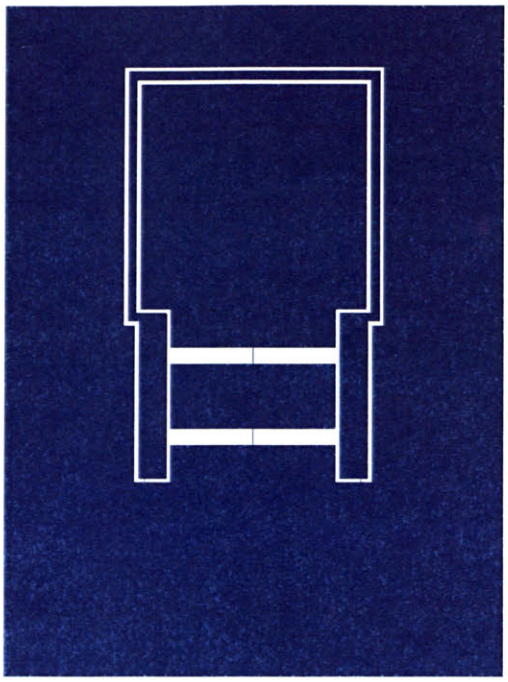

(b) Mask CAP1OUT.

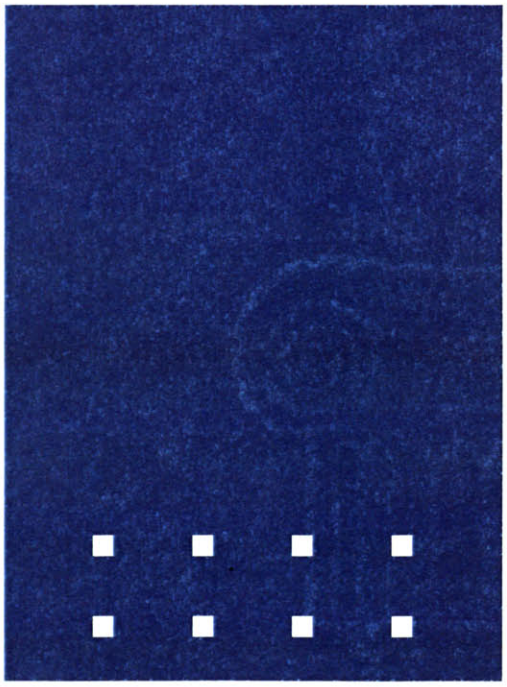

(c) Mask CAP1THRU.

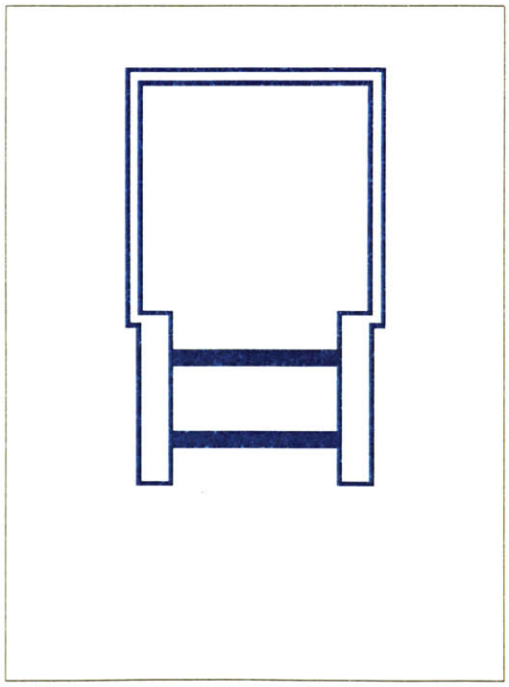

(d) Mask CAP1OUT-INV.

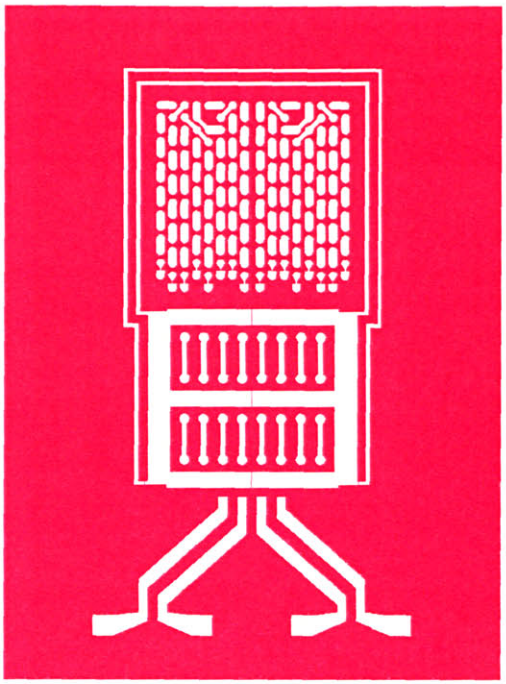

(e) Mask CAP1IN.

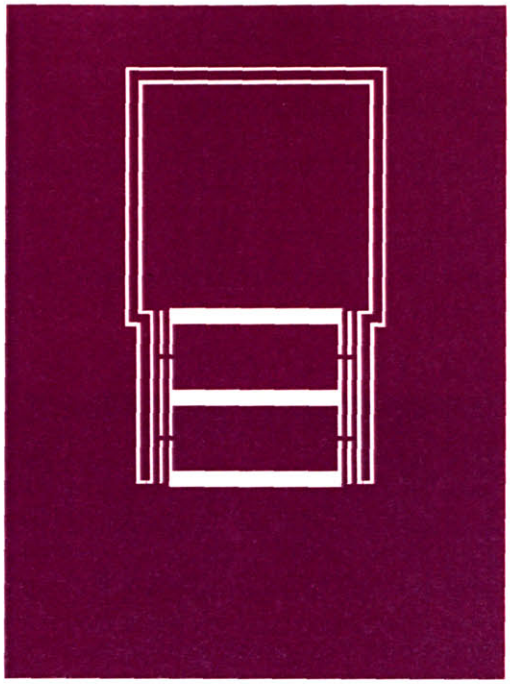

(f) Mask CAP1OUT.

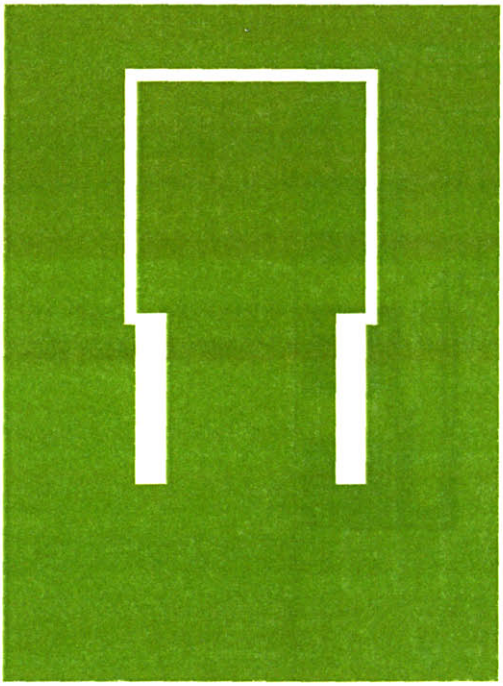

(g) Mask OXHALO.

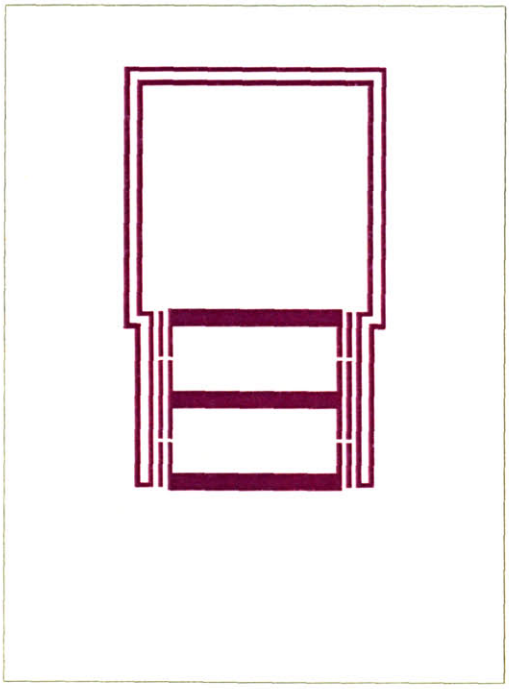

(h) Mask CAP2OUT-INV.

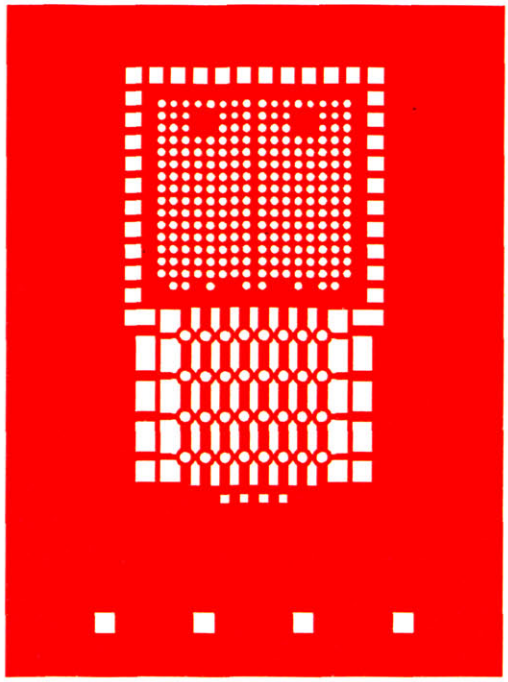

(i) Mask TUBES.

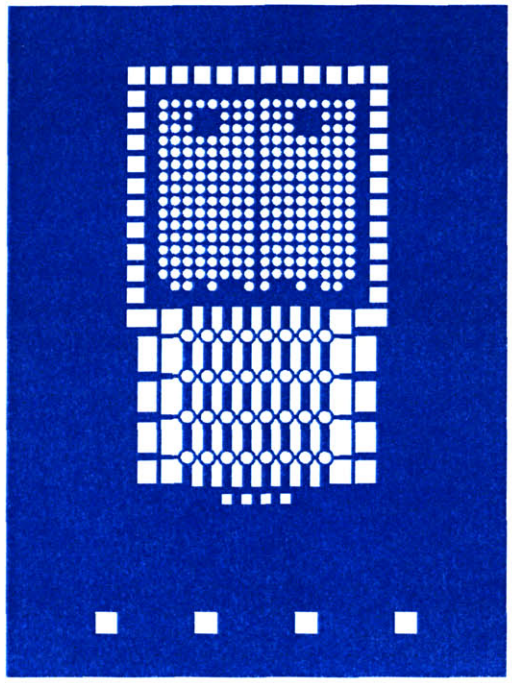

(j) Mask TUBES-BACK.

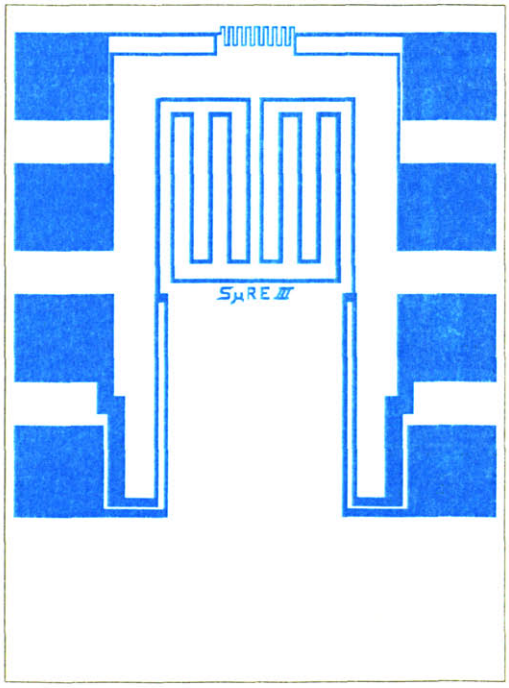

(k) Mask METAL.

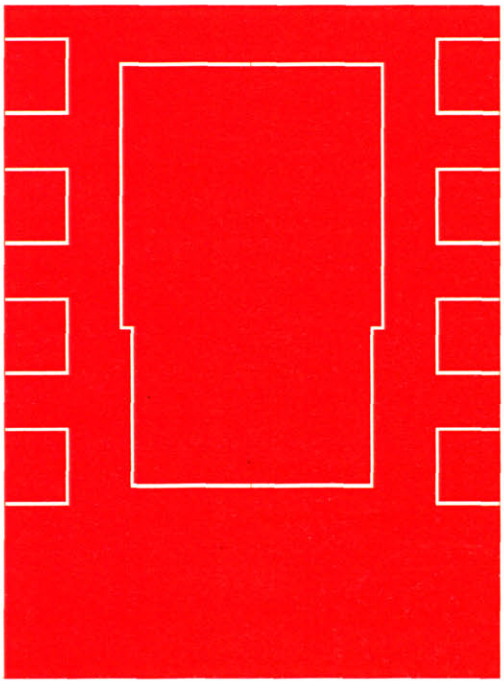

(l) Mask PACKING-FRONT (front side packaging chip).

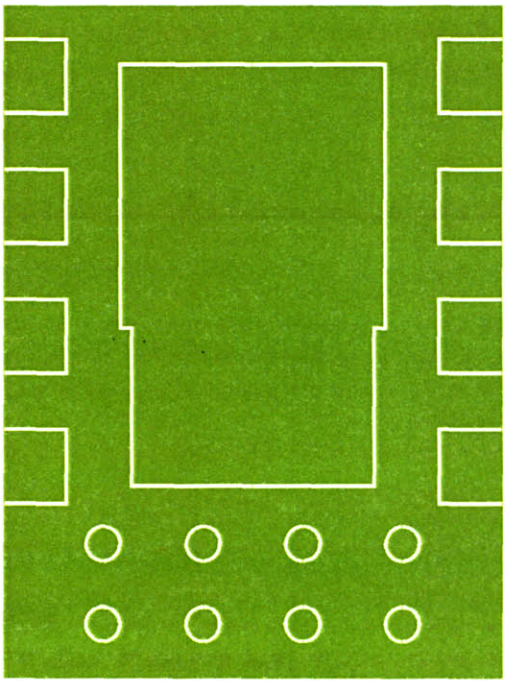

(m) Mask PACKING-BACK (back side packaging chip).

Appendix C

Thermal modeling program code

C.1 therm.m

```
clear all
viewfactors
matrixes

T_h = 700+273.15; %K Reactor temperature
T_c = 25+273.15; %K Ambient temperature

%Heat loss calculations: Power dissipation is positive
%Temperature is given in vector form T = [T_h T_slab3 T_slab2 T_slab1 T_c]
delT = T_h-T_c;
T = [T_h 3*delT/4+T_c 2*delT/4+T_c delT/4+T_c T_c];

Cv=1.6543e6; %J/m^3K heat capacity of silicon
Vs=2.947e-9; %m^3 volume of slab
t=1e-3; %s time of integration
mx=1e-4; %End signal limit

T_C=T-273.15; %Temperatures in Celsius

%Simulation without forced convection:
Ta=T;
```

```
Qa = radiation(Ta,M_r,Av)+Ta*(M_tc+M_nbc);

    while ((abs(Qa(2))>mx)|(abs(Qa(3))>mx)|(abs(Qa(4))>mx));
    Ta = Ta-[0 t*Qa(2:4)/(Cv*Vs) 0];
    Qa = radiation(Ta,M_r,Av)+Ta*(M_tc+M_nbc);
    end

Ta_C=Ta-273.15
Qa
q_cond=Ta*(M_nbc+M_tc)
q_rad=radiation(Ta,M_r,Av)

%Simulation with forced convection:
Tb=T;
Qb = radiation(Tb,M_r,Av)+Tb*(M_tc+M_nbc);
q0 = Qb(1);
Qb = Qb + q0*Tb*M_conv;
q0 = Qb(1);

    while ((abs(Qb(2))>mx)|(abs(Qb(3))>mx)|(abs(Qb(4))>mx));
    Tb = Tb-[0 t*Qb(2:4)/(Cv*Vs) 0];
    Q1 = radiation(Tb,M_r,Av)+Tb*(M_tc+M_nbc);
    Qb = Q1 + q0*Tb*M_conv:
        while abs(Qb(1)-q0)>mx;
        q0 = Qb(1);
        Qb = Q1 + q0*Tb*M_conv;
        end
    end

Tb_C=Tb-273.15
Qb
q_cond=Tb*(M_nbc+M_tc)
q_conv=q0*Tb*M_conv
q_rad=radiation(Tb,M_r,Av)
```

C.2 matrixes.m

```
%General constants and temperatures:
sig = 5.7e-8; %W.m^-2.K^-4
eps_Si = 0.7;
k_SiN = 3.2; %W.m^-1.K^-1
k_Ta = 57; %W.m^-1.K^-1
k_Pt = 72; %W.m^-1.K^-1
t_SiN = 4e-6; %Nitride thickness
t_Ta = 0.01e-6; %Tantalum thickness
t_Pt = 0.4e-6; %Platinum thicnkess

%Tubes:
n_p = 8: %# of tubes in parallel
L_t = 700e-6; %Length of a tube
%l chooses tube length: 1=600um, 2=700um, 3=800um in view factors
l=2;
A_t = 300e-6*pi*t_SiN*n_p; %Total cross sectional area of tube WALLS, all 8 parallel tubes
C_t = n_p*A_t*k_SiN/L_t; %W.K^-1

%Leads on nitride bridges:
kA = k_SiN*120e-6*t_SiN+k_Ta*100e-6*t_Ta+k_Pt*100e-6*t_Pt; %W.m.K^-1
n_nb = 4; %# of nitride bridges in parallel
C_nb1 = n_nb*kA/1065e-6; %Substrate to Slab1
C_nb2 = n_nb*kA/1980e-6; %Slab1 to Slab3
C_nb3 = n_nb*kA/1075e-6; %Slab3 to Reactor

%Areas:
Av=[Areac(l) Aslab Aamb(l)];

%Heat loss calculations: Power dissipation is positive, power addition is negative
```

```
%Tube conduction matrix:
M_tc = C_t*[[ 1 -1  0  0  0];
            [-1  2 -1  0  0];
            [ 0 -1  2 -1  0];
            [ 0  0 -1  2 -1];
            [ 0  0  0 -1  1]];

%Nitride bridge conduction matrix:
M_nbc = [[ C_nb3        -C_nb3 0          0       0];
         [-C_nb3  C_nb3+C_nb2 0       -C_nb2       0];
         [     0          0 0          0       0];
         [     0       -C_nb2 0  C_nb2+C_nb1 -C_nb1];
         [     0          0 0       -C_nb1  C_nb1]];

%Radiation matrix:
VF = [[-Areac(l) fb(l) fc(l) 0        fg(l)]/Areac(l);
      [   fb(l)   -As fa(l) fc(l)    ff(l)]/As;
      [   fc(l) fa(l)   -As fa(l)    fe(l)]/As;
      [       0 fc(l) fa(l)   -As    fd(l)]/As;
      [   fg(l) ff(l) fe(l) fd(l) -Aamb(l)]/Aamb(l)];

M_solve = [eye(5)*(1-eps_Si)/eps_Si eye(5);
                                eye(5)      VF];

M_r = transpose(inv(M_solve));

%Convection matrix:
LHV_C3H8=46350e3;%J/kg
cp_N=1070;%J/kg.K
f_N=16.696;%factor to account for fraction of gas being propane
M_conv = 2*f_N*(cp_N/LHV_C3H8)*[[ 1 -1  0  0  0];
                                [-1  2 -1  0  0];
                                [ 0 -1  2 -1  0];
                                [ 0  0 -1  2 -1];
                                [ 0  0  0 -1  1]];
```

C.3 viewfactors.m

```
%Viewfactors between various elements:
%Slabs 1-3 (S1-3), Reactor (R), Substrate (S), Ambient (A)
%Each factor is given as a vector containing value for tube lengths
  %600, 700 and 800 um.  Format: f=F*A (A is in m^2).

%S1<->S2 and S2<->S3 fa=f1+2*f2
%f1:
Aall=7.8897e-6;
A1=3.3558e-6;
A2=1.1781e-6;
Fall=[0.6657 0.6242 0.5857];
F1=[0.4839 0.4349 0.3926];
F2=[0.2290 0.1958 0.1700];
f1=0.5*(Aall*Fall+A2*F2)-A1*F1;
%f2:
A=3.3558e-6;
F1=[0.2084 0.2280 0.2447];
F2=[0.2958 0.3035 0.3105];
f2=A*(F2-F1);

fa=f1+2*f2;

%S1<->S and S3<->R fb=f2+f3+f4+f5+f6
%f3:
Aall=5.5335e-6;
A1=3.3558e-6;
A2=1.1781e-6;
A3=2.1777e-6;
Fall=[0.6001 0.5543 0.5127];
F1=[0.4839 0.4349 0.3926];
F2=[0.2290 0.1958 0.1700];
F3=[0.3720 0.3262 0.2886];
f3=0.5*(Aall*Fall-A1*F1+A2*F2-A3*F3);
```

```
%f4:
A=2.1777e-6;
F1=[0.2721 0.2913 0.3070];
F2=[0.3504 0.3564 0.3615];
f4=A*(F2-F1);
%f5:
Aall=6.7116e-6;
A1=2.1777e-6;
Fall=[0.1209 0.1355 0.1488];
F1=[0.2721 0.2913 0.3070];
f5=Aall*Fall-A1*F1;
%f6:
Aall=[4.4625 4.8195 5.1765]*1e-6;
A1=[2.142 2.499 2.856]*1e-6;
A2=2.3205e-6;
Fall=[0.5480 0.5655 0.5812];
F1=[0.3628 0.4025 0.4372];
F2=[0.3833 0.3833 0.3833];
f6=0.5*(Aall.*Fall-A1.*F1+A2*F2);

fb=f2+f3+f4+f5+f6;

%S1<->S3 and S2<->S and S2<->R fc=f7
A=2.3205e-6;
F1=[0.3833 0.3833 0.3833];
f7=A*F1;
fc=f7;

%S1<->S/A
As=2*(3570*1270+1270*650+3570*650)*1e-12;
Aslab=As*[1 1 1];
fd=Aslab-fa-fc;

%S2<->S/A
fe=Aslab-2*fa-fc;
```

```
%S3<->S/A
ff=Aslab-fa-2*fc;

%R<->S/A
Areac=[94.6432 96.6312 98.6192]*1e-6;
fg=Areac-fb-fc;

%R to itself approximation
Aamb=2*59475300e-12*ones(1,3)+31160e-6*[1900 2000 2100]*1e-12;
Fh=39052300e-12*ones(1,3)./Aamb;
```

C.4 radiation.m

```
function [q] = radiation(T,M,A)

%Formula for calculating the radiation for a given temperature:

    sig=5.7e-8; %W.m^-2.K^-4
    y = [sig*T.^4 0*ones(1,5)]*M;
    q = y(1:5).*A;
```

Bibliography

[1] Leonel R. Arana. *High-Temperature Microfluidic Systems for Thermally-Efficient Fuel Processing.* PhD dissertation, Massachusetts Institute of Technology, Department of Chemical Engineering, June 2003.

[2] E. J. Brown. The status of thermophotovoltaic energy conversion technology at Lockheed Martin Corp. In *Space Technology and Applications International Forum*, Albuqureque, NM, USA, February 2003.

[3] Ivan Celanovic. *Thermophotovoltaics: Shaping the Flow of Thermal Radiation.* PhD dissertation, Massachusetts Institute of Technology, Department of Chemical Engineering, May 2006.

[4] Kerry Cheung. Die-level glass frit vacuum packaging for a micro-fuel processor system. Master's thesis, Massachusetts Institute of Technology, Department of Electrical Engineering and Computer Science, June 2005.

[5] T. J. Coutts. A review of progress in thermophotovoltaic generation of electricity. *Renewable and Sustainable Energy Reviews*, 3:77–184, 1999.

[6] R. S. DiMatteo. Micron-gap thermophotovoltaics (MTPV). In *Thermophotovoltaic Generation of Electricity, 5th Conference*, number 653 in AIP Conference Proceedings, pages 232–240, Rome, Italy, September 2002.

[7] W. Durisch. Small thermophotovoltaic prototype systems. In *Thermophotovoltaic Generation of Electricity, 5th Conference*, number 653 in AIP Conference Proceedings, pages 71–78, Rome, Italy, September 2002.

[8] A. H. Epstein and S. D. Senturia. Power MEMS and energy conversion. In *Transducers '97*, Chicago, IL, USA, June 1997.

[9] S. L. Firebaugh. Investigation of materials for use in high-temperature, thin-film heaters and temperature sensors. Master's thesis, Massachusetts Institute of Technology, Department of Electrical Engineering and Computer Science, 1997.

[10] L. Fraas. Thermophotovoltaics for combined heat and power using low NOx gas fired radiant tube burners. In *Thermophotovoltaic Generation of Electricity, 5th Conference*, number 653 in AIP Conference Proceedings, pages 61–70, Rome, Italy, September 2002.

[11] L. M. Fraas, J. E. Avery, and H. X. Huang. Thermophotovoltaics: Heat and electric power from low bandgap solar cells around gas fired radiant tube burners. In *29th IEEE PVSC conference*, New Orleans, USA, May 2002.

[12] A. Gombert. An overview of TPV emitter technologies. In *Thermophotovoltaic Generation of Electricity, 5th Conference*, number 653 in AIP Conference Proceedings, pages 123–131, Rome, Italy, September 2002.

[13] S. M. Haile. Fuel cell materials and components. *Acta Materialia*, 51(19):5981-6000, November 2003.

[14] E. E. Horne. 500 watt diesel fueled TPV portable power supply. In *Thermophotovoltaic Generation of Electricity, 5th Conference*, number 653 in AIP Conference Proceedings, pages 91–100, Rome, Italy, September 2002.

[15] H. H. Kolm. Quarterly progress report, solid state research, group 35. Technical report, MIT Lincoln Laboratory, Lexington, MA, May 1956.

[16] S. Y. Lin. A three-dimensional photonic crystal operating at infrared wavelengths. *Nature*, 394:251–253, 1998.

[17] Alexander Mitsos. *Man-Portable Power Generation Devices: Product Design and Supporting Algorithms.* PhD dissertation, Massachusetts Institute of Technology, Department of Chemical Engineering, June 2006.

[18] J. D. Morse. Novel proton exchange membrane thin-film fuel cell for microscale energy conversion. *Journal of Vacuum Science and Technology*, 18:2003–2005, 2000.

[19] R. E. Nelson. TPV and state-of-art development. In *Thermophotovoltaic Generation of Electricity, 5th Conference*, number 653 in AIP Conf. Proc., pages 3–17, Rome, Italy, September 2002.

[20] Ole M. Nielsen, Leonel R. Arana, Chelsey D. Baertsch, Klavs F. Jensen, and Martin A. Schmidt. A thermophotovoltaic micro-generator for portable power applications. In *Transducers '03*, Boston, USA, June 2003.

[21] J. L. Pan, H. K. H. Choy, and C. G. Fonstad. Very large radiative transfer over small distances from a black body for thermophotovoltaic applications. *IEEE Transactions on Electron Devices*, 47(1), January 2000.

[22] F. E. Rasmussen, J. Frech, M. Heschel, and O. Hansen. Fabrication of high aspect ratio through-wafer vias in CMOS wafers for 3-D packaging applications. In *Transducers '03*, Boston, USA, June 2003.

[23] S. B. Schaevitz. A MEMS thermoelectric generator. Master's thesis, Massachusetts Institute of Technology, Department of Electrical Engineering and Computer Science, 2000.

[24] S. B. Schaevitz, A. J. Franz, K. F. Jensen, and M. A. Schmidt. A combustion-based MEMS thermoelectric power generator. In *Transducers '01*, Munich, Germany, June 2001.

[25] L. Schlapbach and A. Zuttel. Hydrogen-storage materials for mobile applications. *Nature*, 414:353–358, 2001.

[26] Robert Siegel and John R. Howell. *Thermal Radiation Heat Transfer*, chapter 7.4. Hemisphere Publishing Corporation, third edition, 10 January 1992.

[27] Peter Vandenabeele and Karen Maex. Influence of temperature and backside roughness on the emissivity of Si wafers during rapid thermal processing. *Journal of Applied Physics*, 72(12), December 1992.

[28] C. A. Wang. Lattice-matched GaInAsSb/AlGaAsSb/GaSb materials for thermophotovoltaic devices. In *Thermophotovoltaic Generation of Electricity, 5th Conference*, number 653 in AIP Conference Proceedings, pages 324–334, Rome, Italy, September 2002.

[29] B. Wernsman. Greater than 20thermophotovoltaic radiator/module system using reflective spectral control. *IEEE Transactions on Electron Devices*, 51(3):512–515, March 2004.

[30] W. Yang. Design, fabrication, and testing of a prototype microthermophotovoltaic system. *Journal of Microelectromechanical Systems*, 13(5), October 2004.

[31] K. Yoshida. High energy density miniature electrical and thermal power source using catalytic combustion of butane. In *17th IEEE International Conference on Micro Electro Mechanical Systems*, Maastricht, The Netherlands, 2004.

[32] C. Zhang. An integrated combustor-thermoelectric micro power generator. In *Transducers '01*, Munich, Germany, 2001.